2014

Low-temperature nuclear magnetic resonance investigation of systems frustrated by competing exchange interactions

Beas Roy
Iowa State University

Low-temperature nuclear magnetic resonance investigation of systems frustrated by competing exchange interactions

by

Beas Roy

A dissertation submitted to the graduate faculty

in partial fulfillment of the requirements for the degree of

DOCTOR OF PHILOSOPHY

Major: Condensed Matter Physics

Program of Study Committee:

Yuji Furukawa, Major Professor

David C. Johnston

Ruslan Prozorov

Soeren Prell

Amy Andreotti

Iowa State University

Ames, Iowa

2014

DEDICATION

I would like to dedicate this work to my parents Mr. Amalendu Sekhar Roy and Mrs. Sutapa Roy, to my dearest little brother Diptanil Roy and to my fiancé Dr. Tanmoy Sarkar.

TABLE OF CONTENTS

LIST OF TABLES

LIST OF FIGURES

ACKNOWLEDGEMENTS

Standing on the verge of completing my doctoral thesis work, I want to express my gratitude to several people who contributed towards this. My thesis would be incomplete without mentioning them.

I would like to start by sincerely thanking my major professor Dr. Yuji Furukawa for his guidance during my research work and during my thesis writing. He has always been patient with me as I have gone through thick and thin both professionally and personally. He has been kind enough to impart his knowlegde in Physics as well as in experiments throughout my research work. He has been an excellent mentor and my work would not have been possible without him.

I would like to extend my sincere gratitude to Dr. David C. Johnston for his constant guidance and kind support both in teaching and in research. He has contributed to my understanding of Physics to a large extent. He has been an excellent guide as my Teaching Advisor during my first year of graduate teaching. I thank him for his valuable advice on my thesis and my published papers.

I thank Dr. Soeren Prell for mentoring me during my first year at Iowa State University as a Graduate Teaching Advisor.

I thank Dr. Ruslan Prozorov for his help and guidance during my first year of Graduate Research work at Iowa State University.

I thank my committee members Dr. Yuji Furukawa, Dr. David C. Johnston, Dr. Ruslan Prozorov, Dr. Soeren Prell and Dr. Amy Andreotti for being supportive of my research work and guiding in my thesis writing. I also thank them for their kind cooperation in fixing the date of final defense so that my parents could attend the convocation ceremony.

I would like to express my gratitude to Dr. Paul C. Canfield and Dr. Sergey Bud'ko for their kind help in high pressure mearuements and valuable discussions which helped me refine

my skills as a researcher. I thank Dr. Paul C. Canfield for his continuous guidance.

I would like to extend my gratitude to Dr. Yoh Kohori and Dr. Hideto Fukazawa firstly for their kind and warm welcome in Chiba University, Japan and secondly for introducing me to the technique of very high pressure measurements in their laboratory which greatly inspired me to do NMR under high pressure. I thank them for their valuable discussions regarding improvising our high pressure measurement techniques.

I would like to thank my group members Dr. Steven L. Yeninas, Dr. Panchanan Khuntia, Paul Wiecki, Jinfang Cui for their kind support and help in laboratory measurments and in discussions regarding my research work. I would also like to thank Dr. Abhishek Pandey for his guidance and important discussions during paper writing. I thank Yasuhiro Komaki for guiding me through my learning of high measurement techniques.

I thank Dr. David C. Johnston, Dr. Paul C. Canfield, Dr. Sergey Bud'ko, Dr. Ramesh Nath, Dr. Abhishek Pandey and Dr. Sheng Ran for preparing the high quality samples on which we had done the NMR measurements.

I also want to thank my school, undergraduate and graduate teachers, instructors and professors without whom my knowledge would be insufficient to successfully conduct research.

I thank my graduate mentor, during my Master's thesis work Dr. Avinash Mahajan, for his guidance and advice and also for encouraging me to do doctoral study in Condensed Matter Physics.

I also want to thank Dr. Indrani Bose for her kind guidance during one of my short research project during my Master's thesis work.

I thank my parents Mr. Amalendu Sekhar Roy and Mrs. Sutapa Roy for their patience, for their undying faith in me, for their encouragement even when they were 7966 miles away from me. I thank my father who has been a friend, a philosopher and a guide in my life and who has always inculcated in me the *Never-say-die* spirit which helped me believe in myself even in the darkest of times. I am grateful to my mother for teaching me to be humble and patient especially in the times when the odds are not in my favor, and not to mention for her extraordinary culinary skills which contributed appreciably towards my work. I thank my brother Diptanil Roy for supporting and encouraging me and my work through his little

naughty and cool ways. Thanks to my family for being my pillar of support.

When I was away from my family the one person who stood by me was my fiancé Dr. Tanmoy Sarkar. I would like to thank him for his unconditional love and support during my research work and during all the days I needed a friend. He has always believed in me and made me believe in myself. I thank him for being a very essential spoke of the wheel of my life.

I thank my friends Sarmistha Banerjee, Dr. Arya Dhar and Dr. Amit Kumar Pal for always being there for me and supporting me with all heart.

Last but not the least, I thank the Almighty for everything.

ABSTRACT

This doctoral thesis emphasizes on the study of frustrated systems which form a very interesting class of compounds in physics. The technique used for the investigation of the magnetic properties of the frustrated materials is Nuclear Magnetic Resonance (NMR). NMR is a very novel tool for the microscopic study of the spin systems. NMR enables us to investigate the local magnetic properties of any system exclusively. The NMR experiments on the different systems yield us knowledge of the static as well as the dynamic behavior of the electronic spins. Frustrated systems bear great possibilities of revelation of new physics through the new ground states they exhibit.

The vandates AA'$VO(PO_4)_2$ [$AA' \equiv Zn_2$ and BaCd] are great prototypes of the $J_1 - J_2$ model which consists of magnetic ions sitting on the corners of a square lattice. Frustration is caused by the competing nearest-neighbor (NN) and next-nearest neighbor (NNN) exchange interactions. The NMR investigation concludes a columnar antiferromagnetic (AFM) state for both the compounds from the sharp peak of the nuclear spin-lattice relaxation rate ($1/T_1$) and a sudden broadening of the ^{31}P-NMR spectrum. The important conclusion from our study is the establishment of the first $H - P - T$ phase diagram of $BaCdVO(PO_4)_2$. Application of high pressure reduces the saturation field (H_s) in $BaCdVO(PO_4)_2$ and decreases the ratio J_2/J_1, pushing the system more towards a questionable boundary (a disordered ground state) between the columnar AFM and a ferromagnetic ground state. A pressure up to 2.4 GPa will completely suppress H_s.

The Fe ions in the "122" iron-arsenide superconductors also sit on a square lattice thus closely resembling the $J_1 - J_2$ model. The ^{75}As-NMR and Nulcear Quadrupole Resonance (NQR) experiments are conducted in the compound $CaFe_2As_2$ prepared by two different heat treatment methods ("as-grown" and "annealed"). Interestingly the two samples show two different ground states. While the ground state of the "as-grown" sample shows a non-magnetic

collapsed tetragonal phase (with no magnetic fluctuations), the ground state of the "annealed" sample shows a magnetically long-range ordered orthorhombic phase. The temperature dependence of $1/T_1$ and that of Knight shift showed that the electron correlations completely disappear in the nonsuperconducting collapsed tetragonal phase in "as-grown" sample of $CaFe_2As_2$ indicating quenching of Fe moments.

The insulating A-site spinel compound $CoAl_2O_4$ exhibits frustration due to competing NN and NNN exchange interactions. This compound has been studied for a long time yet there has been a contradiction as to what the ground state of this compound is. The origin of this ambiguity was pointed out to be microstructure effects such as site-inversion between Co and Al. Thus depending on the value of degree of site inversion x $[(Co_{1-x}Al_x)[Al_{2-x}Co_x]O_4]$, the ground states differ. A very high quality sample was prepared ($x \approx 0.06$) and ^{27}Al and ^{59}Co NMR were performed to study the ground state of this compound. Together with the results from heat capacity, magnetic measurements and neutron diffraction measurements we conclude that the ground state is collinear AFM. We settled a long debated problem for the ground state of $CoAl_2O_4$.

The compound $BiMn_2PO_6$ is a magnetically frustrated system with three-dimensional magnetic ordering. Frustration in this compound is caused by the comparable values of the exchange interactions along the chain, along the rung and in between the ladders. Thus the magnetic structure of this compound is quite complex with the temperature dependence of magnetic susceptibility exhibiting peak at 30 K, a jump at 43 K and a change of slope at 10 K. ^{31}P-NMR study was done on this system to investigate the nature of transitions (if any) at these temperatures. NMR study suggested a long-range AFM transition at 30 K with a sharp peak in $1/T_1$. No signature of transition at 43 K suggested its origin is extrinsic. Between 10 K and 30 K the NMR spectra proved the existence of a commensurate magnetic order while below 10 K, the shape of the NMR spectrum changes either due to an incommensurate magnetic order or due to spin reorientation.

In summary the work presented in this thesis focusses on the NMR investigation of the magnetic properties of various compounds frustrated by the competing exchange interactions.

References

[1] A. Yogi, N. Ahmad, R. Nath, A. A. Tsirlin, J. Sichelschmidt, **B. Roy** and Y. Furukawa, arXiv:1409.3076 (submitted to Phys. Rev. B).

[2] **Beas Roy**, Yuji Furukawa, Ramesh Nath, David C. Johnston, J. Phys.: Conf. Ser. **320**, 012048 (2011).

[3] **Beas Roy**, Yuji Furukawa, David Johnston, Ramesh Nath, Yasuhiro Komaki, Hideto Fukazawa, and Yoh Kohori, "Magnetic phase diagram of the two-dimensional frustrated square lattice compound $BaCdVO(PO_4)_2$ from high-pressure and low-temperature ^{31}P-NMR study", Paper to be submitted.

[4] S. Ran, S. L. Bud'ko, D. K. Pratt, A. Kreyssig, M. G. Kim, M. J. Kramer, D. H. Ryan, W. N. Rowan-Weetaluktuk, Y. Furukawa, **B. Roy**, A. I. Goldman, and P. C. Canfield, Phys. Rev. B **83**, 144517 (2011).

[5] Y. Furukawa, **B. Roy**, S. Ran, S. L. Bud'ko and P. C. Canfield, Phys. Rev. B **89**, 121109 (R) (2014).

[6] **B. Roy**, Abhishek Pandey, Q. Zhang, T. W. Heitmann, D. Vaknin, D. C. Johnston, and Y. Furukawa, Phys. Rev. B **88**, 174415 (2013).

[7] R. Nath, K. M. Ranjith, **B. Roy**, D. C. Johnston, Y. Furukawa, and A. A. Tsirlin, Phys. Rev. B **90**, 024431 (2014).

CHAPTER 1. NUCLEAR MAGNETIC RESONANCE

Nuclear Magnetic Resonance (NMR) is a powerful microscopic technique frequently used in Physics, Chemistry and Biology for the study of matter. In principle, it is possible to perform NMR on every nucleus with nuclear spin I not eqFfiguual to zero. While in Chemisty, NMR is extensively used in determining the structure of organic compounds, in the field Biology, NMR also serves as a great tool for determination of structure and dynamics of proteins. In the field of Condensed Matter Physics, NMR is used to explore magnetic (electronic) properties of compounds microscopically enabling the description of their low-energy spin dynamics.

1.1 Principle of Nuclear Magnetic Resonance

When an isolated nucleus with angular momentum $\vec{I}$ and magnetic moment $\vec{\mu} = \gamma_{\mathrm{N}}\hbar\vec{I}$ (where γ_{N} is the gyromagnetic ratio) is exposed to a static magnetic field $\vec{H_0}$, the field will induce a torque on the magnetic moment $\vec{\mu}$ of magnitude equal to $\vec{\mu}\times\vec{H_0}$. The equation of motion of such a nuclear moment is given by,

$$\frac{d\vec{I}}{dt} = \vec{\mu} \times \vec{H}_0 \tag{1.1a}$$

$$\frac{d\vec{\mu}}{dt} = \vec{\mu} \times (\gamma\hbar\vec{H}_0) \tag{1.1b}$$

Now we transform the eqn. 1.1b from the laboratory frame to a frame rotating at a constant angular velocity $\vec{\omega} = \omega\hat{z}$. In the rotating frame,

$$\frac{d\hat{x}}{dt} = \vec{\omega} \times \hat{x} \tag{1.2}$$

Let a vector $\vec{G}$ be defined as $\vec{G} = G_{\rm x}\hat{x} + G_{\rm y}\hat{y} + G_{\rm z}\hat{z}$ in the lab frame. Thus in the rotating frame the time derivative of this vector will be:

$$\begin{aligned}\frac{d\vec{G}}{dt} &= \hat{x}\frac{dG_{\rm x}}{dt} + \hat{y}\frac{dG_{\rm y}}{dt} + \hat{z}\frac{dG_{\rm z}}{dt} + G_{\rm x}\frac{d\hat{x}}{dt} + G_{\rm y}\frac{d\hat{y}}{dt} + G_{\rm z}\frac{d\hat{z}}{dt} \\ &= \hat{x}\frac{dG_{\rm x}}{dt} + \hat{y}\frac{dG_{\rm y}}{dt} + \hat{z}\frac{dG_{\rm z}}{dt} + \vec{\omega} \times (G_{\rm x}\hat{x} + G_{\rm y}\hat{y} + G_{\rm z}\hat{z}) \\ &= \frac{\delta\vec{G}}{\delta t} + \vec{\omega} \times \vec{G}\end{aligned} \tag{1.3}$$

where $\frac{\delta}{\delta t}$ is the derivative in the lab frame. Putting that in eqn. 1.1b we have:

$$\frac{\delta\vec{\mu}}{\delta t} = \vec{\mu} \times (\gamma_{\rm N}\vec{H}_0 + \vec{\omega}) \tag{1.4}$$

The equations 1.1b and 1.4 are practically same if we replace magnetic field $\vec{H}_0$ by an effective field $\vec{H}_{\rm eff} = \vec{H}_0 + \frac{\vec{\omega}}{\gamma}$ [1].

Now let us take a look at the effect of an oscillating magnetic field on the motion of the magnetic moment in presence of a static magnetic field $\vec{H}_0 = H_0\hat{z}$. We can conceive of an alternating field to consist of two oppositely rotating fields, $\vec{H}_{\pm}(t) = H_1'(\hat{x}\cos\omega t \pm \hat{y}\sin\omega t)$. The two components add to give us $\vec{H}_1(t) = 2H_1'\cos\omega t\ \hat{x} = H_1\cos\omega t\ \hat{x}$ [1][2]. The total magnetic field is: $\vec{H}(t) = \vec{H}_0 + \vec{H}_1(t)$, where typically $|\vec{H}_1| << |\vec{H}_0|$. In a reference frame rotating at an angular velocity of $\omega\hat{z}$, H_1 is static. Also, since the axis of rotation is the same as the direction of the static magnetic field, H_0 will also be static. Thus, in the presence of a static and rotating magnetic field, the equation of motion of the nuclear spin is thus given in the laboratory frame and in the rotating frame by eqn. 1.5 and eqn. 1.6. respectively,

$$\frac{d\vec{\mu}}{dt} = \vec{\mu} \times \gamma[\vec{H}_0 + \vec{H}_1(t)] \tag{1.5}$$

$$\frac{\delta\vec{\mu}}{\delta t} = \vec{\mu} \times [(\omega_z + \gamma H_0)\hat{z} + \gamma H_1\hat{x}] \tag{1.6}$$

where the $\hat{x}$-axis in the rotating frame is chosen along the $\vec{H}_1$. By setting $\omega_z = -\omega$, eqn. 1.6 can be rewritten as :

$$\begin{aligned}\frac{\delta\vec{\mu}}{\delta t} &= \vec{\mu} \times \gamma\left[(H_0 - \frac{\omega}{\gamma})\hat{z} + H_1\hat{x}\right] \\ &= \vec{\mu} \times \vec{H}_{\rm eff}\end{aligned} \tag{1.7}$$

where $\vec{H}_{\rm eff} = \left[(H_0 - \frac{\omega}{\gamma})\hat{z} + H_1\hat{x}\right]$ In other words, the nuclear moment precesses about $H_{\rm eff}$

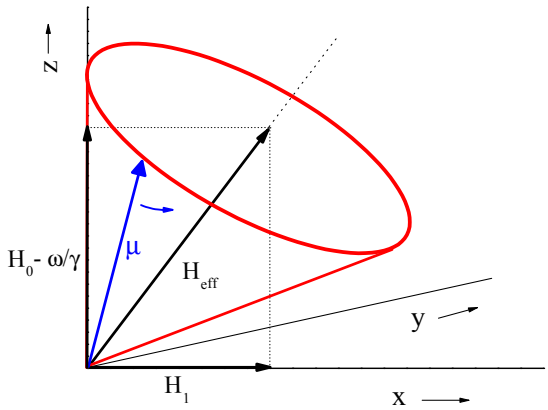

Figure 1.1 (Color online) Effective field H_{eff}. μ, the magnetic moment vector, precesses around H_{eff}.

in the rotating frame Fig. 1.1. For an angular frequency $\omega = \gamma H_0$, we can reduce the effective field to $H_{\text{eff}} = H_1\hat{x}$, if we consider $\hat{x}$-axis to be along the direction of H_1. Thus, the moment now precesses in the $y - z$ plane. If we define θ as the angle which the moment makes with the $\hat{z}$-axis then $\theta = \gamma H_1 t_w$, where t_w is the time for which the alternating field or the radio frequency pulse is switched on. Thus, by controlling t_w and H_1 we can manipulate θ. Thus H_1 and t_w can be chosen such that $\theta = \pi/2$ (90°-pulse) or $\theta = \pi$ (180°-pulse). When we apply a 90°-pulse, the nuclear moment is rotated from an initial $\hat{z}$-direction to $\hat{y}$-direction in the rotating frame. The alternating field alternates the direction of the moments between $\hat{y}-$ and $-\hat{y}-$axis thus producing a flux through a coil with its axis along the $\hat{y}-$axis. Now after the rf pulse is switched off, the moment relaxes back to the original $\hat{z}-$direction, yielding the Free Induction Decay (FID). This FID is the observable in the process of NMR. More about FID and Echo will be discussed later.

Quantum mechanically we can explain the same in the following manner. When an isolated nucleus with angular momentum I and magnetic moment, $\vec{\mu} = \gamma\hbar\vec{I}$ is exposed to a static magnetic field $\vec{H}_0$, the interaction (Zeeman interaction) Hamiltonian is given by,

$$\mathcal{H}_{\text{Zeeman}} = -\vec{\mu}\cdot\vec{H}_0 = -\gamma\hbar\vec{I}\cdot\vec{H}_0 \tag{1.8}$$

In the simplest case if we assume that the static field is applied along the $\hat{z}-$direction, i.e., $\vec{H_0} = H_0\hat{z}$, then the interaction Hamiltonian can be written as :

$$\mathcal{H}_{\text{Zeeman}} \left|m\right\rangle = -\gamma\hbar H_0 I_z \left|m\right\rangle = E_{\text{m}} \left|m\right\rangle \tag{1.9}$$

The energy eigenvalues of this Hamiltonian are given by $E_{\text{m}} = \gamma\hbar H_0 m$ with $2I+1$ values of $m = I,\ I-1,\ .\ ,\ -I$. Transitions between these eigenstates ($\left|m\right\rangle$), labeled by the quantum number m, enable us to observe NMR. These transitions can be induced by radio frequency (rf) magnetic field (say H_1) applied perpendicular to the static magnetic field H_0. Thus, in presence of the rf field the total Hamiltonian becomes $\mathcal{H}(t) = \mathcal{H}_{\text{Zeeman}} + \mathcal{H}_1(t)$, where $\mathcal{H}_1(t)\left|m\right\rangle = -\gamma\hbar H_1 \cos\omega t\ I_x \left|m\right\rangle$. Since typical values of $H_1 << H_0$, $\mathcal{H}_1$ can be treated as a perturbation to the unperturbed Hamiltonian $\mathcal{H}_{\text{Zeeman}}$. As the perturbation is periodic in nature, we can exploit the Fermi's golden rule [3][4] to evaluate the probability of transition per unit time or the rate of transitions between eigenstates $\left|m\right\rangle$ and $\left|m'\right\rangle$. In the limit of a time interval $t \to \infty$, the rate of transition is given by :

$$\mathcal{R}_{\text{m}\to\text{m}'} = \frac{\mathcal{P}_{\text{m}\to\text{m}'}}{T} = \frac{2\pi}{\hbar} |\left\langle m \right| \mathcal{H}_1 \left| m' \right\rangle|^2 \delta(\hbar\omega_{m,m'} - \hbar\omega) \tag{1.10}$$

where $\omega_{m,m'} = E_{\text{m}} - E_{\text{m}'}$, $\mathcal{P}_{\text{m}\to\text{m}'} \propto$ to $|\left\langle m \right| \mathcal{H}_1 \left| m' \right\rangle|^2 \propto |\left\langle m \right| \mathcal{I}_x \left| m' \right\rangle|^2$. Thus, the transition can occur only when the transition probability is not zero, i.e., $\left\langle m \right| \mathcal{I}_x \left| m' \right\rangle \neq 0$, which is satisfied only for $m' = m \pm 1$. Thus, if we consider the simplest case of $I = 1/2$ (Fig. 1.2), the two states are $\left|-1/2\right\rangle$ and $\left|1/2\right\rangle$ with quantum numbers $I_z = -1/2$ and $1/2$ respectively. And transitions are possible between these two states $\left|-1/2\right\rangle \leftrightarrow \left|1/2\right\rangle$ with an exchange of energy $\Delta E = E_{-1/2} - E_{1/2}$.

1.2 Electron-Nucleus Interaction

Now let us inspect the influence of the surrounding electrons on the nuclear energy levels. The nucleus has a magnetic dipole moment which interacts with the magnetic field. The nucleus with $I > 1/2$ also possesses a finite electric dipole moment which interacts with any electric field created by the electronic charges.

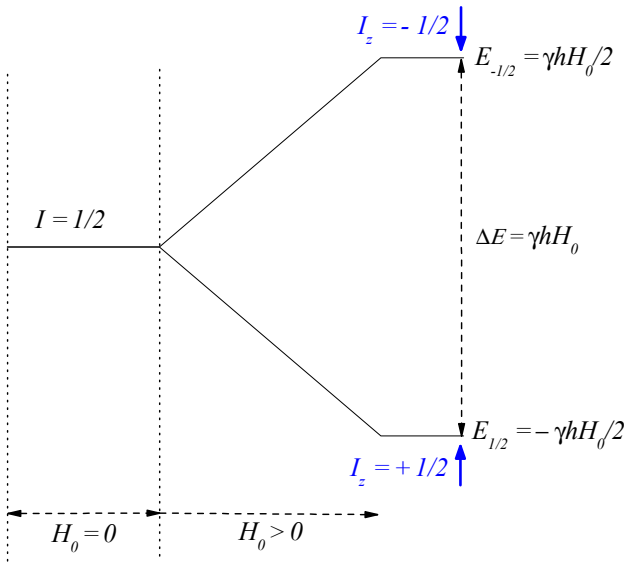

Figure 1.2 (Color online) Zeeman splitting of nuclear energy levels for nuclear spin $I = 1/2$

1.2.1 Electric Interaction

Let us define a nuclear electric multipole operator $\mathcal{A}_l^m$ which would simply be the tensor operator of integer order l [5]. Under the assumption, that the stationary nuclear states have definite parities, electric multipole moments with odd l (order of moment) values are forbidden. Thus the electric dipole moment ($l = 1$) is absent. From the Clebsch-Gordon coefficients, the expectation value of the nuclear multipole operator is non-zero only if $l \leq 2I$. So, for $I = 1/2$, we do not have any electric multipole moment. For nucleus with $I > 1/2$, electric quadrupole moment Q plays an important role in the electron-nucleus coupling. An asymmetry in the distribution of the charges around the nucleus gives rise to an Electric Field Gradient (EFG) which is responsible for a finite Q. Let us mathematically look at the significance of the electric quadrupole moment. A charge distribution with charge density ρ and a potential V due to external sources has an electrostatic energy of :

$$E_{\mathrm{Q}} = \int \rho(\vec{r}) V(\vec{r}) d(\vec{r}) \tag{1.11}$$

If we define a quantity $Q_{\mathrm{a,b}}$, such that,

$$Q_{\mathrm{a,b}} = \int (3x_a x_b - \delta_{\mathrm{ab}} r^2)\rho d\tau \tag{1.12}$$

where $Q_{\mathrm{a,b}} = \delta^2 Q/\delta x_a \delta x_b$ and a and $b \equiv x$, y and z, and with the condition that V satisfies the Laplaces equation ($\nabla^2 V = 0$) it can be shown that the quadrupole energy is given by:

$$E_{\mathrm{Q}}^{(2)} = \frac{1}{6}\sum_{a,b} V_{\mathrm{a,b}} Q_{\mathrm{a,b}} \tag{1.13}$$

where $V_{\mathrm{a,b}} = \delta^2 V/\delta x_a \delta x_b$. Thus, in the case of the nucleus in a cubic environment $V_{\mathrm{xx}} = V_{\mathrm{yy}} = V_{\mathrm{zz}}$ and with $\nabla^2 V = 0$, this would mean the quadrupole interaction vanishes [1].

Quantum mechanically, the quadrupole operator $\hat{Q}_{\mathrm{a,b}}$ for a point charge e, will then be defined as,

$$\begin{aligned}
\hat{Q}_{\mathrm{a,b}} &= \int (3x_{\mathrm{a}}x_{\mathrm{b}} - \delta_{\mathrm{ab}} r^2)\hat{\rho}(\vec{r})d\tau \\
&= e\sum_{\mathrm{k}} \int (3x_{\mathrm{a}}x_{\mathrm{b}} - \delta_{\mathrm{ab}} r^2)\delta(\vec{r} - \vec{r}_k)d\tau \\
&= e\sum_{\mathrm{k}} (3x_{\mathrm{a}}x_{\mathrm{b}} - \delta_{\mathrm{ab}} r^2)
\end{aligned} \tag{1.14}$$

where k is the number of protons since neutrons have 0 charge. Thus, the contribution of the quadrupole interaction in the Hamiltonian is :

$$\mathcal{H}_{\mathrm{Q}} = \frac{1}{6}\sum_{\mathrm{a,b}} V_{\mathrm{a,b}} \hat{Q}_{\mathrm{a,b}} \tag{1.15}$$

Thus, from eqn. 1.14 and 1.15, we have,

$$\mathcal{H}_{\mathrm{Q}} = \frac{eQ}{4I(2I-1)}[V_{zz}(3I_z^2 - I^2) + (V_{xx} - V_{yy})(I_x^2 - I_y^2)] \tag{1.16}$$

With introduction of two quantities η and q [1] such that

$$\text{Field gradient :} \quad eq \equiv V_{zz} \tag{1.17a}$$

$$\text{Assymetry parameter :} \quad \eta \equiv \frac{V_{xx} - V_{yy}}{V_{zz}} \tag{1.17b}$$

eqn. 1.16 becomes :

$$\mathcal{H}_{\mathrm{Q}} = \frac{e^2 qQ}{4I(2I-1)}[3I_z^2 - I^2 + \eta(I_x^2 - I_y^2)] \tag{1.18}$$

A nucleus in its ground state with the positive charge distributed in the shape of a prolate is more likely to be oriented perpendicular to the direction of the external positive charge due to electrostatic force (adapted from [6]) . Thus the interaction of the quadrupole moment and EFG affects the interaction between the magnetic dipole moment and the magnetic field strongly. The quadrupolar interaction causes shift in the otherwise equidistant energy levels. This shift is proportional to the square of the quantum number 'm'. Thus for $I = 3/2$ the energy states with $m = \pm 1/2$ shift identically and those with $m = \pm 3/2$ shift identically (Fig. 1.3).

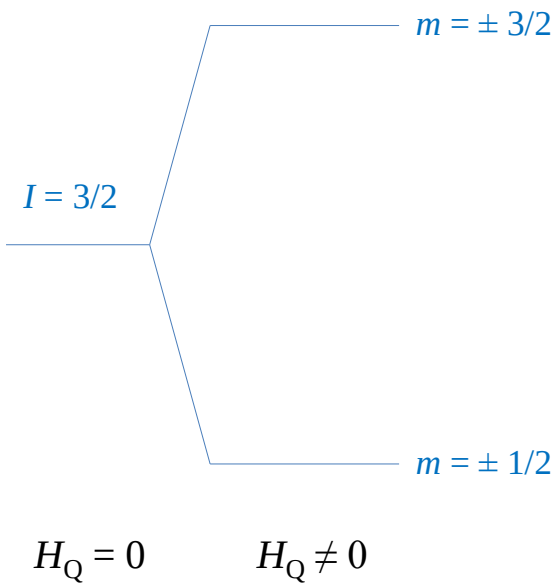

Figure 1.3 (Color online) Quadrupole splitting of energy levels for $I = 3/2$ without any magnetic field. Due to a square dependence of the quadrupolar interaction on the I_z or m, the energy levels are split into 2 levels with $m = \pm 1/2$ and $m = \pm 3/2$.

1.2.2 Magnetic Interaction

To explore the magnetic interaction between the nucleus and electrons, we follow the discussion of the electric interaction in the previous section. Due to opposite parity properties

of electric field (polar vector) and magnetic field (axial vector) even values of l are forbidden, resulting in the magnetic dipole being the first non-vanishing nuclear magnetic multipole.

The magnetic electron-nucleus interaction Hamiltonian is given by[5],

$$\mathcal{H}_M = 2\mu_B \hbar \vec{I} \cdot \left[\frac{\vec{L}}{r^3} + 3\frac{\vec{r}(\vec{S}\cdot\vec{r})}{r^5} - \frac{\vec{S}}{r^3} + \frac{8\pi}{3}\vec{S}\delta(\vec{r}) \right] \tag{1.19}$$

where $\vec{L}$ and $\vec{S}$ are the orbital and the spin angular momentum of the electron respectively. The first term in eqn. 1.19 represents the magnetic interaction between the nuclear spin angular momentum $\vec{I}$ and the electronic orbital angular momentum $\vec{L} = \vec{r} \times \vec{p}$. In some transition metals this term can be important, but in most cases $\vec{L}$ is generally quenched. The second and the third term together represent the dipole-dipole interaction between the nuclear and the electronic spin moments, if they are at a finite distance from each other, typically prevalent in case of p- and d-electrons. This term is responsible for the anisotropic Knight shift $\mathcal{K}_{\text{aniso}}$ (next section) in absence of cubic symmetry and at times even at cubic sites if spin-orbit coupling is present. The third term (Fermi contact interaction term) is used to explain the case of s-electrons which have a finite wavefunction at $r = 0$.

1.3 Knight Shift

The energy difference $\Delta E = h\nu$ between two energy levels $m \leftrightarrow m \pm 1$ is proportional to the applied magnetic field. Depending on the electronic environment, the proportionality factor differs from just simply γ_N. The electron spin moments induce an excess field ($\Delta\vec{H}$) at the nucleus. Thus, the total effective field at the nucleus sums to $\vec{H}_{\text{eff}} = \vec{H}_0 + \Delta\vec{H}$, where $H_0 (= \nu_0/\gamma_N)$ is the standard reference field at the resonating nucleus. Knight shift ($\mathcal{K}$), discovered by Walter Knight [7] for metals, measures this effective field at the nucleus. $\mathcal{K}(\%) \equiv \Delta H/H_{\text{eff}} \times 100 = (H_0 - H_{\text{eff}})/H_{\text{eff}} \times 100$. This implies that $\nu_0 = \gamma_N(1+\mathcal{K})H_{\text{eff}}$. In the frequency-domain the Knight shift is defined by $\mathcal{K}(\%) = (\nu_{\text{res}} - \nu_0)/\nu_0 \times 100$, where ν_{res} corresponds to the peak of the frequency-domain NMR spectrum.

The fourth term of eqn. 1.19 is the Fermi contact interaction between the resonating nucleus and s-electrons. According to the theory first proposed by Townes, Herring and Knight [8][9]

$$\mathcal{K}_{\text{Fermi}} = \frac{8\pi}{3}\chi_p \left\langle \left| \psi_s(0) \right|^2 \right\rangle_{FS} \tag{1.20}$$

where χ_p is the Pauli paramagnetic spin susceptibility per atom and $\langle \mid \psi_s(0) \mid^2 \rangle_{FS}$ is the average over the Fermi surface of the squared magnitude of Bloch wavefunctions evaluated at the site of the nucleus[10]. In addition to this, we have a contribution from the orbital magnetic moment [11] of the conduction electrons :

$$\mathcal{K}_{\rm orb} = 2\chi_{\rm orb} \left\langle \frac{1}{r^3} \right\rangle, \tag{1.21}$$

and also a diamagnetic contribution[12] :

$$\mathcal{K}_{\rm dia} = \frac{8\pi}{3}\chi_{\rm dia} \tag{1.22}$$

where $\chi_{\rm orb}$ and $\chi_{\rm dia}$ are the orbital and the diamagnetic contributions to the magnetic susceptibility. The T dependence of the total Knight shift might change sign depending on the magnitude and sign of the different contributions. The anisotropic component in the Knight shift, which is present in case of nucleus in non-cubic symmetry, does not contribute to the shift of the centroid of the NMR resonance[10].

For a Fermi gas of noninteracting spins,

$$\chi_p = \frac{1}{2}\gamma_{\rm e}^2\hbar^2\rho(E_{\rm F}) = \frac{1}{2}g^2\mu_{\rm B}^2\rho(E_{\rm F}) \tag{1.23}$$

where $g \approx 2.00$ is the spectroscopic splitting factor (g-factor) of the electron spin and $\mu_{\rm B}$ is the Bohr magneton. Also the nuclear spin-lattice relaxation rate $1/T_1$ (to be discussed in the next section) for metals with substantial s-character in the wavefunction at the Fermi surface, is given by[1]:

$$\frac{1}{T_1} = \frac{64}{9}\pi^3\hbar^3\gamma_{\rm e}^2\gamma_{\rm N}^2 \langle \mid \psi_s(0) \mid^2 \rangle_{FS}^2 \rho^2(E_{\rm F}) k_{\rm B} T \tag{1.24}$$

where $\rho(E_{\rm F})$ is the density of states at the Fermi energy for one spin direction. Thus, from eqn. 1.20, eqn. 1.23 and eqn. 1.24, we have:

$$\mathcal{K}^2 T_1 T = \frac{\hbar}{4\pi k_{\rm B}} \frac{\gamma_{\rm e}^2}{\gamma_{\rm N}^2} = \mathcal{S} \tag{1.25}$$

This equation is known as the *Korringa relation*[13]. The ratio $\mathcal{S}/(\mathcal{K}^2 T_1 T)$ is known as the *Korringa ratio*. For an uncorrelated electron system (Fermi Liquid), the ratio is one. For antiferromagnetic correlations when $\vec{q} \neq 0$ fluctuations are dominant, this ratio is greater than

1 and for ferromagnetic correlations, the ratio is less than one. Thus, this ratio plays an important role in determining the nature of spin fluctuations in a metallic system.

Conduction electrons cause a change in the effective field as seen by the nucleus through the hyperfine interaction. In the tensor notation[14]:

$$\mathcal{K}_{\alpha\alpha}(\equiv \mathcal{K}_\alpha) = \frac{H_{\mathrm{hf},\alpha\alpha}}{N_\mathrm{A}\mu_\mathrm{B}}\chi_{\alpha\alpha} \tag{1.26}$$

where $H_{\mathrm{hf},\alpha\alpha}$ is the hyperfine field at the nucleus and μ_B is the Bohr magneton. α is assumed to be along one of the principal axes of the hyperfine field tensor. This formula is widely used to estimate the hyperfine field from the $\mathcal{K}-\chi$ plot.

The tensor $\bar{\mathcal{T}}$ describing the electron-nucleus coupling ($H_\mathrm{hf} = \gamma_\mathrm{N}\hbar\vec{I}\cdot\bar{\mathcal{T}}\cdot\vec{S}$) is not a scalar in the case of symmetry of the electronic environment of the nucleus less then cubic, and the Knight shift will depend on the direction of the applied field with respect to crystalline axes [5]. Since $\mathcal{K} = \Delta H/H = H_\mathrm{hf}/H$, the isotropic term in the Hamiltonian due to the hyperfine field is $-\gamma_\mathrm{N}\hbar\mathcal{K}_\mathrm{iso}(\vec{I}\cdot\vec{H_0})$, where H_0 is the applied field. Also as mentioned, in case of symmetry lower than cubic we will also have an anisotropic term, $-\gamma_\mathrm{N}\hbar[\mathcal{K}_x I_x H_x + \mathcal{K}_y I_y H_y + \mathcal{K}_z I_z H_z]$, where $H_x = H_0\,\sin\theta\,\cos\phi$, $H_y = H_0\,\sin\theta\,\sin\phi$ and $H_z = H_0\,\cos\theta$. Here OX, OY and OZ are the principal axes of the tensor $\bar{\mathcal{T}}$ and $\mathcal{K}_z = -(\mathcal{K}_x + \mathcal{K}_y)$ and θ and ϕ [5] specify the direction of the H_0 with respect to the axes $OXYZ$. Thus, the anisotropic $\mathcal{K}$ can be written as,

$$\mathcal{K}_\mathrm{aniso} = \mathcal{K}_x\,\sin^2\theta\,\cos^2\phi + \mathcal{K}_y\,\sin^2\theta\,\sin^2\phi + \mathcal{K}_z\,\cos^2\theta \tag{1.27}$$

In case of axial symmetry, *i.e.* $\mathcal{K}_x = \mathcal{K}_y = \mathcal{K}_\perp = -\frac{1}{2}\mathcal{K}_z = -\frac{1}{2}\mathcal{K}_\parallel$, eqn. 1.27 becomes:

$$\mathcal{K}_\mathrm{ax} = \frac{1}{2}\mathcal{K}_\parallel\,(3\,\cos^2\theta - 1) \tag{1.28}$$

Thus, the term which should be added to the resonance frequency($\nu_0(1+\mathcal{K})$) is given by,

$$\nu = \frac{1}{2}\mathcal{K}_\parallel\,\nu_0\,(3\,\cos^2\theta - 1) \tag{1.29}$$

Due to the random orientation of crystalline axes in powdered samples used for NMR experiments, all the values of θ are equally probable in powdered sample and also the anisotropic shift results in a broadening proportional to the applied field. If $g(\nu)\mathrm{d}\nu$ is the fraction of particles

having a frequency between ν and $\nu + \mathrm{d}\nu$, then the lineshape can be given by [5]:

$$g(\nu) \sim \frac{1}{|\mathrm{d}\nu/\mathrm{d}u|} \tag{1.30}$$

where $u = \cos\theta$. Due to additional broadening effects (*e.g.* dipolar broadening *etc.*), the real curve is given by the convolution of $g(\nu)$ and $f(\nu)$ (is the shape of resonance curve in absence of anisotropic shift) (Fig. 1.4):

$$I(\nu) = g * f = \int_{-\infty}^{\infty} f(\nu')g(\nu - \nu')\mathrm{d}\nu' \tag{1.31}$$

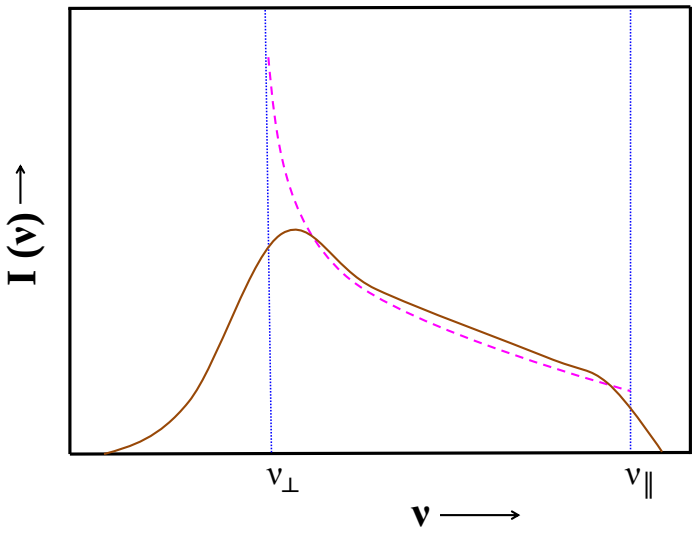

Figure 1.4 (Color online) The solid brown curve is the experimental line shape ($I(\nu)$) for polycrystalline compound including all the sources of broadening. The dashed pink line is the theroetical line shape ($g(\nu)$) in a polycrystalline powder due to anisotropy of Knight shift in presence of axial symmetry.

1.4 Relaxation

1.4.1 Nuclear Spin-Lattice Relaxation (T_1)

As discussed in the previous section, for $I = 1/2$, under a static magnetic field H_0, the two nuclear energy levels with populations $N_\uparrow$ and $N_\downarrow$ are separated by $\Delta E = 2\mu H_0$. At

equilibrium, the nuclei would distribute themselves in the two energy levels such that the ratio of their population will be :

$$\frac{N_{\downarrow}}{N_{\uparrow}} = \exp\left(-\frac{\Delta E}{k_{\mathrm{B}}T}\right) \tag{1.32}$$

Thus, in the state of equilibrium with more number of nuclei in the lower energy level ($N_{\uparrow}$), there exists a net equilibrium nuclear magnetization per mole along the direction of the applied field given by the Curie Law,

$$M_0 = M_{0z} = H_0 \frac{\hbar^2 \gamma_N^2 I(I+1) N_{\mathrm{A}}}{3 k_{\mathrm{B}} T} \tag{1.33}$$

with no transverse component of the magnetization, i.e., $M_{0x} = M_{0y} = 0$[2].

In order to flip a nuclear spin from $\downarrow$ to $\uparrow$, it has to release an energy of $2\mu H_0$ to some reservoir such as the lattice. Thus, the rate at which the magnetization reaches its saturation depends on the properties of the lattice. A spin can flip from a higher to a lower energy state via two kinds of emission: spontaneous or stimulated. The probability of spontaneous emission (A_{21}) is related to the probability of simulated emission (B_{21}) by the relation $A_{21}/B_{21} = 8\pi h\nu^3/c^3$. Since in NMR we deal with radio frequencies, this ratio is very small. Thus to observe NMR signal due to nuclear transitions a stimulated emission, such as a strongly interacting and fluctuating source, is necessary. A time varying rf magnetic field which interacts with nuclear magnetic dipole moment or an EFG which interacts with the nuclear quadrupole moment are two such sources.

For the numerical aspects of nuclear relaxation, let us go through the Bloch Equations. In 1964, F. Bloch proposed a set of phenomenological equations to describe nuclei in the presence of external magnetic field $\vec{H_0} = H_0\hat{z}$. We go through the arguments leading to the establishment of the Bloch equations[5].

1. The equation of motion of the nuclear magnetization for an ensemble of nuclear spins is

$$\frac{\mathrm{d}\vec{M}}{\mathrm{d}t} = \gamma \vec{M} \times \vec{H}_0 \tag{1.34}$$

2. Growth of the longitudinal magnetization (M_z) towards its equilibrium value (M_0) (eqn 1.33) is given by the equation

$$\frac{\mathrm{d}M_z}{\mathrm{d}t} = -\frac{M_z - M_0}{T_1} \tag{1.35}$$

where T_1 is the longitudinal relaxation time. 3. If in addition to the static field, an rf pulse is applied such that there is a finite component of nuclear magnetization at right angles to the static field, then the decay of the transverse component of nuclear magnetization is given by the set of equations :

$$\frac{\mathrm{d}M_x}{\mathrm{d}t} = -\frac{M_x}{T_2} \quad ; \quad \frac{\mathrm{d}M_y}{\mathrm{d}t} = -\frac{M_y}{T_2} \tag{1.36}$$

where T_2 is the transverse relaxation time.

Adding these effects of static field and a small rf field together we have :

$$\frac{\mathrm{d}\vec{M}}{\mathrm{d}t} = \gamma\vec{M} \times \vec{H} - \frac{M_x}{T_2}\hat{x} - \frac{M_y}{T_2}\hat{y} - \frac{M_z - M_0}{T_1}\hat{z} \tag{1.37}$$

where $\vec{H}$ is total field (static and rf field). Eqn. 1.37 is the vector representation of the Bloch equations.

To derive an expression for the nuclear spin-lattice relaxation (T_1) concept of spin temperature T_s is very essential [5][1]. We can describe a system of nuclear spins with a temperature T_s even when it is not in equilibrium with the lattice. The spin temperature in general is defined by,

$$\frac{p_m}{p_{m-1}} = \exp\left(\frac{\gamma\hbar H}{k_\mathrm{B}T_\mathrm{s}}\right) \tag{1.38}$$

where p_m and p_{m-1} are the relative populations for two adjacent energy levels $|m\rangle$ and $|m-1\rangle$. Thus, in case $p_m = p_{m-1}$, T_s is infinite. With this definition of T_s, a statistical description of the system can be made by a density matrix $\rho \propto \exp(-\beta\mathcal{H}_0)$, with $\beta{=}1/k_\mathrm{B}T_\mathrm{s}$. $\mathcal{H}_0$ is the Hamiltonian of the system. The Curie Law $\chi = M/H = C/T$, at a constant field leads to $M \propto 1/T$. Thus, the same time constant T_1 can determine the decay of T_s towards T_L (lattice temperature). Thus, we can write:

$$\frac{\mathrm{d}\beta}{\mathrm{d}t} = -\frac{1}{T_1}(\beta - \beta_0) \tag{1.39}$$

where $\beta_0{=}1/k_\mathrm{B}T_\mathrm{L}$. To determine the expression for T_1 for arbitrary spins, the time derivative $\mathrm{d}\bar{E}/\mathrm{d}t$ of the average energy $\bar{E}$ of the nuclear spin system is calculated in two ways and then equated to each other. With $\bar{E} = \mathrm{tr}\{\rho\mathcal{H}_0\}$,

$$\frac{\mathrm{d}\bar{E}}{\mathrm{d}t} = -\frac{\mathrm{d}\beta}{\mathrm{d}t}\frac{\langle\mathcal{H}_0^2\rangle}{Z} = \frac{1}{Z}(\beta - \beta_0)\frac{\langle\mathcal{H}_0^2\rangle}{T_1} \tag{1.40}$$

where Z ($\sum_m e^{-\beta E_\mathrm{m}}$) is the partition function. The relative population in a state $|m\rangle$ is given by

$$p_\mathrm{m} = \frac{e^{-\beta E_\mathrm{m}}}{Z} \approx \frac{1-\beta E_\mathrm{m}}{Z} \tag{1.41}$$

The approximation is in the limit $k_\mathrm{B}T > \gamma H$ The average energy can then be written as :

$$\bar{E} = \sum_m p_\mathrm{m} E_\mathrm{m} \tag{1.42}$$

The rate of change of population can be written as :

$$\frac{\mathrm{d}p_\mathrm{m}}{\mathrm{d}t} = \sum_n \{W_\mathrm{mn}(p_\mathrm{n} - p^0_\mathrm{n}) - W_\mathrm{nm}(p_\mathrm{m} - p^0_\mathrm{m})\} = \frac{1}{Z}(\beta_0 - \beta)\sum_n W_\mathrm{mn}(E_\mathrm{n} - E_\mathrm{m}) \tag{1.43}$$

where $W_\mathrm{mn} = W_\mathrm{nm}$ is the transition probability from the state $|m\rangle$ to $|n\rangle$ From eqns. 1.41, 1.42 and 1.43,

$$\frac{\mathrm{d}\bar{E}}{\mathrm{d}t} = -\frac{1}{2}\frac{1}{Z}(\beta_0 - \beta)\sum_{\mathrm{m,n}} W_\mathrm{mn}(E_\mathrm{n} - E_\mathrm{m})^2 \tag{1.44}$$

Thus, comparing eqns. 1.40 and 1.44, we can express the nuclear spin-lattice relaxation rate as :

$$\frac{1}{T_1} = \frac{1}{2}\frac{\sum_{\mathrm{m,n}} W_\mathrm{mn}(E_\mathrm{n} - E_\mathrm{m})^2}{\langle \mathcal{H}_0^2 \rangle} = \frac{1}{2}\frac{\sum_{\mathrm{m,n}} W_\mathrm{mn}(E_\mathrm{n} - E_\mathrm{m})^2}{\sum_n E_\mathrm{n}^2} \tag{1.45}$$

which is quite general in application.

Electronic spin fluctuations induce fluctuations in the hyperfine fields at the nuclear site which cause transition in between adjacent nuclear levels. Thus, $1/T_1$ can be expressed as the Fourier transform of this fluctuating hyperfine fields.

$$\frac{1}{T_1} = \frac{\gamma_\mathrm{N}^2}{2}\int_{-\infty}^{\infty} \left\langle \{H^+_\mathrm{hf}(t), H^-_\mathrm{hf}(0)\} \right\rangle \exp(i\omega_0 t) \tag{1.46}$$

where $\omega_0 = \gamma_\mathrm{N} H_0$ is the Larmor nuclear frequency, $\{PQ\} = (PQ + QP)/2$ and $\langle .. \rangle$ is the time average. The bilinear coupling Hamiltonian between the nuclear spin $\vec{I}$ at $\vec{r} = 0$ and the electronic spin $\vec{S}_i$ at the electronic site $\vec{r} = \vec{r}_i$ is given by,

$$\mathcal{H}_\mathrm{hf} = \sum_i \vec{S}_i \cdot \bar{\mathcal{A}} \cdot \vec{I} = \sum_i \sum_{\alpha\alpha'} S_{i,\alpha} \mathcal{A}_{\alpha\alpha'}(\vec{r}_i) I_{\alpha'} \tag{1.47}$$

where $\alpha, \alpha' \equiv x, y, z$, $\bar{\mathcal{A}}$ is the hyperfine coupling tensor and $\sum_i$ runs over all the neighboring electronic spin sites. In terms of the hyperfine field H_hf, the Hamiltonian $\mathcal{H}_\mathrm{hf}$ is :

$$\mathcal{H}_\mathrm{hf} = -\gamma_\mathrm{N}\hbar\vec{H}_\mathrm{hf} \cdot \vec{I} = -\gamma_\mathrm{N}\hbar \sum_{\alpha'} H_{\mathrm{hf},\alpha'} I_{\alpha'} \tag{1.48}$$

Comparing the eqns. 1.46, 1.47 and 1.48, $1/T_1$ can be expressed in terms of the electronic spin-spin correlation function perpendicular to the applied magnetic field,

$$\frac{1}{T_1} = \frac{1}{2\hbar^2} \sum_i \sum_\alpha \sum_{\alpha' \equiv x,y} \mathcal{A}^2_{\alpha\alpha'}(\vec{r}_i) \int_{-\infty}^{\infty} \left\langle S^+_{i,\alpha}(t) S^-_{i,\alpha}(0) \right\rangle \exp(i\omega_0 t) \tag{1.49}$$

Using the fluctuation-dissipation theorem [15], we have,

$$\frac{1}{T_1} = \frac{k_B T}{N\hbar^2 N_A g^2 \mu_B^2} \sum_{\vec{q}} \sum_\alpha \sum_{\alpha' \equiv x,y} |\mathcal{A}_{\alpha\alpha'}(\vec{q})|^2 \frac{\chi''_\alpha(\omega_0, \vec{q})}{\omega_0} \tag{1.50}$$

where N is the number of lattice points in the system, $\sum_{\vec{q}}$ is over all the q values in the first Brillouin zone and χ'' is the imaginary part of the magnetic susceptibility. $\mathcal{A}_{\alpha\alpha'}(\vec{q}) = \sum_i \mathcal{A}_{\alpha\alpha'}(\vec{r_i}) e^{-i\vec{q}\cdot\vec{r_i}}$ is the Fourier transform of $\mathcal{A}_{\alpha\alpha'}(\vec{r_i})$ [2].

1.4.2 Nuclear Spin-Spin Relaxation (T_2)

In the above derivation we have neglected the nuclear spin-spin lattice or the transverse relaxation rate $1/T_2$ which measures how fast the magnetization decays in the XY plane. One way to perceive this is through dipole-dipole interaction between the nuclei. A nucleus starts to experience a local field H_{loc} due to the neighboring nuclei. The z-component of the local field produced at a position $\vec{r}$ by the nuclear dipole $\mu_N = \gamma_N \hbar I$ can be expressed as,

$$H_{\text{loc,z}} \propto \frac{\mu_N}{r^3}\left(3\cos^2\theta - 1\right) \propto \frac{\gamma_N \hbar I}{r^3}\left(3\cos^2\theta - 1\right) \tag{1.51}$$

This field $H_{\text{loc,z}}$ alters the field (H_0) experienced by the nucleus thereby causing it to precess slower or faster than it would otherwise resulting in the dephasing of the nuclei with the T_2 mechanism. If at $t = 0$ the nuclei were all precessing in-phase (coherent) then as a result of this dipole-dipole nuclear interaction they will get out of phase and if in a time which we identifty with T_2 such that $\gamma_N H_{\text{loc}} T_2 \approx 1$, they will be completely phased out and the vector sum of moments ≈ 0, then,

$$\frac{1}{T_2} \approx \gamma_N H_{\text{loc}} \propto \frac{\gamma_N^2 \hbar}{r^3} \tag{1.52}$$

T_2 is also affected by $H_{\text{hf,z}}$, the z-component of the fluctuating field at the nucleus, which increases or decreases the rate of precession[2]. It does not affect the T_1 process (relevant to longitudinal magnetization) but causes decay of transverse magnetization resulting in the T_2

effect. In the limit of the rapid fluctuations ($\omega_0\tau_0 << 1$; ω_0 is the Larmor frequency and τ_0 is the correlation time of the longitudinal fluctuating field) the resonance becomes narrower (*motional narrowing*) due to the first term in the equation 1.53. The spin-lattice relaxation results in the finite lifetime of a spin in an eigenstate ($\Delta E = \hbar\Delta\omega = \frac{\hbar}{T_1}$), thus contributing to the broadening of the resonance. Thus, these two effects must be incorporated in the definition of T_2:

$$\frac{1}{T_2} = \gamma_{\mathrm{N}}^2 \left\langle H_{\mathrm{hf,z}}^2 \right\rangle \tau_0 + \frac{1}{2T_1} \tag{1.53}$$

Apart from the dynamic time-variational fluctuations in the field, there can be static spatial fluctuations in the field having a more macroscopic origin such as inhomogeneity (ΔH) in the applied field. It would contribute a term $\gamma_{\mathrm{N}}\Delta H$ in the expression for T_2. These effects *viz.* inhomogenity of the applied magnetic field, distribution of the static local field at nucleus caused by electrons, nuclear dipole-dipole coupling, T_1 process resulting in a finite lifetime of energy states, and also EFG which lifts the degeneracy of the energy levels, result in the broadening of the absorption line of resonance.

1.5 NMR Detection

We can turn on an rf field H_1 for time t_{w} such that $\gamma H_1 t_{\mathrm{w}} = \pi/2$ in a system of nuclear spins and witness an Free Induction Decay (FID) signal after the switch-off of the rf field (discussed later in this chapter). This FID decays exponentially with a time constant T_2. Due to the inhomogenity in the field there will be a distribution in the precessional frequencies of the nuclei. Thus, even if all the nuclei are coherent in the beginning, they will dephase with respect to each other causing a decay in the resultant signal. To transform the FID signal from the time domain to the frequency domain we use the typical mathematical tool of Fourier transform. Thus, if we consider an FID signal $S(t) = S_0 \exp(-t/T_2)$, then its Fourier transform (FT) will be

$$\begin{aligned} \tilde{S}(\omega) &= \frac{1}{2\pi}\int_{-\infty}^{\infty} \exp(-t/T_2)\, \exp(-i\omega t)\, \mathrm{d}t \\ &= \frac{(1/T_2)}{2\pi[(1/T_2)^2 + \omega^2]} - i\frac{\omega}{2\pi[(1/T_2)^2 + \omega^2]} \end{aligned} \tag{1.54}$$

The FT of the FID signal is a Lorenztian. The real and the imaginary parts correspond to the *absorption mode* and the *dispersion mode* respectively(Fig. 1.5). Generally the dispersion line shape is not chosen to be used. The full width at half its maximum of the absorption lineshape is $(1/\pi T_2)$. But due to the *dead time* (the finite recovery time of the receiver), the initial part of the FID cannot be observed. In the extreme case when T_2 is shorter than the time the receiver (detector) takes for recovery, FID cannot be seen at all. To resolve this constraint concept of *Spin Echo* was introduced in 1950 by Hahn [16]. Carr-Purcell [17] proposed a pulse sequence $\pi/2-\pi$-pulse elaborated in Fig. 1.6 where the refocussing of spins after the π-pulse results in a spin echo. For the measurement of T_1 we used saturation combination $(\pi/2)$ pulse in addition to the $\pi/2-\pi$ pulse sequence. The required pulse sequence is shown in Fig. 1.7.

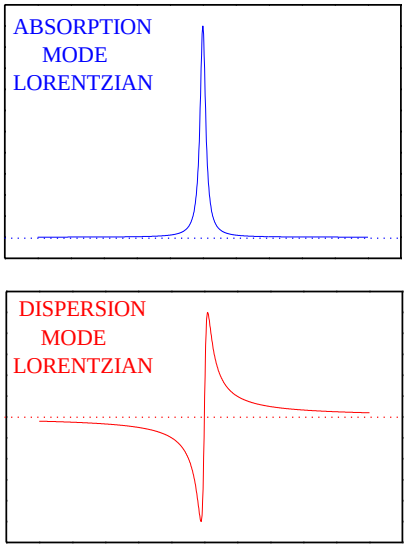

Figure 1.5 (Color online) Fourier transform of Free Induction Decay (FID) Absorptive and Dispersive Lorentzian.

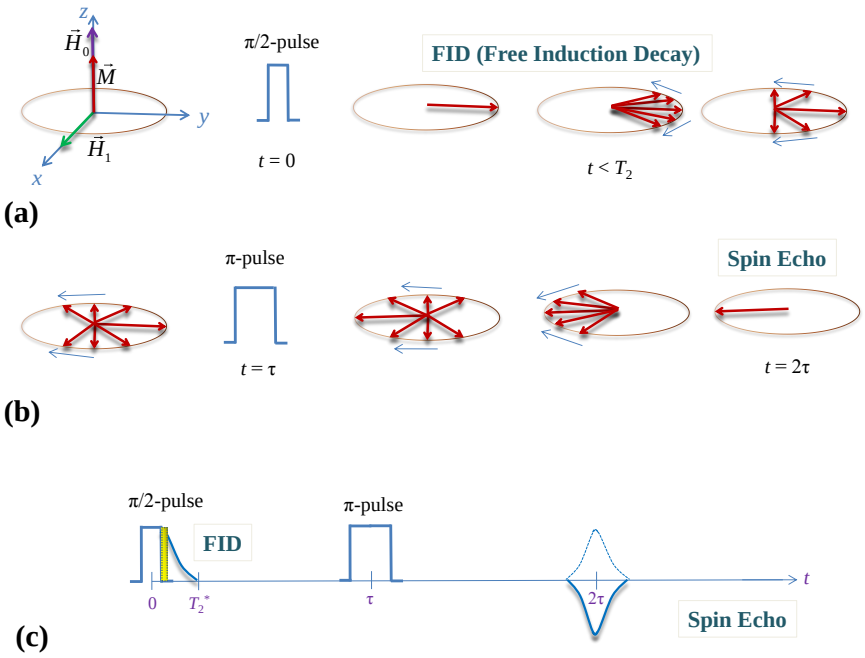

Figure 1.6 (Color online)Formation of a Spin echo by a Carr-Purcell pulse sequence. It is assumed that the thermal equilibrium magnetization ($\vec{M}$) is along the z-axis and we have neglected the T_1 effects for simplicity here. (a) After the initial (t =0) $\pi/2$-pulse, $\vec{M}$ is along the y-axis. Due to the T_2 effect the nuclear spins will precess at different precessional frequencies (FID). (b) At $t = \tau$ a π-pulse is applied and the spins gets refocussed along the -y-axis instead of dephasing out completely thus creating another FID at $t = 2\tau$. (c) The timeline of formation of spin echo. The yellow (gradient) portion just after the first $\pi/2$-pulse is the *dead time* that we had discussed.

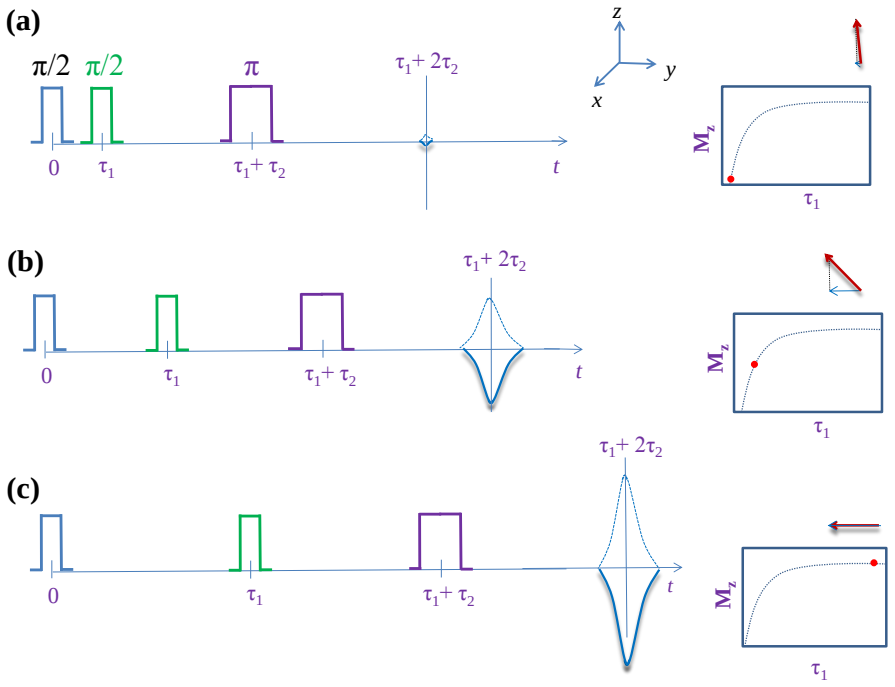

Figure 1.7 (Color online) Measurment of $1/T_1$ by using a single saturation pulse method. (a) shows a very small τ_1 which results in a very small transverse magnetization. As we increase the τ_1 as in (b) and (c), the magnitude of transverse magnetization increases following the formula $M(\tau_1) = M(\infty)(1 - \exp(\tau_1/T_1))$

1.6 NMR Experimental Details

The radio-frequency(rf) power is transmitted from the transmitter section of an NMR spectrometer to an NMR probe containing the sample in a coil (inductor) which is a part of an LC circuit. The power obtained from the coil is transmitted through the same coaxial cable to the pre-amplifier and then to the receiver section of the spectrometer, where the NMR signal is detected. The parameters of the circuit in the probe are very essential in determining the NMR signal obtained. In our experiments we used either copper or silver wires to make coils. To satisfy resonance condition, the resonance frequency ω_0, generated by rf signal generator in the transmitter section, should be equal to $\frac{1}{\sqrt{LC}}$, where L and C are the inductance (coil) and the capacitance of the LC circuit respectively. The capacitance and the inductance of coil determine the resonance frequency of the circuit. The inductance of a coil is generally given by $L \propto \frac{n^2(\pi r^2)}{l}$, where n is the number of turns of the coil, r is the radius of the coil, l is the average length of the coil. Thus, by changing the radius, length and/or number of turns of the coil it is possible to change the frequency of the circuit. The NMR signal intensity depends on the 'filling factor' of the coil, defined as $\frac{\text{Volume of the Sample}}{\text{Volume of the Coil}}$. Thus, closer the size (length and radius) of the coil is to the size of the sample, stronger is the NMR signal. There are two most commonly used configurations of the LC circuit used in NMR experiments shown in Fig. 1.8. The Parallel-Tuned Series-Matched (PTSM) circuit (Fig. 1.8a) and the Series-Tuned Parallel-Matched (STPM) circuit (Fig. 1.8b). The PTSM configuration is generally used for measurements under low frequencies while the STPM configuration is used in the high-frequency measurements. The NMR signal intensity also depends on the Q-factor of the circuit defined as $Q = \frac{\omega_0 L}{R}$, where R is the resistance of the coil. An increase in the Q can have two opposite effects on the NMR signal. On one hand increase of Q can enhance NMR signal but on the other hand it can increase the dead time, the time it takes for the transmission rf energy to dissipate[18] which can make it difficult to see any NMR signal. Thus an optimum value of Q is generally preferred. Q factor can also be defined as $Q = \frac{f_0}{\Delta f}$, where f_0 is the resonant frequency and Δf measures the half-power bandwidth. The network analyzer can be used to measure the Q-factor.

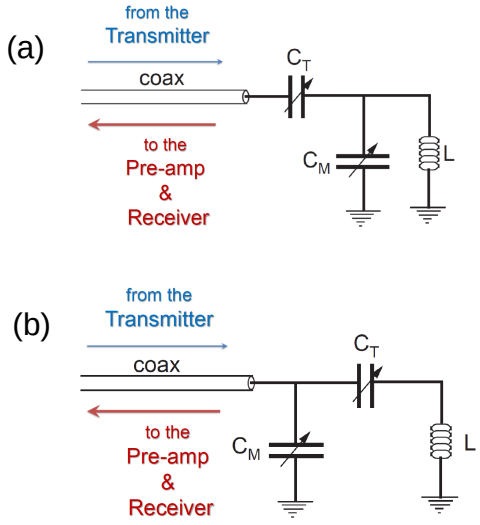

Figure 1.8 (Color online) C_{T} and C_{M} are the tuning and matching capacitances respectively and L is the inductance of the coil. C_{T} is used for tuning the circuit to the desired resonance frequency and C_{M} is used for impedance-matching. The power is transmitted and received back along the same coaxial cable labeled as 'coax' in the figure. The power is transmitted from the transmitter to the probe. The signal obtained from the coil is transmitted back along the 'coax' cable to the pre-amp and then to the receiver. (a) represents the Parallel-Tuned Series-Matched circuit configuration used mainly for low frequencies and (b) represents the Series-Tuned Parallel-Matched circuit configuration used mainly for high frequencies[9].

The NMR measurements were done by using a homemade phase-coherent spin-echo pulse spectrometer. The NMR spectra were measured by doing the Fourier transform of the NMR spin echo signals or by sweeping the magnetic field at a fixed frequency. The NQR spectra was obtained by plotting the spin echo intensity versus frequency where the frequency was changed in regular steps. The nuclear spin-lattice relaxation rate $1/T_1$ was measured using the single-saturation pulse method. In the case of $I = 1/2$ such as ^{31}P and ^{1}H, the nuclear magnetization recovery after a single saturation pulse should follow a single exponential behavior, 1-$M(t)/M(\infty)$ = A e^{-t/T_1} where $M(t)$ is the nuclear magnetization at time t after the saturation pulse. But in case of inhomogeneous distribution of $1/T_1$, we could not fit the data with a single exponential behavior. In that case we used the stretched exponential function 1-$M(t)/M(\infty)$ = A $e^{-(t/T_1)^{\beta}}$.

1.7 NMR Under High Pressure

The ground states of most of the compounds in Condensed Matter Physics is quite sensitive to application of pressure [19]. Thus NMR study under pressure at low temperatures (down to $\sim$ mK using a ^{3}He-^{4}He dilution refrigerator (Kelvinox MX100, Oxford instruments) installed at Ames Laboratory) offers scope for determining evolution of near zero-temperature properties with pressure.

For application of pressure we use a hybrid Cu-Be/NiCrAl clamp-type high-pressure cell (R&D Support Corporation) (Fig. 1.9) which can yield a pressure of up to 2.5 GPa at room temperature, and marks a clear progress from a simple Cu-Be pressure cell which can yield up to only 1.5 GPa[20]. Our hybrid pressure cell consists of non-magnetic WC pistons, a NiCrAl inner cylinder encompassed by Cu-Be outer cylinder. It has a height of 62 mm, an inner and outer diameter of 6 mm and 20 mm respectively. The sample (inside the NMR coil of dimensions length $\sim$ 3 mm and diameter $\sim$ 3 mm) for study, is inserted into the teflon tube which is filled with a liquid pressure-transmitting medium. Liquid pressure media have their own hydrostatic limit, i.e. there is a maximum pressure above which they solidify. Daphne 7373 [21] which can yield a hydrostatic pressure up to 2.5 GPa at room temperature is a better choice than Fluorinert which solidifies at around $\sim$ 0.55 - 0.9 GPa [22]. Although isopentane has a higher limit to the hydrostatic pressure ($\sim$ 3 GPa) [23], it causes serious damage to samples due to a discontinuous pressure drop associated with solidification on cooling[21]. In all our NMR experiments under high pressure we have used Daphne 7373 as the pressure-transmitting medium. Since the ^{63}Cu-NQR frequency, ν_Q varies linearly with pressure [25], we used ^{63}Cu-NQR (nuclear quadrupole resonance) corresponding to the transition in Cu_2O for pressure calibration.The pressure dependence of ν_Q at a given temperature[25] is given by:

$$\nu_Q(P,T) = A + BP + CP^2 \tag{1.55a}$$

$$A(T) = 27.06 - 0.4762\rho(T) \tag{1.55b}$$

$$B(T) = 0.04154 - 0.002682\rho(T) \tag{1.55c}$$

$$C(T) = -2.992 \times 10^{-6}\rho(T) \tag{1.55d}$$

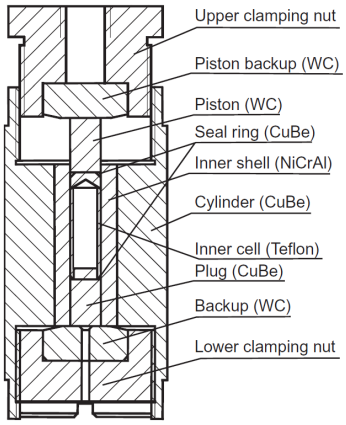

Figure 1.9 (Color online) CuBe/NiCrAl high-pressure cell[24]

So we inserted two coils into the teflon tube, one for the sample we want to investigate and another for the powdered Cu_2O we used to detect the NQR frequency. The two coils were arranged perpendicular to each other so as to avoid interference of signals.

Fig. 1.10 shows how sample pressure changes with temperature for different applied pressures. With decrease in temperature from room temperature to 100 K, the pressure decreases by 0.25 GPa. Below 100 K, the sample pressure is almost constant down to 4.2 K.

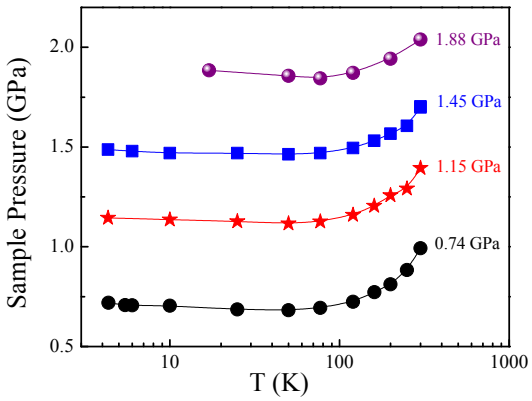

Figure 1.10 (Color online) Sample Pressure vs Temperature in different pressure regimes

CHAPTER 2. FRUSTRATED SYSTEMS

2.1 Quantum Magnetism

Quantum magnetism plays a very dynamic role in the field of Condensed Matter Physics. The interest arises from the novel characteristics derived from its study especially in low-dimensional systems and for low spins where the quantum effects are manifested most prominently. The experimental realizations of low-dimensional systems from linear chains [26], to spin ladders [27] to two-dimensional lattices [28] have gained a lot of interest in the study of many-body systems. Further, the two-dimensional (2D) layers of CuO_2 and FeAs in the high-T_c cuprate and iron-based superconductors respectively enhanced the importance of study of the low-dimensional AFM systems.

The parameter characterizing the quantum magnets is the exchange interaction (between neighboring spins) strength J defined by the exchange integral (eqn. 2.1), obtained from the diagonalization of the Hamiltonian:

$$J_{12} = \pm 2e^2 \int \mathrm{d}\vec{r_1} \int \mathrm{d}\vec{r_2} \, \frac{\phi_a^*(r_1)\phi_b^*(r_2)\phi_a(r_2)\phi_b(r_1)}{|\vec{r_1} - \vec{r_2}|} \tag{2.1}$$

where (1, 2) are electron sites and (a, b) are electronic energy states and from Pauli exclusion principle, the total wavefunction of an electron ($\psi(\vec{r}, \vec{\sigma}) = \phi_{\text{orbital}}(\vec{r})\chi_{\text{spin}}(\vec{\sigma})$) must be anti-symmetric. The exchange interaction (J_{12} or more generally J_{ij}) is typically short-ranged and occurs either between neighboring electrons through Coulomb interaction (*direct exchange*) or between electrons separated by non-magnetic ions in insulators (*superexchange*) or between electrons separated by conduction electrons in metals with f-electrons (*indirect exchange*) or interactions among the conduction electrons (*itinerant exchange*)[29]. With the definition of J_{ij} in eqn. 2.1, the interaction Hamiltonian between two spins $\vec{S_i}$ and $\vec{S_j}$ is respectively given

by,

$$\mathcal{H}_{\text{interaction}} = \sum_{<ij>} J_{ij} \vec{S}_i \cdot \vec{S}_j \tag{2.2}$$

While the lattice dimensionality is summarized in Fig. 2.1, depending on the spin dimensionality(Fig. 2.2) (number of components of the spin vector allowed to contribute in the Hamiltonian) the generalized Hamiltonian are as follows:

$$\mathcal{H}_{\text{Ising}} = \sum_{<ij>} J_{ij} S_i^z S_j^z \qquad \text{Ising Model} \tag{2.3a}$$

$$\mathcal{H}_{\text{XY}} = \sum_{<ij>} (J_{ij}^x S_i^x S_j^x + J_{ij}^y S_i^y S_j^y) \qquad \text{XY Model} \tag{2.3b}$$

$$\mathcal{H}_{\text{Heisenberg}} = \sum_{<ij>} (J_{ij}^x S_i^x S_j^x + J_{ij}^y S_i^y S_j^y + J_{ij}^z S_i^z S_j^z) \qquad \text{Heisenberg Model} \tag{2.3c}$$

For isotropic XY model $J_{ij}^x = J_{ij}^y$ and for isotropic Heisenberg model $J_{ij}^x = J_{ij}^y = J_{ij}^z$.

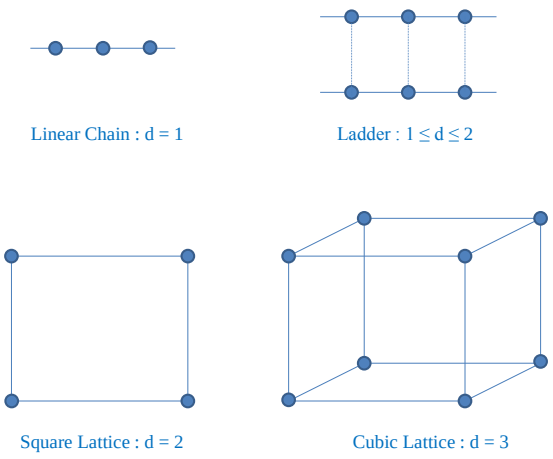

Figure 2.1 (Color online) Lattice with dimensionality "d".

2.2 Frustration

The ground state of a system is typically characterized by the eigenstate with minimum energy. Failure to simultaneously satisy minimization of ground state energy and interaction of

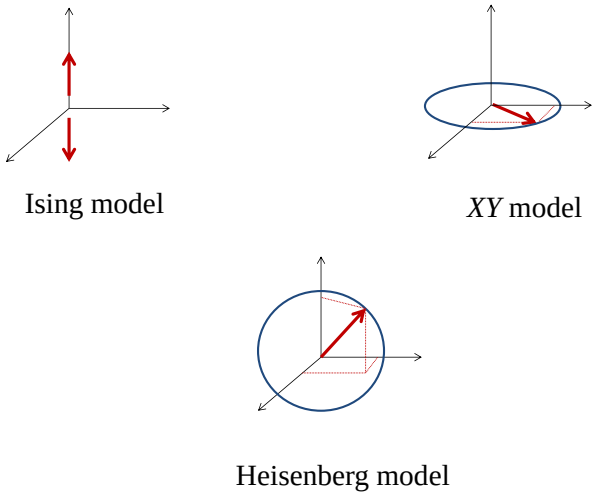

Figure 2.2 (Color online) Spin Dimensionality.

all the spin pairs leads to "Frustration". In the words of R. Moessner [30] frustration starts to emerge whenever "a conflict arises between geometry of the space inhabited by a set of degrees of freedom and the local correlations favored by their interactions". Toulouse [31] defined frustration in the following way (discussed in Ref.[32]): if we consider an elementary cell of the lattice which is a polygon formed by faces known as "plaquettes", then such a plaquette is frustrated if the parameter P defined by,

$$P = \prod_{<i,j>} \text{sign}(J_{ij}) \tag{2.4}$$

is negative, where the product includes all the J_{ij} around the plaquette. According to the definition of the interaction Hamiltonian (eqn. 2.2), a negative J_{ij} favors a parallel (ferromagnetic FM) arrangement of neighboring spins, while a positive J_{ij} favors an antiparallel (antiferromagnetic AFM) arrangement of neighboring spins. Suppose we consider the case of a triangular arrangement of Ising spins (the first frustrated system studied in 1950[33]) with (nearest-neighbor) NN AFM interaction only ($E_{Ising} = J_{ij} S_i^z S_j^z$) , we see that there is no unique way to minimize the interaction energy and minimize all the three interactions simultaneously. There are three degenerate configurations for the ground state where we can arrange the spins

so that two bonds are AFM and one bond is FM (Fig. 2.3). This arrangement of Ising spins on a triangluar lattice is a very common example of geometrically frustrated systems. Other such geometries include the 2D Kagome lattice [34] consisting of vertex-sharing triangles, and also three-dimensional (3D) lattices such as checkerboard or pyrochlore lattice [35] consisting of vertex-sharing tetrahedra. Frustration can also arise due to competing interactions such

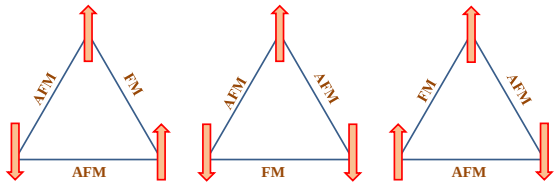

Figure 2.3 (Color online) Configurations of AFM Ising spins in a triangular lattice.

as in Villain model[36], in R_5T_4 (R = rare earth, T = Ge or Si) [37] where the FM intra-layer interaction competes with the AFM inter-layer interaction, in $J_1 - J_2$ square lattice where FM NN (along the side) and AFM next-nearest-neighbor (NNN) interactions are comparable (to be discussed later in this chapter), in double pervoskite ($A_2BB'O_6$, A = Ca, Ba, Sr, B, B' = transition metals) family of compounds[38] where inequivalent NN and NNN exchange interactions compete, in spinels AB_2O_4 where frustration arises since within each sublattice there is AFM coupling (to be discussed later in this chapter), and in spin ladder compounds [39] where frustrated interchain exchange interactions occur both on rungs and diagonals. Since frustration results in multi-degenerate ground states rather than one unique stable one, introduction of very small perturbations or fluctuations in the system cause very novel and exotic phenomena to emerge many of which have not been well explained or understood yet. The frustration effects lead to very emergent phenomena and interesting ground states with no long-range ordering such as spin liquid[26], spin glass[27], spin ice[28], resonating-valence-bond state[40], quantum

spin liquid state[41] and quantum spin glass[42]. The properties of these exotic ground states are tunable externally through chemical substitution, pressure or internally via fluctuations.

Apart from the general interest in frustrated low-dimensional materials, the advent of high-T_c superconductivity in cuprates and pnictides with two-dimensional AFM spins in a square lattice has induced much interest in frustration. The undoped cuprates and pnictides show long-range ordering to Néel state at low temperatures. Doping with holes or electrons destroys the long-range antiferromagnetic order in these compounds and superconductivity emerges. In 1987 Anderson [43] had suggested that the mechanism of superconductivity in high-T_c superconductors can be explained by the existence of a disordered (lacking LRO) phase which he proposed to be a "quantum spin liquid" state, more specifically "resonating-valence-bond" state. This provided a strong impetus in the study of disordered ground states.

One of the ways frustration is manifested in experiments is by the ratio ("frustration ratio") $f = |\theta_{CW}|/T_N$, where θ_{CW} is the Curie-Weiss temperature and T_N is the Néel ordering temperature. According to mean field theory, θ_{CW} $(= S(S+1)\sum_j J_{ij}/3k_B$[44]) gives us an estimation of the exchange energy while T_N $(= 2S(S+1)\sum_j |J_{ij}|/3k_B$[44]) marks the transition to a long-range ordered state. In a non-frustrated system, $T_N \sim |\theta_{CW}|$, while for a frustrated system where the LRO is majorly suppressed, generally $T_N << |\theta_{CW}|$ (Fig 2.4). A system is typically considered to be strongly frustrated when $f > 10$. The f value can be very high in both two-dimensional (>500 [45]) and three-dimensional (>100 [46]) magnetic systems. A list of values of f for different compounds is shown in Fig 2.5

Note that suppression of the T_N does not necessarily mean geometric frustration. Spin dimensionality also affects the LRO. According to Mermin-Wagner theorem [49], "At non-zero temperature, a one- or two-dimensional isotropic spin-S Heisenberg model with finite-range exchange interaction can be neither ferromagnetic nor antiferromagnetic." In other words, there cannot be any FM/AFM LRO at finite temperature in one- or two-dimensional lattice.

The degeneracy in the ground state of a frustrated system can be broken by perturbations such as dipolar interactions and minimal disorder in spin-ice pyrochlores[50], the spin-lattice coupling in spinels [51] and the Dzyaloshinskii-Moriya interactions in Cs_2CuCl_4 [52]. At times thermal fluctuations present in the systems acts as the degeneracy-breaking mechanism and

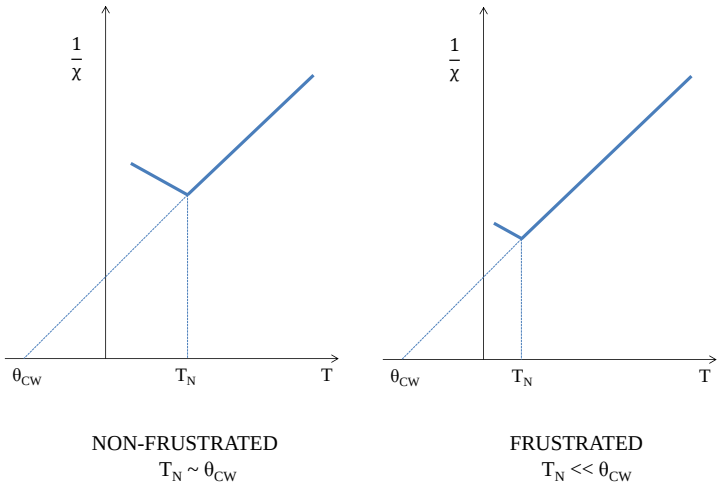

Figure 2.4 (Color online) Signature of frustration in AFM systems[47]. In a non-frustrated AFM ordered system the $T_{\rm N} \sim |\theta_{\rm CW}|$ while in a frustrated system $T_{\rm N} << |\theta_{\rm CW}|$

selects a single or a subset of states which show long-range order (LRO) to some extent, and this is known as "Order by disorder"[53].

2.3 Outline of the Thesis

Study of frustrated systems bears the possibility of revelation of new physics as well as explanation of some puzzling phenomena like unconventional superconductivity. Inspired by the very novel and yet not fully understood effects of frustration, this thesis majorly delves into the study the magnetic properties of the two-and three-dimensional frustrated systems at low temperatures using the technique of nuclear magnetic resonance (NMR). Fig. 2.6 summarizes frustrated systems I have discussed in this thesis. For studying the magnetic properties of the different frustrated materials from a microscopic viewpoint NMR stands out as a very efficient tool. NMR also enables us to explore spin dynamics at very low energy scales ($<$ mK) where the quantum effects are the strongest. While the static (NMR spectrum) results provide us insight of spin orientation, static internal field and dimensionality of the system, the dynamic survey ($1/T_1$,$1/T_2$) helps us observe the nature of spin fluctuations, density of states etc. in the

Material	Lattice	$\|\theta_{cw}\|$	f
κ-(BEDT-TTF)$_2$Cu$_2$(CN)$_3$	≈ triangular	375 K	> 10^3
EtMe$_3$Sb[Pd(dmit)$_2$]$_2$	≈ triangular	350 K	> 10^3
ZnCu$_3$(OH)$_6$Cl$_2$	kagome	240 K	> 10^3
Cu$_3$V$_2$O$_7$(OH)$_2$ · 2H$_2$O	≈ kagome	120 K	≈ 100
BaCu$_3$V$_2$O$_8$(OH)$_2$	≈ kagome	80 K	> 10^2
Cs$_2$CuCl$_4$	quasi one-dimensional	4 K	≈ 10

Figure 2.5 (Color online) List of Frustrated materials with high frustration ratio f [54].

system. The utility of NMR in reflecting the local properties of electrons from a microscopic viewpoint makes it a very sensitive probe for investigation of compounds in Condensed Matter Physics.

2.3.1 $J_1 - J_2$ Model

The $J_1 - J_2$ model consists of the magnetic spins sitting on the square lattice. The nearest-neighbor (NN) exchange coupling (J_1) is between the spins sitting along the sides of the square and next-nearest-neighbor (NNN) exchange coupling (J_2) is between the spins sitting along the diagonal of the square (Fig. 2.7a). The Heisenberg Hamiltonian for such a model is given by,

$$\mathcal{H}_{J_1-J_2} = J_1 \sum_{<ij>} \vec{S_i} \cdot \vec{S_j} + J_2 \sum_{<ik>} \vec{S_i} \cdot \vec{S_k} \tag{2.5}$$

where $< ij >$ are pairs of NN spins and $< ik >$ are pairs of NNN spins. In an ideal 2D $J_1 - J_2$ model there is no interplane exchange coupling ($J_\perp = 0$) between the magnetic planes, so it is strictly a two-dimensional (2D) model. Here it is interesting to pause and look at the theorem proposed by Mermin and Wagner which states that magnetic long-range order (LRO) cannot exist for one- and two-dimensional systems. Thus, the discussion about these 2D models

	***Quasi* -2D**	**3D**
Localized & Frustrated	$Zn_2VO(PO_4)_2$ (Chap 3.1) $BaCdVO(PO_4)_2$ (Chap 3.2)	$CoAl_2O_4$ (Chap 5) $BiMn_2PO_6$ (Chap 6)
Itinerant	$CaFe_2As_2$ (Chap 4)	

Figure 2.6 (Color online) Outline of the thesis

having a LRO is contradictory to the theorem. The answer is simple. The assumption that the magnetic layers in these compounds are decoupled is incorrect. Although very small, there is a finite contribution from $J_\perp$ in the real systems. Thus, these systems may be better termed as $quasi-2D$. Also real systems may not have a perfect square lattice structure i.e. in the case of in-plane anisotropy the exchange couplings along the two sides or along the two diagonals are not same. Chapter 3 and Chapter 4 will be focussing on these *quasi*-2D localized and itinerant materials respectively.

(i) *Localized Frustrated Quasi-2D Systems*

Recently low dimensional magnetic systems have been of great interest due to their unconventional, novel and complex magnetic properties. The relevance of the 2D antiferromagnetic (AFM) systems to the physics of high-T superconductors makes the study of the former more appealing. One of the most striking effects in these systems is the formation of quantum dis-

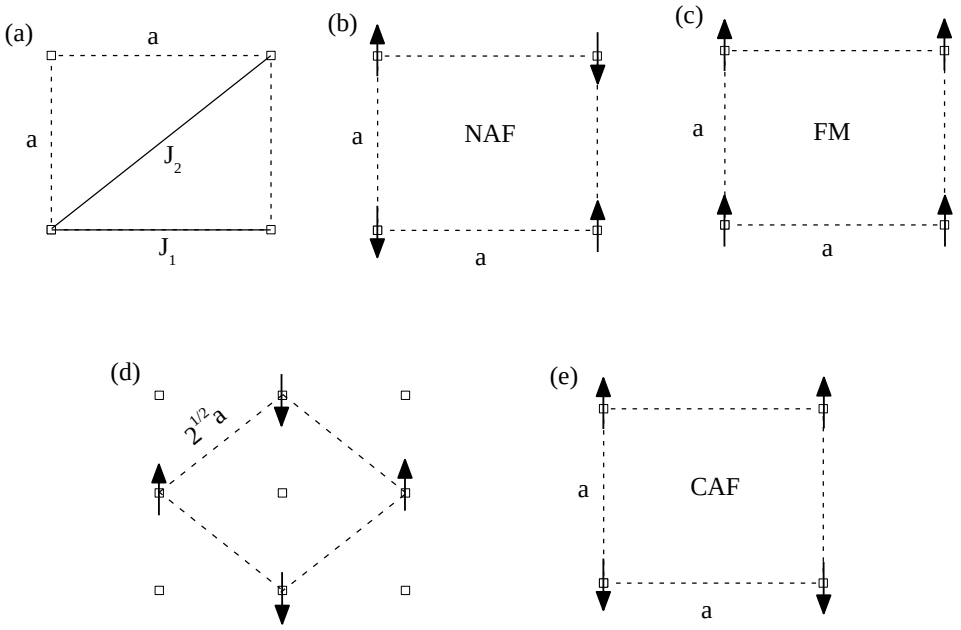

Figure 2.7 (Color online) $J_1 - J_2$ model. (a) The NN exchange interaction J_1 along the side of the square of side 'a' and the NNN exchange interaction J_2 along the diagonal. (b) The Néel AFM ground state with AFM chains arranged antiferromagnetically. (c) The FM ground state with FM chains arranged ferromagnetically. (d) Lattice rotated by 45° is still a square lattice with side $\sqrt{2a}$ (e) Columnar AFM ground state chosen by 'Order by disorder'.

ordered state with short range magnetic correlations due to the geometric frustration. The spin-1/2 Heisenberg square-lattice system in the $J_1 - J_2$ model has received considerable attention. The spin frustration in this model is caused by the competition between the NN J_1 and the NNN J_2. First let us look at the two extreme cases :

(i) $J_2 = 0$ – In this scenario when only the NN are allowed to interact, for an antiferromagnetic (AFM) J_1, the ground state is simply a Néel antiferromagnet (Fig. 2.7b), while for a ferromagnetic (FM) J_1, the ground state is a ferromagnet (Fig. 2.7c).

(ii) $J_1 = 0$ – For an FM interaction along the diagonal, the ground state is again a ferromagnet. But in the case of an AFM J_2, the ground states correspond to FM chains

arranged antiferromagnetically. The lattice can be rotated so as to form configurations which are degenerate in energy (Fig. 2.7d). But thermal/quantum fluctuations can lift the degeneracy in lieu of the phenomena of "Order by disorder" as proposed by Villain [53], and a collinear state (Fig 2.7e) is chosen as a ground state.

In the most general case both J_1 and J_2 are finite. In that case the competing interactions give rise to exotic ground states depending on the frustration ratio $\alpha \sim J_2/J_1$. Based on this ratio, a $J_1 - J_2$ phase diagram (Fig. 2.8) has been proposed from theoretical studies [55][56], which includes three ordered magnetic structures (with the following wavevectors $\vec{Q}$): ferromagnet (FM) ($\vec{Q} = [0, 0]$), Néel antiferromagnet (NAF) ($\vec{Q} = [\pi, \pi]$) and columnar antiferromagnet (CAF) ($\vec{Q} = [\pi, 0]$ or $[0, \pi]$). Classically, first-order phase transitions are expected to occur at the boundaries between these phases, but quantum fluctuations destroy long range magnetic ordering there and instead lead to disordered ground states. The precise nature of the disordered ground state at the boundaries is qualitatively different for ferromagnetic J_1 and antiferromagnetic J_1. For $J_2/J_1 \approx 0.5$ (for the AFM J_1) a gapped spin singlet (dimerized) state, is proposed to exist[57], while the intermediate state for the FM J_1 is suggested to be a gapless nematic state in the region -0.4 $< J_2/J_1 <$ -0.7 from numerical exact diagonalization calculations[56]. On the contrary, recently Richter et al.,[58] pointed out from theoretical studies using a large-scale exact diagonalization of finite lattice up to N = 40 and the coupled cluster method that the CAF state is stable down to J_2/J_1 = -0.4 and the gapless nematic state does not exist. Layered vanadium materials of the type Li_2VOXO_4 (X = Si, Ge) [59] and $AA'VO(PO_4)_2$ (AA' = Pb_2, Zn_2, SrZn, BaCd)[60][61][62] realize this $J_1 - J_2$ model. They fall at different points in the $J_1 - J_2$ phase diagram depending on the parameters $J_c = \sqrt{(J_1^2 + J_2^2)}$, and the angle $\phi = \tan^{-1}(J_2/J_1)$ which determine the extent of frustration in the compounds.

In Chapter 3 we first discuss about localized moment vanadium oxide compounds: $Zn_2VO(PO_4)_2$ which has an Néel AFM LRO ground state with an AFM J_1 and an AFM J_2 and with a weak frustration ($J_2/J_1 \sim$ 0.04), and then a more frustrated scenario ($J_2/J_1 \sim$ -0.9) in $BaCdVO(PO_4)_2$ with a columnar AFM LRO ground state and having an FM J_1 and an AFM J_2 and the evolution of it's magnetic properties under high pressure.

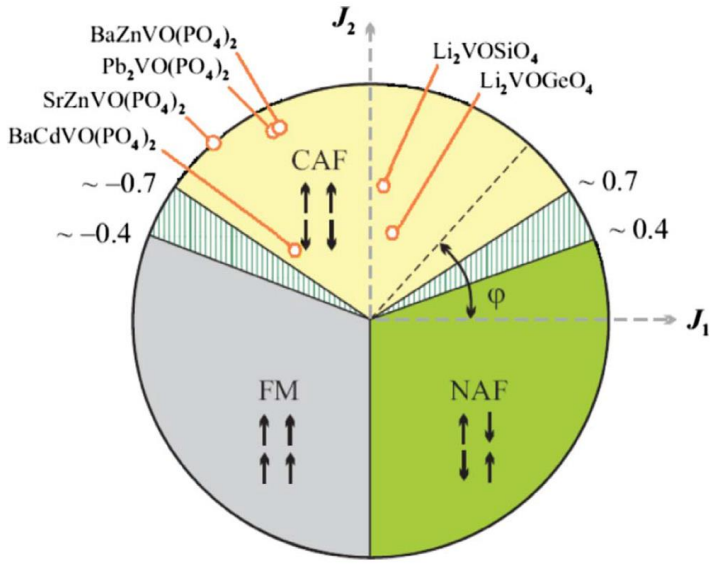

Figure 2.8 (Color online) $J_1 - J_2$ phase diagram[63].

(ii) *Itinerant Quasi-2D Systems*

The study of iron-based superconductors has been a hot topic of research since its discovery in 2008. The ground state of these compounds changes from an antiferromagnetic to a superconducting one on doping and/or on application of pressure. Thus, the antiferromagnetism in the parent compound suggests a connection between superconductivity and the spin dynamics in these systems. Pnictides are layered compounds just like the high-T_c cuprates. The FeAs layers in the pnictides bear resemblance to the CuO_2 layers in cuprates. This layered structure encouraged the modeling of these systems with the Heisenberg $J_1 - J_2$ model with dominant AFM NNN exchange interaction ($J_2 > |J_1|/2$)[64], although with an in-plane anisotropy ($J_{1a} \neq J_{1b}$) in the distorted orthorhombic phase and a finite interplane coupling of these layers ($J_\perp \neq 0$). This model yields a 2-sublattice collinear 'stripe' AFM-type magnetic structure [65]. For the fully isotropic case, with $J_{1a} = J_{1b} \equiv J_1$ (interaction between the two sublattices), degeneracy

and thus frustration should emerge. The anisotropy evidenced in the in-plane NN exchnage coupling ($J_{1a} \neq J_{1b}$) in the pnictides can be perceived intuitively coming from the structural distortion but it is seen that the orthorhombic distortion is less than 1% [66][67]. Thus, the origin of the anisotropy lies somewhere else. Orbital ordering has been held responsible for the strong anisotropy in the exchange interaction.[68]. Another possibility was the effect of a higher-order [biquadratic $(\vec{S}_i \cdot \vec{S}_i)^2$] term in the Hamiltonian [69] which also favors stripe AFM ordering.

Chapter 4 discusses how the magnetic properties of the iron-based superconductor $CaFe_2As_2$ changes under different heat treatments during the preparation of the single crystals on the basis of NMR measurements done.

2.3.2 Frustrated 3D Systems

Frustrated systems in 3D lattices like pyrochlore lattice [70][71], face-centred cubic (fcc) lattice [72], spinels [73] etc. also exhibit fascinating and complex ground states lacking long-range order like spin liquid[70][74], spin glass[75][76], spin ice [77][50] etc. Chapters 5 and 6 demonstrate effects of frustration in lattices with three-dimensional character.

(i) $CoAl_2O_4$

Spinels are compounds with a chemical formula AB_2X_4 where the A-site and the B-site comprise of metal cations and the X-site comprises of anions. When the octahedral B-site is occupied by a magnetic ion the spinel is termed as a B-site spinel[78] ($ZnCr_2O_4$[79][80], $ZnFe_2O_4$[81], Vanadium spinels[82]) with a pyrochlore structure exhibiting frustration. The A-site spinels (spinels with magnetic ion in the tetrahedral A-site), with structure similar to that of a diamond lattice, also show frustration effects. The diamond lattice consists of two interpenetrating fcc lattices displaced along the body diagonal by one quarter of the length of

the diagonal. The nearest neighbor interaction J_1 couples sites in between two separate fcc sublattices [83], whereas the next nearest neighbor interaction J_2 couples sites within a single fcc sublattice. In the presence of ferromagnetic or antiferromagnetic J_1 exclusively, there is no frustration, but a finite antiferromagnetic J_2 introduces frustration in the compound due to presence of competing interactions.

Different A-site spinels exhibit various ground states depending on what the A and B ions are: a spin-orbital ground state below 45 K is proposed in the case of $FeSc_2S_4$ [84][85], an orbital glass state below 10 K for $FeCr_2S_4$ [84][86] and a spin-glass state for $FeAl_2O_4$ (Spin glass transition temperature $T_g = 12$ K) [87][88]. Mn compounds are spin-only systems. $MnSc_2S_4$ shows a spiral magnetic ordering (AFM phase transition temperature $T_N = 2$ K) [84][85][89] while $MnAl_2O_4$ ($T_N = 40$ K) [87][90][91] has a long range antiferromagnetically ordered ground state. $CoRh_2O_4$ ($T_N = 27$ K) [92] and $CoCo_2O_4$ ($T_N = 34$ K) [93][92] both have antiferromagnetic ground states.

Chapter 5 demonstrates the magnetic properties of the ground state of a highly frustrated A-site spinel compound $CoAl_2O_4$ which lies very near to the boundary separating spin liquid ground state and the AFM ordered ground state in the T_c (ordering temperature) vs J_2/J_1 phase diagram proposed theoretically by Bergman[94].

(ii) $BiMn_2PO_6$

As discussed previously in this chapter, LRO is absent in one- and two-dimensional (1D and 2D) Heisenberg systems unlike the three-dimensional (3D) Heisenberg systems. In some cases of quasi-2D materials LRO may still exist. However, interesting physics evolves from spin models which bridge the 1D and the 2D systems, *viz*. Spin Ladders. An n-chain ladder has a structure in between a 1D chain and a 2D square lattice. Let us consider a two-chain (or two-leg) ladder formed by spin-1/2 AFM Ising spins for simplicity. J and J_R are the exchange interactions along the chain and along the rung of the ladder. In the case of $J_R = 0$ and $J \neq 0$, the ground state consists of two decoupled AFM spin chains. In the other extreme case of J=0

and $J_R \neq 0$, the ground state can be perceived as being singlets [95] $S = 0$ $[\frac{1}{\sqrt{2}}(|\uparrow\downarrow\rangle - |\downarrow\uparrow\rangle)]$ and the first excited state is a triplet S =1 $[S_z = +1, |\uparrow\uparrow\rangle$; $S_z = 0$, $\frac{1}{\sqrt{2}}(|\uparrow\downarrow\rangle + |\downarrow\uparrow\rangle)$; S_z = -1, $|\downarrow\downarrow\rangle]$. Theoretically it has been proposed that for coupled n-chain ladders we have a gapless energy spectrum for odd 'n' and a gapped energy spectrum for even 'n' [96][97] (Fig. 2.9). Azuma's

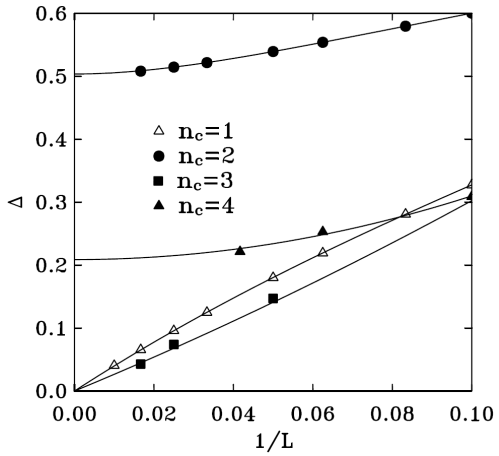

Figure 2.9 (Color online) Spin gap in the energy spectrum, as a function of system size L for open $L \times n_c$ coupled chain[101], where n_c is the number of chains in the spin ladder.

[98] magnetization and NMR results on the S =1/2 two-leg ladder $SrCu_2O_3$ and three-leg ladder $Sr_2Cu_3O_5$ gave an experimental confirmation on the theoretical prediction. The spin-1/2 ladder systems not only exhibit Luttinger liquid Physics [99], but they also pave the way for understanding superconductivity. Superconductivity was reported for the hole doped two-leg ladder compound $Sr_{14-x}Ca_xCu_{24}O_{41}$ [99] under pressure from resistivity measurements. It is natural to think of spin ladders with a higher spin to be more classical in nature and to be simply having an LRO ground state. The spin-5/2 ladder compound $BaMn_2O_3$ [100] provides a strong incentive to focus on high spin ladder compounds. Frustration in this compound, caused by the nearest-neighbor interladder coupling in the high-temperaure orthorhombic phase, is lifted by the structural transition to a low-temperaure monoclinic phase which yielded an AFM ground state below T_N = 184 K. Thus, high-spin ladders might reveal interesting features pertaining to the combined effects of magnetic and structural transitions and further spiced up with

frustration.

With that view, NMR measurements were done on the spin = 5/2 spin ladder $BiMn_2PO_6$ as discussed in Chapter 6.

CHAPTER 3. LOCALIZED FRUSTRATED QUASI-2D SYSTEMS

3.1 $Zn_2VO(PO_4)_2$

This section is based on work submitted for publication[102].

3.1.1 Introduction

$Zn_2VO(PO_4)_2$ is a member of the family of compounds known as the $J_1 - J_2$ model or the frustrated square-lattice (FSL) compound which have been discussed in chapter 2. Its structure consists of $V^{4+}O_5$ square pyramids connected by ZnO_5 square pyramids and PO_4 tetrahedra forming layers perpendicular to the crystallographic c-axis[102][103]. The V-V distance along the c-axis ($\sim$ 4.5 Å) is shorter than that in the ab-plane ($\sim$ 6.3 Å)[103][104][102]. Thus, it was intuitively thought that $J_\perp >> J_{ab}$, where $J_\perp$ and J_{ab} are interplanar and intraplanar exchange coupling strengths. With that idea $Zn_2VO(PO_4)_2$ was proposed to be consisting of quasi-one-dimensional spin chains of VO_6 octahedra, linked by corners along the c-direction [103][104]. But the conclusions from the thermodynamic study of the compound showed contrary result ($J_\perp << J_{ab}$ [105]) and favoured rather a quasi-two-dimensional (2D) scenario. Neutron diffraction study[106] has shown that below $T_N \approx 3.75$ K, while along the ab-plane the magnetic ordering is Néel type antiferromagnetic (AFM), along the c-direction the ordering is ferromagnetic(FM). From the density-functional-theory(DFT)-based calculations also $Zn_2VO(PO_4)_2$ is evidenced to have a spin-1/2 AFM square lattice model[107].

The low-dimensional feature of this system is evident from a broad peak observed in the magnetic susceptibility and a hump in the specific heat around $\sim$ 6.9 K[102]. The magnetic ordering temperature $T_N \approx 3.7$ K, is characterized by a kink in the magnetic susceptibility data and a λ-type anomaly at T_N. Unlike the similar vandates ($BaCdVO(PO_4)_2$ [108],

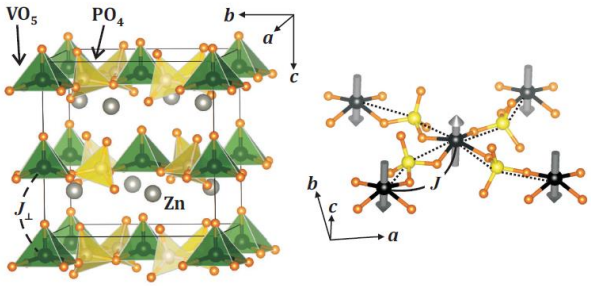

Figure 3.1 (Color online) Structure of $Zn_2VO(PO_4)_2$ [102][103].

$Pb_2VO(PO_4)_2$[109]), $Zn_2VO(PO_4)_2$ does not show a change in T_N with the applied field. From the high-temperature series expansion (HTSE) of the magnetic susceptibility for an FSL model[110], the exchange couplings were evaluated to be J_1 (nearest-neighbor(NN) exchange coupling) $\approx$ 7.8 K, J_2 (next-nearest-neighbor(NNN) exchange coupling) $\approx$ 0.3 K [102][105]. Thus, inspite of the fact that both J_1 and J_2 are both AFM, minimal frustration effect is expected for this system because $J_2/J_1 \sim 0.04$ is pretty small as compared to the values of other members of this family of compounds (Table 3.1). From neutron scattering data[106], the $J_\perp$ is estimated to be around -0.2 K, which is small but not negligible and which is responsible for the long-range ordering (LRO) in this systems below $T_N \approx 3.7$ K. In this following section we present results of ^{31}P-NMR study done on $Zn_2VO(PO_4)_2$ to further invesitigate its ground state and the spin dynamics.

3.1.2 Experimental Details

Polycrystalline sample of $Zn_2VO(PO_4)_2$ was prepared by solid state reaction using ZnO (99.999%) and $NH_4H_2PO_4$ (99.999%) as mentioned in Ref.[102]. The NMR measurements were carried out using pulsed NMR techniques on ^{31}P (nuclear spin I=1/2 and gyromagnetic ratio $\gamma_N/2\pi$= 17.2356 MHz/T) nuclei in the temperature range 1.5 K $\leq T \leq$ 250 K. We have carried out the NMR measurements at two different radio frequencies of 75.5 MHz and 9.4

Table 3.1 Exchange couplings J_1 and J_2 in $J_1 - J_2$ model

Compounds	J_1(K)	J_2(K)	J_2/J_1	References
$Zn_2VO(PO_4)_2$	7.8	0.3	0.04	[102][105]
$VOMoO_4$	110	22	0.2	[111]
$PbVO_3$	203	77	0.4	[112]
Li_2VOSiO_4	3.9	4.3	1.1	[113]
$BaCdVO(PO_4)_2$	-3.6	3.2	-0.9	[108]
$SrZnVO(PO_4)_2$	-7.5	8.6	-1.1	[114]
$Pb_2VO(PO_4)_2$	-5.4	9.3	-1.8	[109]
$BaZnVO(PO_4)_2$	-5	9.3	-1.9	[115]
$PbZnVO(PO_4)_2$	-5.2	10	-1.9	[116]

MHz that correspond to applied fields of about 4.38T and 0.545 T, respectively. Spectra were obtained either by Fourier transform of the NMR echo signals or by sweeping the field at a fixed frequency. The NMR shift $K(T) = (H_{\rm ref} - H(T))/H(T)$ was determined by measuring the resonance field of the sample $[H(T)]$ with respect to nonmagnetic reference H_3PO_4 (resonance field $H_{\rm ref}$). The ^{31}P spin-lattice relaxation rate $1/T_1$ was measured by the conventional single saturation pulse method.

3.1.3 NMR Study

The structure of $Zn_2VO(PO_4)_2$ features one P-site[103]. We observed a narrow spectral line above $T_{\rm N}$ as is expected for an $I = 1/2$ nucleus [118]. Figure 3.2 shows the ^{31}P-NMR spectra measured at different temperatures. The line shape was found to be asymmetric because of the anisotropy in magnetic susceptibility $\chi(T)$ and/or in the hyperfine coupling constant between the P nucleus and the V^{4+} spins. The line position was found to shift with temperature. Temperature dependence of the NMR shift K extracted by fitting the spectra (see inset of Fig. 3.2) are presented in Fig. 3.3(a), which shows a strong anisotropy along different directions. At high temperatures, both isotropic ($K_{\rm iso}$) and axial ($K_{\rm ax}$) parts of the NMR shift vary in a Curie-Weiss manner and then pass through a broad maximum at around 9 K reflecting the 2D short-range order, similar to the $\chi(T)$ data[102].

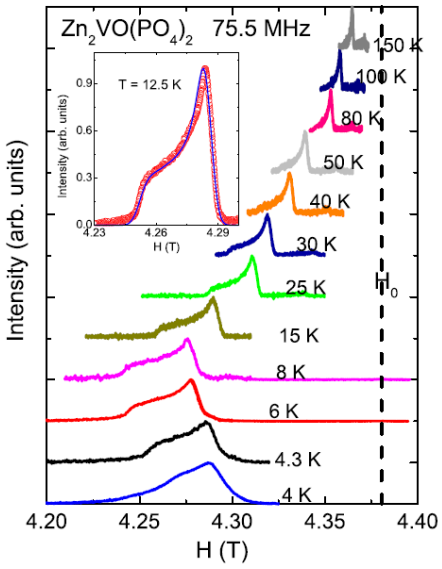

Figure 3.2 (Color online)T dependence of ^{31}P-NMR spectra of $Zn_2VO(PO_4)_2$ at ν = 75.5 MHz.

The NMR shift $K(T)$ is related to the spin susceptibility $\chi_{\rm spin}(T)$ by the relation:

$$K(T) = K_0 + \frac{A_{\rm hf}}{N_{\rm A}}\chi_{\rm spin}(T), \tag{3.1}$$

where K_0 is the temperature-independent chemical shift, and $A_{\rm hf}$ is the hyperfine coupling constant between the P nuclei and the V^{4+} electronic spins. The $K-\chi$ plot with T as an implicit parameter is fitted very well by a straight line [Fig. 3.3(b)] over the whole temperature range ($T > T_{\rm N}$) yielding the isotropic and axial parts of the hyperfine coupling $A_{\rm hf}^{\rm iso}$ = (9221±100) Oe/$\mu_{\rm B}$ and $A_{\rm hf}^{\rm ax}$ = (1010±50) Oe/$\mu_{\rm B}$, respectively. Since the NMR shift is a direct measure of $\chi_{\rm spin}(T)$ and is free from extrinsic impurities, it serves as an independent test for the bulk susceptibility $\chi(T)$. High-temperature series expansion (HTSE) of $\chi_{\rm spin}$ for 2D S =1/2 Heisenberg square lattice is given by Rushbrooke and Wood [117] which can be written as,

$$\chi_{\rm spin}(T) = \frac{N_{\rm A}\mu_{\rm B}^2 g^2}{J} \times [4x + 4 + 2.00025x^{-1} + 0.66656x^{-2} + 0.06286x^{-3} - 0.060434x^{-4} + 0.000237x^{-5}]^{-1} \tag{3.2}$$

where $x = \frac{k_{\rm B}T}{J}$. We fitted the temperature dependence of $K_{\rm iso}$ above 6 K by eqn. 3.1 where

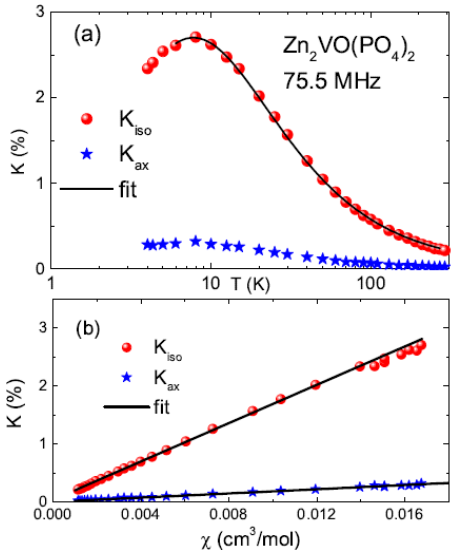

Figure 3.3 (Color online) (a) NMR shift K vs T (b) NMR shift K vs χ at $\nu = 75.5$ MHz.

the expression for $\chi_{\rm spin}$ is given in eqn. 3.2. During the fitting process, $A_{\rm hf}^{\rm iso}$ and g were fixed to the values $g \simeq 1.97$ and $A_{\rm hf}^{\rm iso} \simeq 9221$ Oe/$\mu_{\rm B}$, obtained from the ESR experiments [102] and $K_{\rm iso}$ vs. χ analysis, respectively. In this way, we obtained $K_0 = (0.025 \pm 0.001)$ % and $J/k_{\rm B} = (8.4 \pm 0.3)$ K. The fit to eqn. 3.2 is shown in Fig. 3.3a as a solid black line. The resulting J value is close to the values estimated from the $\chi(T)$ analysis [105] and neutron diffraction experiments [106]. The total hyperfine coupling constant at the P site is the sum of transferred hyperfine ($A_{\rm trans}$) and dipolar ($A_{\rm dip}$) couplings produced by V^{4+} spins, i.e., $A_{\rm hf} = z' A_{\rm trans} + A_{\rm dip}$, where z' is the number of nearest-neighbor V^{4+} spins of the P site. In the crystal structure, squares are formed via V−O−P−O−V superexchange interaction paths. In contrast to $Pb_2VO(PO_4)_2$ where each P atom is coupled to four V^{4+} spins [109] in $Zn_2VO(PO_4)_2$ each P atom is coupled to only two V^{4+} spins (Fig. 3.1), thus, $z' = 2$ for $Zn_2VO(PO_4)_2$. The anisotropic dipolar couplings were calculated using lattice sums to be $A_{\rm a} = 210$ Oe/$\mu_{\rm B}$, $A_{\rm b} = 210$ Oe/$\mu_{\rm B}$, and $A_{\rm c} = -420$ Oe/$\mu_{\rm B}$ along the $a-$, $b-$, and $c-$directions, respectively. Clearly, the value of dipolar coupling is almost negligible compared to the total hyperfine coupling [$A_{\rm hf}^{\rm iso} = (9221 \pm 100)$ Oe/$\mu_{\rm B}$] suggesting that the dominant contribution to the total hyperfine coupling is due to the transferred hyperfine coupling at the P site. The magnitude of this

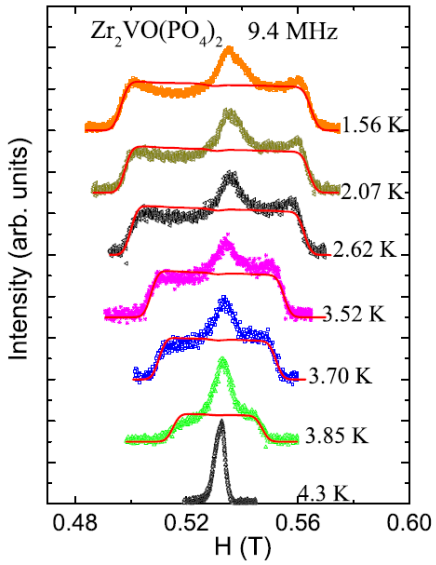

Figure 3.4 (Color online) Temperature-dependent ^{31}P-NMR spectra measured at 9.4 MHz. The solid lines are the fits to the spectra at different temperatures as in [119]. The spectra in the paramagnetic state broaden below $T_{\rm N}$ and take a rectangular shape, due to the internal field $H_{\rm int}$.

coupling depends on the relative orientation and the extent of overlap between the V($3d$), P($2p$), and O($2s$) orbitals.

Below $T_{\rm N}$, the ^{31}P spectra measured at 75.5 MHz were found to broaden abruptly. In order to precisely probe the intrinsic line shape, we remeasured the ^{31}P spectra at a lower frequency of 9.4 MHz. As shown in Fig. 3.4, the ^{31}P line above $T_{\rm N}$ remains narrow and immediately below $T_{\rm N}$ it starts broadening indicating that the P site is experiencing the static internal field in the ordered state through the hyperfine field between the P nuclei and the ordered V^{4+} moments. With decrease in temperature, the spectrum takes a nearly rectangular shape, which reflects that the magnetic ordering is commensurate in nature. If the magnetic structure were incommensurate with the lattice, the internal field would be distributed and the spectrum would not exhibit the rectangular shape seen in Fig. 3.4. Our spectra are, therefore, consistent with the collinear magnetic order determined from the neutron diffraction experiments[106].

The internal field $H_{\rm int}$, which is proportional to the V^{4+} sublattice magnetization, was determined from the fit of the experimental spectra following the procedure adopted recently

for $BiMn_2PO_6$ [120]. The temperature dependence of H_{int} is plotted in Fig. 3.5. In order to extract the critical exponent (β) of the order parameter (sublattice magnetization), $H_{int}(T)$ was fitted by the power law:

$$H_{int} = H_0\left(1 - \frac{T}{T_N}\right)^{\beta} \tag{3.3}$$

One can notice that H_{int} decreases sharply on approaching T_N. We have estimated β by fitting the data points as close to T_N as possible (i.e., in the critical region) as shown in Fig. 3.5. The maximum value of $\beta = 0.33 \pm 0.02$ with $T_N \simeq 3.9(1)$ K was obtained by fitting the data points in the T-range 3.7 K to 3.95 K close to T_N. By increasing the number of fitting points toward low-Ts, the β value was found to decrease. At low-Ts, H_{int} develops the tendency of saturation. The critical exponent reflects the universality class of the spin system. The values expected for different spin- and lattice-dimensionalities are listed in Table II of [109]. The value of β obtained from the experiment is 0.33, which would be consistent with any of the 3D spin models (Heisenberg, Ising, or XY). Given the fact that below T_N spins are aligned with the c direction [106] we may expect a weak uniaxial anisotropy, but it is impossible to quantify this putative anisotropy using the data at hand. Interestingly, the critical behavior of $Zn_2VO(PO_4)_2$ deviates from that of other square-lattice V^{4+} antiferromagnets, where $\beta \simeq 0.25$ (2D XY universality class) was systematically observed in Li_2VOSiO_4 and Li_2VOGeO_4 [121][113][122], $Pb_2VO(PO_4)_2$ [109][123][124], $SrZnVO(PO_4)_2$ [125] [114], and other compounds [124]. The ^{31}P nuclear spin-lattice relaxation rate $1/T_1$ above T_N was measured at the field corresponding to the central peak position. For $T < T_N$, the measurements were performed at both the central peak position as well as at the right-hand side (RHS) edge position (see Fig. 3.4). For an $I = 1/2$ nucleus, the recovery of the longitudinal magnetization is expected to follow a single-exponential behavior. In $Zn_2VO(PO_4)_2$, the recovery of the longitudinal nuclear magnetization was indeed fitted well by the exponential function $1 - \frac{M(t)}{M_0} = Ae^{-t/T_1}$, where $M(t)$ is the nuclear magnetization at a time t after the saturation pulse and M_0 is the equilibrium magnetization. The temperature dependence of $1/T_1$ extracted from the fit is presented in Fig. 3.6. The $1/T_1$ data measured at two different frequencies (75.5 MHz and 9.4 MHz) almost resemble each other at low temperatures. At high temperatures ($T \geq 10$ K), $1/T_1$ is temperature-independent. In the high temperature limit $T >> J/k_B$, a temperature-independent $1/T_1$ behavior is typical

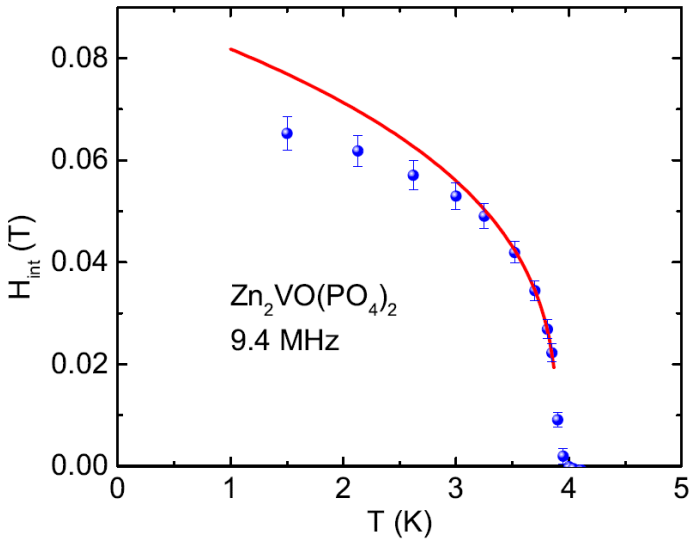

Figure 3.5 (Color online) Temperature dependence of the internal field $H_{\rm int}$ obtained from NMR spectra measured at 9.4 MHz in the ordered state. $H_{\rm int}$ is proportional to the V^{4+} sublattice magnetization. The solid line is the fit by eqn. 3.3 as described in the text.

due to random fluctuation of paramagnetic moments [126]. With decrease in temperature, $1/T_1$ decreases slowly for $T < 10$ K and then shows a weak anomaly around $T_{\rm N} \simeq 3.8$ K. This decrease is very similar to that observed previously in the cases of the antiferromagnetic square lattices $Pb_2VO(PO_4)_2$ [109], $SrZnVO(PO_4)_2$ [114] $VOMoO_4$, and $[Cu(HCO_2)_2.4D_2O]$, where the decrease of $1/T_1$ above $T_{\rm N}$ is explained by cancellation of the antiferromagnetic spin fluctuations at the probed nuclei [127] . Below the peak, $1/T_1$ again decreases smoothly towards zero. As shown in Fig. 3.6 no difference in $1/T_1$ below $T_{\rm N}$ was observed between the data measured at the central peak and RHS edge positions at 9.4 MHz.

In the AFM ordered state, $1/T_1$ is mainly driven by scattering of magnons off nuclear spins, leading to a power-law temperature dependence [128][122]. For $T >> \Delta/k_{\rm B}$, where Δ is the energy gap in the spin-wave spectrum, $1/T_1$ either follows a T^3 behavior due to a two-magnon Raman process or a T^5 behavior due to a three-magnon process, while for $T << \Delta/k_{\rm B}$, it follows an activated behavior $1/T_1 \propto T^2 \exp(-\Delta/k_{\rm B}T)$. As seen from Fig. 3.6 our ^{31}P $1/T_1$ data in the lowest temperature region (1.5 K $\leq T \leq$ 3.25 K) follow the T^5 behavior rather

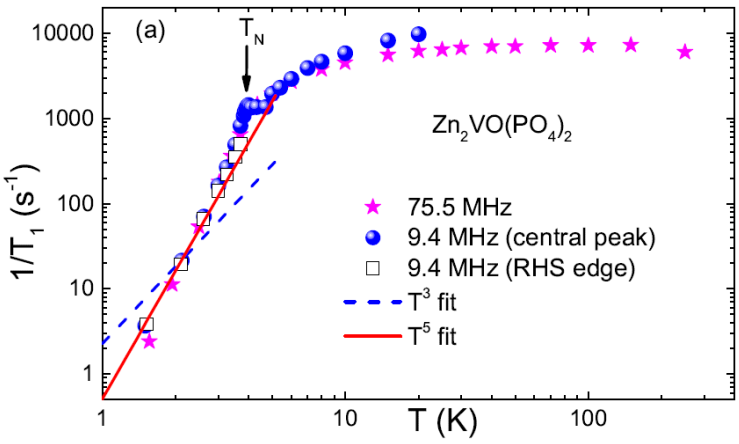

Figure 3.6 (Color online) Spin-lattice relaxation rate $1/T_1$ vs. temperature T measured at 75.5 MHz and 9.4 MHz. Two data sets at 9.4 MHz correspond to the measurements at both the central peak and RHS edge positions below T_N [see Fig. 3.4]. The solid and dashed lines represent T^5 and T^3 behaviors, respectively.

than the T^3 behavior suggesting that the relaxation is mainly governed by the three-magnon process. The lack of activated behavior down to 1.5 K indicates that the upper limit of Δ/k_B is 1.5 K.

At sufficiently high temperatures, $1/T_1$ due to local moments is T-independent and can be expressed within the Gaussian approximation of the auto-correlation function of the electronic spin as[126] :

$$\left(\frac{1}{T_1}\right)_{T\to\infty} = \frac{(\gamma_N g\mu_B)^2\sqrt{2\pi}z'S(S+1)}{3\omega_E}\left(\frac{A_{hf}^a}{z'}\right)^2 \tag{3.4}$$

where $\omega_E = [\max(|J_1|,|J_2|)k_B/\hbar]\sqrt{2zS(S+1)/3}$ is the Heisenberg exchange frequency, z is the number of NN spins of V^{4+} ion, z' is the number of nearest-neighbor V^{4+} spins for a given P site. The z' in the numerator takes into account the number of nearest-neighbor V^{4+} spins responsible for producing fluctuations at the P site. Using the relevant parameters, $A_{hf} \simeq 9221$ Oe/μ_B, $\gamma_N = 1.08\times10^8$ rad s^{-1} T^{-1}, $z = 4$, $z' = 2$, $g = 2$, $S = 1/2$, and the high-temperature (150 K) relaxation rate of $\left(\frac{1}{T_1}\right)_{T\to\infty} \simeq 7270.6$ s^{-1} for the P site in eqn. 3.4, the magnitude of the exchange coupling is calculated to be $J \simeq 9$ K in good agreement with $J \simeq 7.7$ K determined

from the thermodynamic data [102].

One can see in Fig. 3.6 that for $T > 10$ K a slight increase in $1/T_1$ was observed at 9.4 MHz compared to the data measured at 75.5 MHz. In order to check whether this difference is due to the effect of spin diffusion, we measured $1/T_1$ at different applied fields at $T = 15$ K. Long-wavelength ($q \sim 0$) spin fluctuations in a Heisenberg magnet show diffusive dynamics. In 1D compounds, such spin diffusion results in a $1/\sqrt{H}$ magnetic field dependence of $1/T_1$, which has been observed in $(CH_3)_4NMnCl_3$, $CuCl_2.2NC_5H_5$, and Sr_2CuO_3 [129][130][131]. On the other hand, in 2D materials $1/T_1$ varies as $\log(1/H)$ [132]. In Fig. 3.7, $1/T_1$ is plotted against $-\log H$. A weak field dependence is observed. It can be fitted by the form $1/T_1 = a + \log(1/H)$, where a is a constant. The linearity of the $1/T_1$ vs. $\log(1/H)$ dependence supports the 2D nature of the compound. As shown in Fig. 3.8, $1/(\chi T_1 T)$ above 10 K is T-independent and

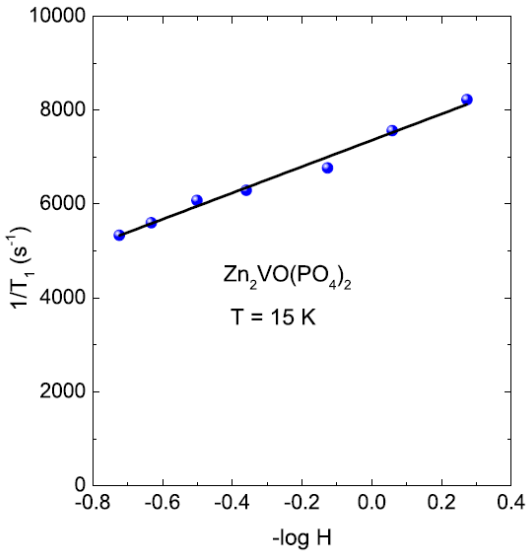

Figure 3.7 (Color online) $1/T_1$ vs. $-\log_{10}H$ measured at $T = 15$ K for $Zn_2VO(PO_4)_2$. The solid line is the fit by $1/T_1 = a + \log_{10}(1/H)$.

increases slowly below 10 K where the system begins to show antiferromagnetic short-range order. The general expression for $1/T_1T$ in terms of the dynamic susceptibility $\chi_M(\vec{q}, \omega_0)$:

$$\frac{1}{T_1 T} = \frac{2\gamma_N^2 k_B}{N_A^2} \sum_{\vec{q}} |A(\vec{q})|^2 \frac{\chi''_M(\vec{q}, \omega_0)}{\omega_0} \tag{3.5}$$

where the sum is over wave vectors $\vec{q}$ within the first Brillouin zone, $A(\vec{q})$ is the form factor of the hyperfine interactions as a function of $\vec{q}$, and $\chi''_{\rm M}(\vec{q},\omega_0)$ is the imaginary part of the dynamic susceptibility at the nuclear Larmor frequency ω_0. For $q = 0$ and $\omega_0 = 0$, the real component of $\chi'_{\rm M}(\vec{q},\omega_0)$ corresponds to the uniform static susceptibility χ. Thus the temperature-independent $1/T_1T$ above 10 K in Fig. 3.8 demonstrates the dominant contribution of χ to $1/T_1T$. On the other hand, a slight increase of $1/T_1T$ below 10 K indicates the growth of antiferromagnetic correlations with decreasing T. The symmetric location of phosphorous between the two

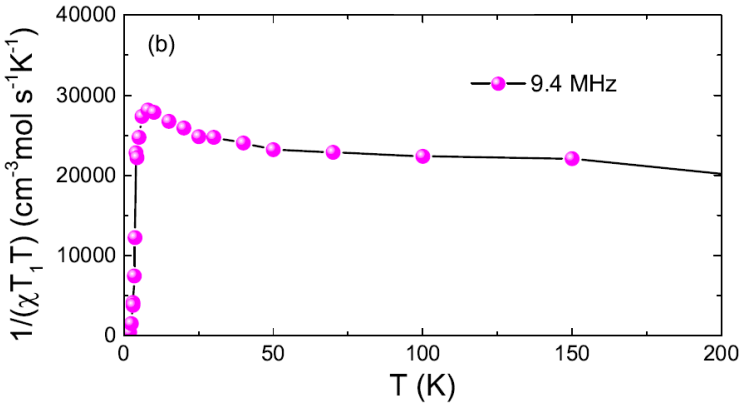

Figure 3.8 (Color online) $1/\chi T_1T$ is plotted as a function of T at $\nu = 9.4$ MHz.

V^{4+} spins implies that Nèel type AFM spin fluctuations $[\vec{q} = (\pm\pi/a, \pm\pi/b)]$ from neighboring spins should be largely filtered out ($|A(\vec{q})|^2 = 0$) because the P nuclei interact with V^{4+} spins having opposite directions (Fig. 3.1). When the coupling to the two V^{4+} spins is equivalent, the AFM fluctuations do not contribute to $1/T_1T$. The residual enhancement of $1/T_1T$ below 10 K reflects the asymmetry of the hyperfine couplings. This asymmetry is consistent with the crystal structure of $Zn_2VO(PO_4)_2$, where the P atoms are located on mirror planes running perpendicular to the $(a + b)$ or (a) crystallographic directions. The tensor of hyperfine couplings may change its orientation upon the reflection in the mirror plane, thus leading to non-equivalent interactions between P and the up- and down-spins on the neighboring V^{4+}

ions.

Another point to be noted here is that in the ^{31}P-NMR spectrum (Fig. 3.4), the central line does not disappear completely even at the lowest measured temperature. NMR experiments on many other compounds, especially on powder samples, are reported to show similar coexistence of the high-T and low-T phases, e.g., in $BaCuP_2O_7$ [133], (Li,Na)VGe_2O_6 [134][135][136], $(Ca_4Al_2O_6)Fe_2(As_{1-x}P_x)_2$ [137], and $BiMn_2PO_6$ [120]. One could argue that the coexistence of two phases is due to a spread of the transition temperatures within the polycrystalline sample, but in such a case it is quite unlikely to observe a distinct peak in the temperature dependence of $1/T_1$, as seen in Fig. 3.6. One possible origin of the central line is the impurity phases. In order to check that, we measured $1/T_1$ below T_N at the positions corresponding to the central peak and the RHS edge of the spectra. The magnitude and the temperature dependence of $1/T_1$ at both positions are the same, which clearly suggests that the central peak is an intrinsic feature of the sample and completely rules out the contribution of impurity phases. Another possible origin of the central line could be the presence of crystal defects or local dislocations in the polycrystalline sample.

3.1.4 Conclusion

$Zn_2VO(PO_4)_2$ is a quasi-2D AFM square lattice with weak frustration due to AFM NNN in-plane exchange coupling J_2 and with a very small FM interplane exchange coupling. Growth of short-range magnetic correlations is evidenced from a broad maxima in both K_{iso}-T and K_{ax}-T plots at ∼9 K and from the increase of $1/T_1T\chi$ above T_N. The compound exhibits long-range ordering below the magnetic transition temperature $T_N \simeq 3.75$ K. ^{31}P-NMR spectra shows the presence of a commensurate magnetic order in the system. From the dynamic NMR study done the it is evident that in the ordered state relaxation is mainly driven by the three-magnon process. A 2D nature of $Zn_2VO(PO_4)_2$ is clear from the field dependence of $1/T_1$.

3.2 $BaCdVO(PO_4)_2$

The ambient-pressure NMR study in this section is based on the work published in [62].

3.2.1 Introduction

As discussed in chapter 2, the theoretically proposed $J_1 - J_2$ phase diagram has interesting aspects especially near the phase boundaries between long-range ordered (LRO) states[109]. While many compounds have been found to realize the LRO states [108][111] [Ferromagnetic (FM), Néel Antiferromagnetic (NAF), and the Columnar Antiferromagnetic (CAF) ground states], no compound has been observed to fall in the exotic phases separating these LRO states. For $J_2/J_1 \approx 0.5$ (for the AFM J_1) a gapped spin singlet (dimerized) state, is proposed to exist[138], while the intermediate state for the FM J_1 is suggested to be a gapless nematic state in the region -0.4 $< J_2/J_1 <$ -0.7 from numerical exact diagonalization calculations[139]. On the contrary, recently Richter et al.,[140] pointed out from theoretical studies using a large-scale exact diagonalization of finite lattice up to N = 40 and the coupled cluster method that the CAF state is stable down to J_2/J_1 = -0.4 and the gapless nematic state does not exist. Thus, apart from the fact that these phase boundaries provide huge opportunity for the study of quantum spin liquid state[141], there lies a theoretical disagreement as to what are the zero-temperature properties of the CAF-FM phase boundary.

$BaCdVO(PO_4)_2$, a member of the family of the vanadium phosphates, has a layered crystal structure (Fig. 3.9) with a slightly distorted [142] square lattice arrangement of V^{4+} ($3d^1$, spin $S = 1/2$) cations. This compound has attracted much interest since it is considered to be a prototype of the bond-frustrated $S = 1/2$ square lattice in the J_1-J_2 model. The exchange interactions between V^{4+} spins in $BaCdVO(PO_4)_2$ were reported [108] to be $J_1 \approx$ -3.62 K (ferromagnetic) and $J_2 \approx$ 3.18 K (antiferromagnetic, AFM) from magnetic susceptibility and magnetization measurements. Long-range AFM ordering at $T_N \approx 1$ K was reported from specific heat [108], magnetization [108][143] and muon spin resonance [124]. Based on the ratio $J_2/J_1 \approx$ -0.88, the system is located close to the debatable phase boundary between CAF and the gapless nematic phase[108]. In order to tune the ratio J_2/J_1, one can think of application

of a high pressure (p). Up to now, the only reported high pressure study for the J_2/J_1 model was on $Li_2VO(SiO_4)$ ($J_2/J_1 = 1.1$ with $J_1 + J_2 = 8.2$ K) in which the ratio J_2/J_1 was reported to decrease by about 40% at $p = 7.6$ GPa [144]. This triggered the interest in investigating the ground state properties of $BaCdVO(PO_4)_2$ under ambient pressure and its evolution with pressure with the help of the tool of NMR. We first discuss its magnetic properties under ambient pressure and then show the effect pressure has on its magnetic properties.

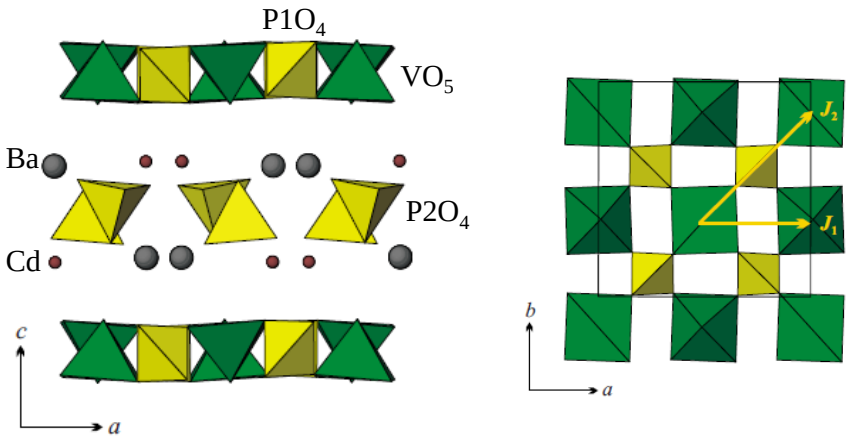

Figure 3.9 (Color online)Structure of $BaCdVO(PO_4)_2$ [108]

3.2.2 Experimental Details

Polycrystalline samples of $BaCdVO(PO_4)_2$ were synthesized by solid-state reaction using $BaCO_3$, CdO, V_2O_3, V_2O_5 and $(NH_4)_2HPO_4$ with at least 99.9% purity. Details of the sample preparation are given in Ref.[108]. The NMR measurements were conducted using pulsed NMR techniques on ^{31}P nuclei with nuclear spin $I = 1/2$ and gyromagnetic ratio $\gamma_N/2\pi = 17.2356$ MHz/T in the T range 0.1 K$\leq T \leq$300 K using a ^{3}He-^{4}He dilution refrigerator (Kelvinox MX100, Oxford instruments) installed at Ames Laboratory. A hybrid Be-Cu/NiCrAl clamp-

type high-p cell (discussed in Chapter 1) was used to produce high pressure (p) on the sample up to 2.3 GPa at room temperature. Daphne oil 7373 was used as the p-transmitting medium. The sample pressure was calibrated using ^{63}Cu nuclear quadrupole resonance (NQR) measurements of Cu_2O based on the p and T dependences of the Cu-NQR frequency reported previously [145][146]. Figure 3.10 shows a typical example of T dependence of the sample p for our pressure cell at four different pressures. The sample p decreases by about 0.25 GPa upon cooling from room temperature to around 100 K. Below 100 K, the sample pressure is almost independent of T. The NMR spectra were obtained by plotting the spin echo signal intensity with sweeping the magnetic field at a constant frequency ν. The nuclear spin lattice relaxation rate $1/T_1$ was measured at the P2 site by the single saturation pulse method and determined by fitting the recovery curves versus time τ with a single exponential function exp[-(τ/T_1)]. In the case that this function did not work due to inhomogeneous distribution of $1/T_1$, we determined the representative value of $1/T_1$ by using a stretched exponential function exp[-$(\tau/T_1)^{\alpha}$].

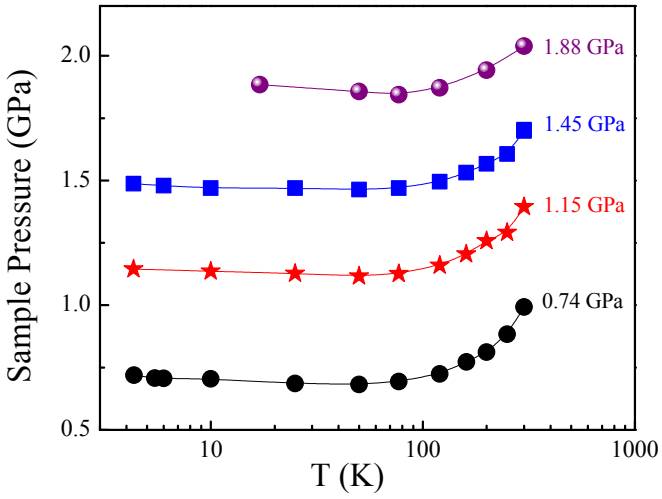

Figure 3.10 (Color online) Temperature profile of the sample pressure for the pressure cell used.

3.2.3 NMR Study under Ambient Pressure

Figure 3.11 shows the ^{31}P-NMR powder spectrum at frequency $\nu = 70.3$ MHz at various temperatures. From the NMR viewpoint an important difference between the structure of

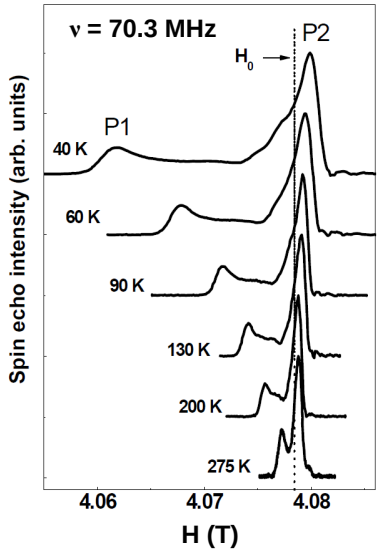

Figure 3.11 (Color online) ^{31}P-NMR spectra at different temperatures. The vertical line corresponds to the Larmor field H_0 determined by the reference sample H_3PO_4.

$Zn_2VO(PO_4)_2$ and that of $BaCdVO(PO_4)_2$ is the presence of two crystallographically inequivalent P sites, P1 and P2 (Fig. 3.9) in the latter. The $[VOPO_4]$ layers, which extend parallel to the ab-plane, are formed by the corner-sharing $V^{4+}O_5$ pyramids with $P1O_4$ tetrahedra while the other P-site forms isolated $P2O_4$ tetrahedra lying between the $[VOPO_4]$ layers. The two P-sites give rise to two distinct lines in the ^{31}P-NMR spectrum which is similar to observed spectra in isostructual $Pb_2VO(PO_4)_2$ [109] and $SrZnVO(PO_4)_2$[114]. The narrow line around the Larmor field H_0 can be assigned to the P2 site lying between vanadium layers and the other broad line is from the strongly-coupled P1 site. Each line has a characteristic shape of the anisotropic powder pattern. With decreasing temperature, both lines broaden and the broad line shifts to lower magnetic field, while the narrow line shifts to slightly higher magnetic field. Figure 3.12 shows temperature (T) dependences of the NMR shifts K. For the P1 site, the shifts along the $a-$ and $b-$axes are the same within our experimental uncertainty

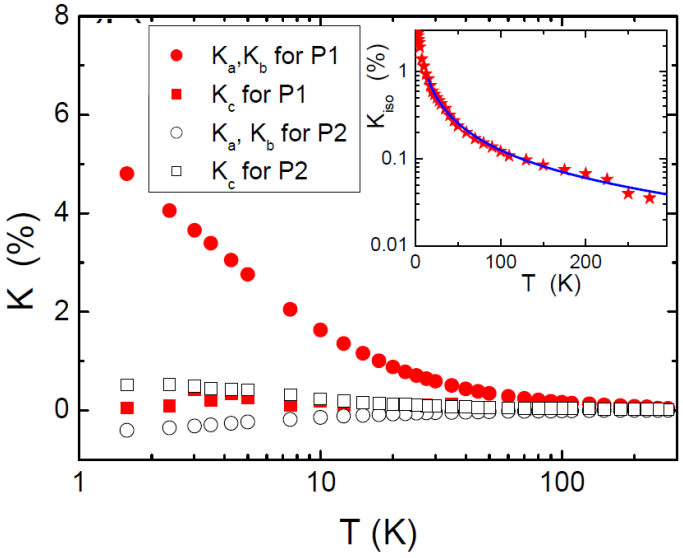

Figure 3.12 (Color online) Temperature dependence of the NMR shift K (a, b and c axes) for each P site. The inset shows temperature dependence of $K_{\rm iso}$ for the P1 site. The solid line is the fit of $K_{\rm iso}$ by Eqs. (2) and (3).

and strongly positive and the shift along the $c-$axis is very small. For the P2 site, there is a relatively small negative shift along the $a-$ (and $b-$) axis and a small positive shift along the $c-$axis. The NMR shift varies linearly with the spin susceptibility χ, and $K(T)$ can be generally expressed in terms of $\chi(T)$ as :

$$K(T) = K_0 + \frac{H_{\rm hf}}{\mu_{\rm B} N_{\rm A}} \chi(T), \tag{3.6}$$

where K_0 is the temperature-independent chemical (orbital) shift, $N_{\rm A}$ is the Avogadro number, $H_{\rm hf}$ is the hyperfine field at the P site in Oe produced by the V^{4+}, $S = 1/2$ spins and $\chi/N_{\rm A}$ is expressed in units of $\mu_{\rm B}$/(Oe spin). Shown in Fig. 3.13 is the $K-\chi$ plot with T as the implicit parameter. From the slope of the $K-\chi$ plot, the hyperfine fields at the P sites are estimated to be $H_a = H_b = (3045 \pm 32)$ Oe and $H_c = (149 \pm 21)$ Oe for P1 site. For P2, $H_a = H_b = -(264 \pm 2)$ Oe and $H_c = (378 \pm 6)$ Oe. The isotropic hyperfine field $H_{\rm iso}[= (H_a + H_b + H_c)/3]$ is then (2080 ± 28) Oe for P1 and $-(50 \pm 3)$ Oe for P2. This was expected since from the structure of $BaCdVO(PO_4)_2$, the P1 site is strongly coupled and the P2 site weakly coupled to the V^{4+} spin [108]. The isotropic component originates from the isotropic transferred hyperfine interaction

(THI) from the V spin moments. The THI between the V and P1 ions is coming from the P($3s$)-O($2p$)-V($3d$) covalent bond in the [$VOPO_4$] layers. The THI at the P2 site evidences that the V $3d$ spins polarize the $3s$ electron spins at the P2 site via covalent bonds between the O and P atoms, which will be responsible for three-dimensional magnetic interactions in the system. These hyperfine fields are compared with $H_a = (1882 \pm 40)$ Oe, $H_b = (1251 \pm 42)$ Oe and $H_c = -(1642 \pm 55)$ Oe for P1 site in the isostructural $Pb_2VO(PO_4)_2$ and its anisotropy in $ab-$plane is due to the distortion in the square lattice with lower crystal structure [109]. On the other hand we did not detect any anisotropy in the $ab-$plane in $BaCdVO(PO_4)_2$ within our experimental resolution. This indicates that the structural deviation from the square lattice is smaller in $BaCdVO(PO_4)_2$ than in $Pb_2VO(PO_4)_2$ which is consistent with the results from the band structure calculations [142] where J_1'/J_1 and J_2'/J_2 for $BaCdVO(PO_4)_2$ are almost equal to unity where J_1 and J_1' make up the NN exchange couplings along the edges perpendicular to each other and J_2 and J_2' are the exchange couplings along the two diagonals of the square lattice. Figure 3.14 shows the temperature dependence of the ^{31}P-NMR spectrum below 4 K

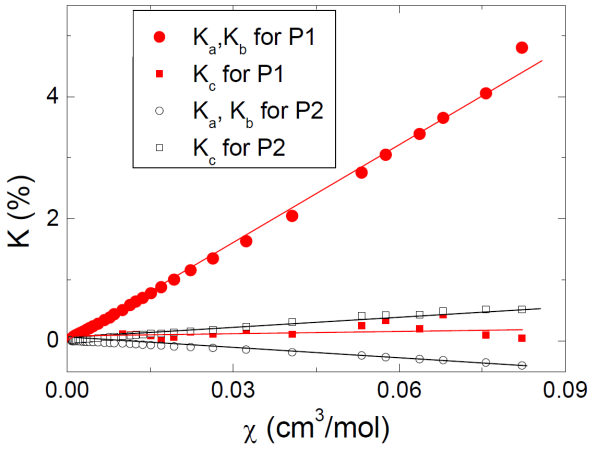

Figure 3.13 (Color online) $K - \chi$ plot for all three orientations for each P site.

at $\nu = 13.8$ MHz. The P1-NMR line was found to broaden abruptly below $T_N \sim 1.05$ K and shoulder-like features are observed on either side of the P2 line. The broadening of the lines is due to the presence of the internal field at the P sites. The symmetric broadening indicates staggered moments in the antiferromagnetically ordered state below T_N which is consistent

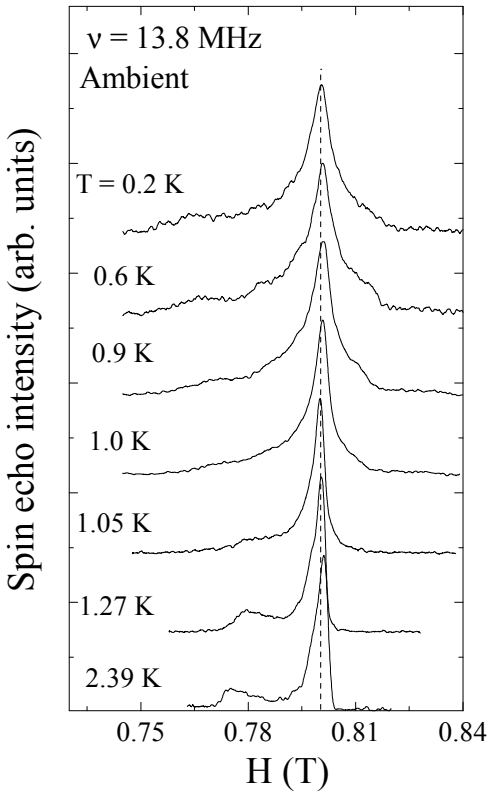

Figure 3.14 (Color online) ^{31}P-NMR field-swept spectrum at ν = 13.8 MHz under ambient pressure. The dotted line is the position of the Larmor field H_0. Below T_N = 1.05 K, a symmetric broadening is seen due to AFM ordering of the V spins.

with the CAF ordered state. Fig. 3.15 shows the temperature dependence of the internal field ($H_{\rm int}$) at the P2 site measured at ν = 46 MHz, where a sudden increase of $H_{\rm int}$ just below T_N can be observed. $H_{\rm int}$ has been estimated by subtracting the line-width just above T_N from the observed line-width below T_N =1.04 K. Since the $H_{\rm int}$ is proportional to the V^{4+} sublattice magnetization, it is possible to estimate a critical exponent for the magnetic transition which depends on the spin and lattice dimensionalities. The critical exponent β is, as shown by red line in the figure, roughly estimated to be 0.35 by fitting the data with the power law $H_{\rm int}(T) = H_0(1-T/T_N)^{\beta}$. Although it is relatively difficult to determine the precise value of β, we can say

that the β value is close to that for a 3-dimensional Heisenberg model ($\beta = 0.33$-0.367) [147][148] rather than that for a 2-dimensional XY model ($\beta = 0.231$) [149] as shown by black line. Thus we consider the magnetic phase transition has a 3-dimensional nature. Figure 3.16 shows the

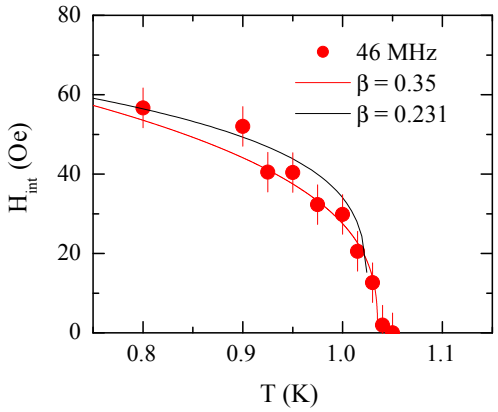

Figure 3.15 (Color online) Internal field $H_{\rm int}$ calculated from the line-width of the spectrum. The lines are fits to eqn. : $H_{\rm int}(T) = H_0(1 - T/T_{\rm N})^{\beta}$. The solid red line corresponds to $\beta = 0.35$ and the dotted black line corresponds to $\beta = 0.231$.

temperature dependence of the ^{31}P-nuclear spin-lattice relaxation rate $1/T_1$ measured at the peak position of the narrow line (P2 site). Above 2 K, $1/T_1$ is temperature-independent due to the exchange-narrowed hyperfine interactions between the V spin moments in the paramagnetic state. With lowering temperature close to $T_{\rm N} = 1.05$ K, $1/T_1$ increases and shows a divergent behavior due to critical slowing down of spin fluctuations. As shown in the inset of Fig. 3.16 the divergent behavior of $1/T_1$ is approximately fitted by $1/T_1 \sim \epsilon^{-\alpha}$ with $\epsilon = (T - T_{\rm N})/T_{\rm N}$ ($T_{\rm N} = 1.05$) and α is estimated to be 0.77 ± 0.04 which, within the error bar, is equal to the value of 0.8 expected for a two-dimensional (2D) Heisenberg system.

In general, critical fluctuations at the antiferromagnetic wave vector dominate near the antiferromagnetic ordering temperature. To see these effects, it is useful to re-plot the data by changing the vertical axis from $1/T_1$ to $1/T_1T\chi$ as shown in Fig 3.17. $1/T_1T$ can be expressed

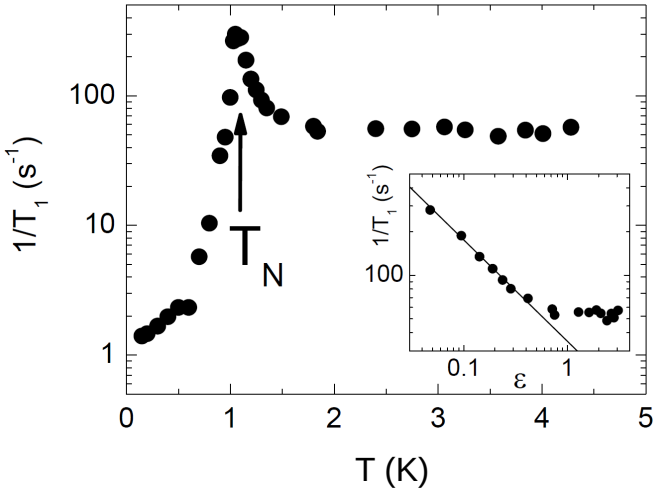

Figure 3.16 (Color online) Temperature dependence of $1/T_1$ for the P2 site at 13.8 MHz. The inset shows the plot of $1/T_1$ vs $\epsilon = (T - T_{\rm N})/T_{\rm N}$. The solid line is a fit as described in the text.

in terms of the dynamic susceptibility $\chi_{\rm M}(\vec{q},\omega_0)$ per mole of electronic spins as [109][150]:

$$\frac{1}{T_1 T} = \frac{2\gamma_N^2 k_{\rm B}}{N_{\rm A}^2} \sum_{\vec{q}} |A(\vec{q})|^2 \frac{\chi''_{\rm M}(\vec{q},\omega_0)}{\omega_0} \tag{3.7}$$

where the sum is over the wave vectors $\vec{q}$ within the first Brillouin zone, $A(\vec{q})$ is the form factor of the hyperfine interactions and $\chi''_{\rm M}(\vec{q},\omega_0)$ is the imaginary part of the dynamic susceptibility at the Larmor frequency ω_0. A plot of $1/T_1 T\chi$ versus T shows the relative magnitude of $\sum_{\vec{q}} |A(\vec{q})|^2 \chi''_{\rm M}(\vec{q},\omega_0)$ as compared to the uniform susceptibility $\chi(0,0)$. For high temperatures above 3 K, $1/T_1 T\chi$ is a constant showing that the temperature dependence of $\sum_{\vec{q}} |A(\vec{q})|^2 \chi''_{\rm M}(\vec{q},\omega_0)$ is equivalent to that of $\chi(0,0)$. With decrease in temperature, $1/T_1 T\chi$ starts to increase. This implies dominance of $\sum_{\vec{q}} |A(\vec{q})|^2 \chi''_{\rm M}(\vec{q},\omega_0)$ over $\chi(0,0)$, which is due to a growth of antiferromagnetic correlations. Thus we conclude that 2D antiferromagnetic spin fluctuations play an important role for driving the long range antiferromagnetic ordering in the system. Since the AFM ordered state must be columnar type, it is most likely that the spin correlations originate from the $\vec{q} = Q_{\rm CAF}$ component.

Below $T_{\rm N}$, $1/T_1$ in Fig. 3.16 decreases sharply and levels off at low temperatures below

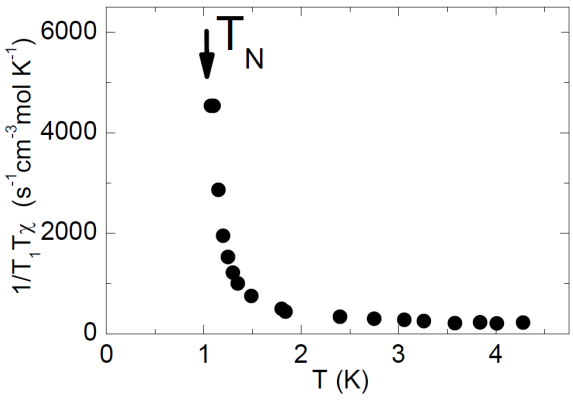

Figure 3.17 (Color online) $1/T_1T\chi$ plotted as a function of temperature.

$\sim$ 0.3 K. Similar behavior is observed in the temperature dependence of the muon relaxation rate λ in $BaCdVO(PO_4)_2$ [124]. The constant relaxation rates at low temperatures indicate temperature-independent spin fluctuations, which is characteristic of a frustrated spin system with a degenerate ground state.

3.2.4 NMR Study under High Pressure

The essence of our results are summarized in Fig. 3.18, the first established magnetic phase diagram of $BaCdVO(PO_4)_2$ under pressure. The magnetic transition temperature, T_N, slightly increases with increasing magnetic field, H, and is reduced with further increase of H and finally suppressed completely above a magnetization saturation field $H_S \approx 4.2$ T at $T = 0.5$ K under ambient pressure [108]. With the application of high pressure (p), although T_N varies only slightly with p at low magnetic fields, H_S ($T = 0.1$ K) decreases drastically to 2.9 T under $p = 0.74$ GPa and to 0.7 T under $p = 2.05$ GPa. The extrapolation to a higher pressure indicates that H_S should vanish at $p \approx 2.35$ GPa. From the $J_1 - J_2$ analysis (shown later) we suggest that there is no signature of gapless nematic state for $|J_2/J_1|$ down to 0.62.

Broadening of the NMR lines below T_N similar to the case under ambient pressure is observed under high pressures indicative of the CAF ordered state under pressure. Under high p, the spectrum remains almost similar except for a noticable change in the NMR shift. The NMR

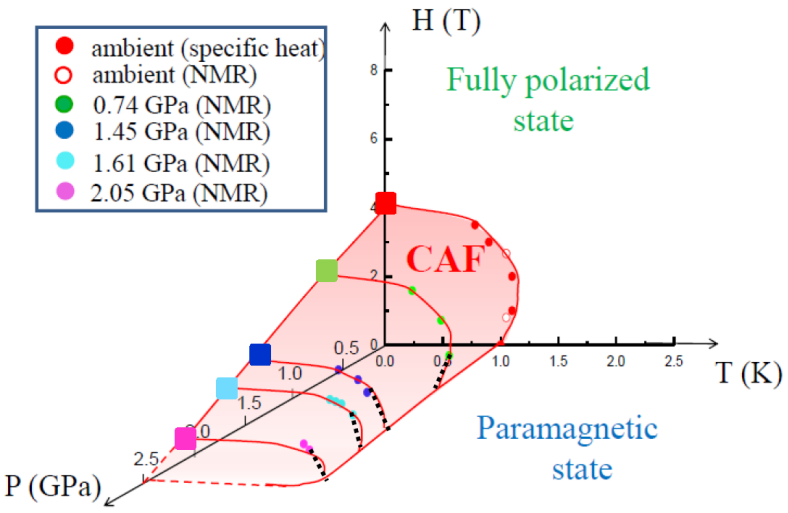

Figure 3.18 (Color online) H-P-T Phase Diagram of $BaCdVO(PO_4)_2$. The solid sqaures mark upper limit for the H_S for each pressure. The dotted lines are added to mark the approximate position of T_N at $H = 0$.

shift consists of two major contributions, the T-independent orbital part K_o and T-dependent spin part K_s:

$$K(T) = K_o + K_s(T) \tag{3.8}$$

The T-dependence of spin contribution of the isotropic part of the NMR shift $K_{iso,s}$ for the P1 site is shown in Fig. 3.19. With decreasing T, $K_{iso,s}$ increases and shows a broad peak at T_{max} = 2.6 K at H = 0.8 T.

A broad peak in the T dependence of NMR shift or susceptibility is a characteristic of the low dimensional spin system with an antiferromagnetic interaction J_{AF}. In a non-frustrated $S = 1/2$ antiferromagnetic square lattice system, the T_{max} is expected at $T_{max} = 0.95\ J_{AF}$ [151][152]. However, it should be noted that T_{max} in χ is reduced by the application of the magnetic field. In fact, as has been reported, T_{max} in χ decreases from 2.7 K at H = 0.1 T to 2.55 K at H = 1 T and to 2.08 K at 2 T [108]. $T_{max}(H)$ obtained from χ data, represented by

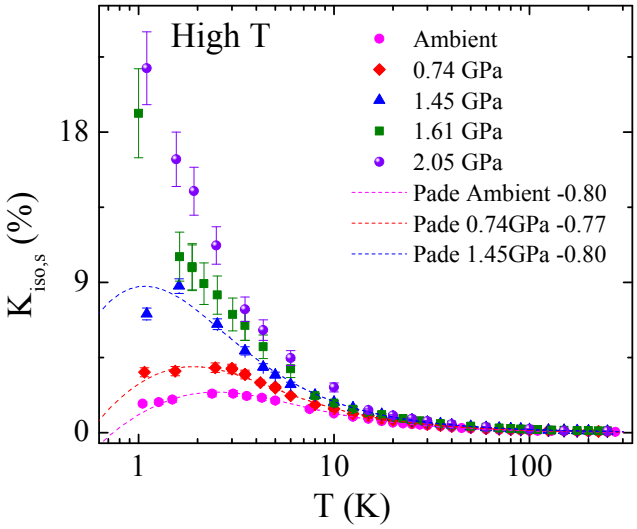

Figure 3.19 (Color online)T dependence of the NMR shift under different pressures. The experimental data for $p \leq$1.45 Pa are fitted with the normalized $\chi_{\text{theoretical}}$ to fit the high-T region of the data (shown by the dotted lines)

the black filled circles in Fig. 3.20a, is plotted as a function of H normalized by the saturation magnetic field $H_{\text{s}} = 4.2$ T under ambient pressure [108]. In the plot, $T_{\text{max}}(H)$ is normalized by $T_{\text{max}}(H = 0) = T_{\text{max}}(0) = 2.7$ K measured at the lowest magnetic field $H = 0.1$ T. The values for $T_{\text{max}}(0)$ were chosen to make the $T_{\text{max}}(H)/T_{\text{max}}(0)$ values, obtained from the $K_{\text{iso,s}}(T)$ data, fall on the smooth curve obtained from the χ data as shown in the Fig. 3.20a. $T_{\text{max}}(0)$ is seen to to be suppressed by p [Fig. 3.20b] indicating decrease of the AFM correlations with p.

The application of p not only leads to the suppression of T_{max}, but also enhances the magnitude of $K_{\text{iso,s}}$ dramatically at low-T [Fig. 3.19]. The NMR shift varies linearly with the spin susceptibility χ_{s} :

$$K_{\text{iso,s}}(T) = \frac{H_{\text{iso}}}{N_{\text{A}}\mu_B}\chi_{\text{s}}(T). \tag{3.9}$$

Thus, the increase of $K_{\text{iso,s}}$ with increasing p is due to an increase of hyperfine coupling field and/or an increase of χ_{s} with p. In order to see the p effects on χ_{s} we have calculated it using the High-Temperature Series Expansion (HTSE) method (eqn. 3.10) with appropriate change

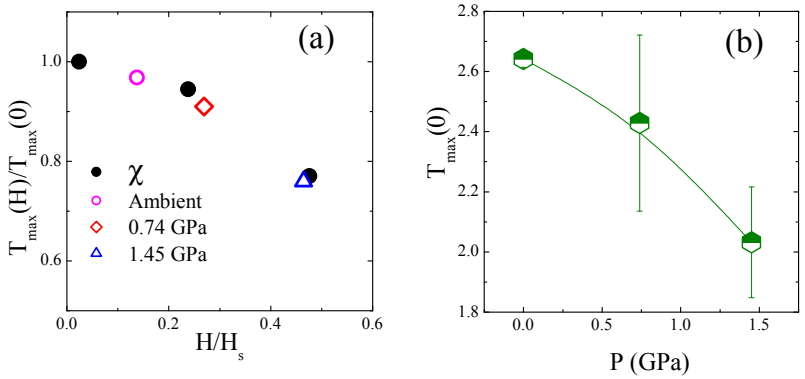

Figure 3.20 (Color online) (a) The solid circles indicate the $T_{\max}(H)/T_{\max}(0)$ values obtained from susceptibility data. The hollow symbols are the values obtained from the $K_{\mathrm{iso,s}}$ data. (b) p dependence of $T_{\max}(0)$.

of J_1 and J_2/J_1 values and found that they change by less than 5%. Thus, the increase of $K_{\mathrm{iso,s}}$ with increasing p is mainly due to the increase of hyperfine coupling field. By using the χ_{s} data under the ambient pressure we estimated H_{iso} (Fig. 3.21) under different pressures. The hyperfine field originates from the isotropic transferred hyperfine interaction (THI) due to the V spin moments. The P($3s$)-O($2p$)-V($3d$) covalent bond in the [$VOPO_4$] layers gives rise to the THI between V and P1. Thus the increase of the THI would be consistent since one expects that the application of high pressure will reduce the unit cell volume which in turn will lead to an increase of the strength of the covalent bond.

χ_{s} in the high temperature regime can be fitted by the High-Temperature Series Expansion (HTSE) proposed for the $S = 1/2$, J_1-J_2 Heisenberg model [153] using cluster expansion methods:

$$\chi_{\mathrm{s}}(T, J_1, J_2) = \frac{N_{\mathrm{A}} g^2 \mu_{\mathrm{B}}^2}{k_{\mathrm{B}} T} \sum_{n=0}^{9} \left(\frac{J_1}{k_{\mathrm{B}} T}\right)^n \sum_{m=0}^{n} c_{m,n} \left(\frac{J_2}{J_1}\right)^m \tag{3.10}$$

The HTSE of χ_{s} is a function of T, J_1 and J_2. With the inclusion of a proportionality factor, eqn. 3.10 should also fit $K_{\mathrm{iso,s}}$ data in high-T region due to eqn. 6.1. Thus, the increase of the $K_{\mathrm{iso,s}}$ with application of pressure might be attributed to the variation of the values of J_1 and

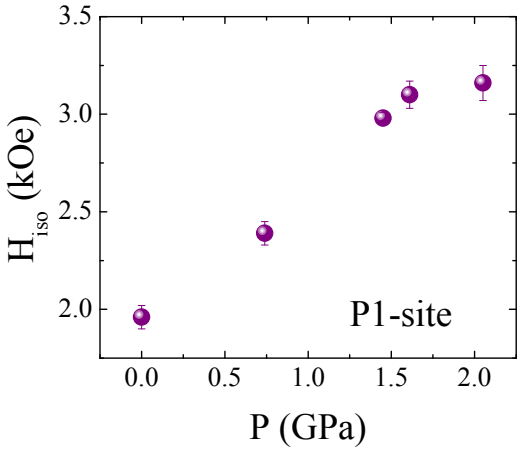

Figure 3.21 (Color online) The isotropic part of the hyperfine field $H_{\rm iso}$ vs pressure for P1 site

J_2 with pressure. To fit the experimental data we introduce reduced dimensionless variables:

$$t \equiv \frac{k_{\rm B}T}{|J_1|}, \qquad \tilde{\chi} \equiv \frac{\chi|J_1|}{N_{\rm A}g^2\mu_{\rm B}^2} \tag{3.11}$$

In the reduced units the eqn. 3.10 becomes:

$$\tilde{\chi}(t, J_1, J_2) = \frac{1}{t}\sum_{n=0}^{9}\left(\pm\frac{1}{t}\right)^n \sum_{m=0}^{n} c_{m,n}\left(\frac{J_2}{J_1}\right)^m \tag{3.12}$$

where the + sign is used for an antiferromagnetic $J_1 > 0$, and the - sign is used for a ferromagnetic $J_1 < 0$. We rearrange eqn. 3.12 such that in the limit of high-T, the left-hand side of eqn. 3.13 becomes equal to unity due to the Curie law $\chi = C/T$.

$$4\tilde{\chi}t = 4\sum_{n=0}^{9}\left(\pm\frac{1}{t}\right)^n \sum_{m=0}^{n} c_{m,n}\left(\frac{J_2}{J_1}\right)^m \tag{3.13}$$

We use Padé Approximants of the HTSE (eqn. 3.13) to fit the experimental data which allows us to do a more precise fitting in a broader range of temperature. We construct susceptibility for various J_1 and J_2/J_1 values in conjunction with the constraint of the saturation field, H_S for different pressures using the `PadeApproximant` utility in `Mathematica`. A Padé Approximant, Padé$[p, q](1/T) \equiv P(1/T)/Q(1/T)$, is a ratio of two polynomials P and Q of order p and q in $1/T$ respectively, such that $p + q \leq r$ where r is the order of the polynomial

whose Padé Approximant we are evaluating. As for the HTSE defined by eqn. 3.10, $r = 9$, thus we can use the following combinations of $[p, q]$: [5,4], [4,5], [4,4], [4,3], [3,4] and so on. For our final analysis we have used [4,4] due to a better agreement in fitting as compared to [4,5] or [5,4] both for the suceptibility data (Fig. 3.22a) and the NMR shift data (Fig. 3.22b). We

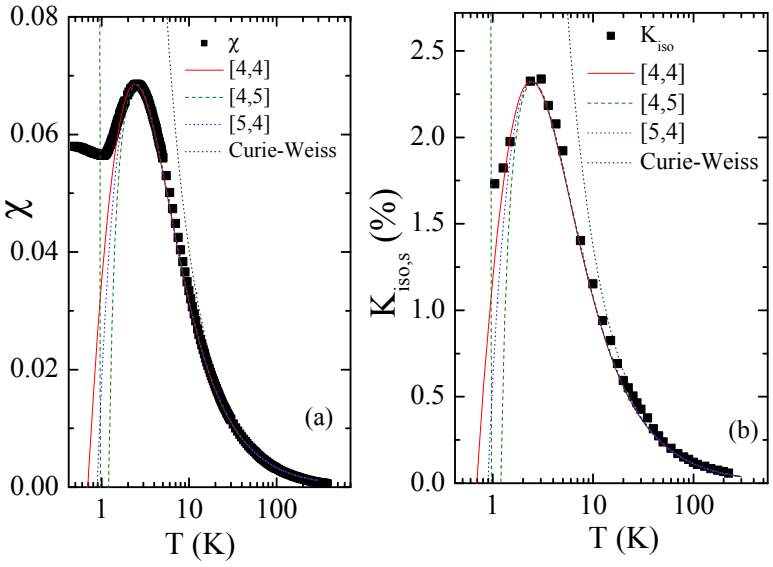

Figure 3.22 (Color online) Theoretical fitting with $\chi_{\text{theoretical}}$ using Padé Approximant with different $[p, q]$ combinations for (a) χ and for (b) $K_{\text{iso,s}}$ under ambient pressure. The labels "$[p, q]$" indicate $\chi_{\text{theoretical}}$ normalized with the peak position of $K_{\text{iso,s}}$

construct the theoretical susceptibility, $\chi_{\text{theoretical}}$, from the Padé Approximant of $4\tilde{\chi}t$ given by eqn. 3.13 for different combinations of J_1 and J_2 with the constraint of the saturation field H_{S}. Thus,

$$\chi_{\text{theoretical}} = \frac{N_{\text{A}} g^2 \mu_{\text{B}}^2}{4 k_{\text{B}} T} \chi_{\text{Pade}}(t, J_1, J_2); \tag{3.14}$$

where $\chi_{\text{Pade}} = 4\tilde{\chi}t$ defined in equation 3.13. Throughout this analysis we have assumed $g = 1.968$[108] and that it does not change with pressure.

From the linear-spin-wave theory for an infinite system H_S is given by[154]:

$$H_S = \frac{zSJ_c}{g\mu_B}\Bigg[\cos\phi\Bigg(1-\frac{1}{2}(\cos Q_x+\cos Q_y)\Bigg) + \sin\phi\Bigg(1-\cos Q_x\cos Q_y\Bigg)\Bigg], \tag{3.15}$$

where z is the number of nearest neighbors, $J_c = \sqrt{J_1^2+J_2^2}$ and $\phi = \tan^{-1}(J_2/J_1)$ and $\vec{Q}$ is the AFM ordering vector. For $BaCdVO(PO_4)_2$, $z = 4$, $S = 1/2$, $\vec{Q}$ is $[0, \pi]$. Thus, H_S simplifies to:

$$H_S = \frac{2}{g\mu_B}(J_1+2J_2) \tag{3.16}$$

The value of H_S obtained from this equation agrees very well with the experimentally obtained value without the introduction of the interplane coupling $J_\perp$ which is negligible ($\sim 10^{-4}$) for this class of compounds. Note that J_1 and J_2 have opposite signs and it is not possible to trivially comprehend the p dependence of J_1 and J_2 solely from the behavior of H_S with p.

Fig. 3.19 and Fig. 3.23 show the fitting of experimental data of $K_{iso,s}$ with the $\chi_{theoretical}$ normalized with it's value at the peak. The normalized $\chi_{theoretical}$ fits the experimental data ($K_{iso,s}$) very well, for various J_1 and J_2 values, from the room temperature down to 5 K for all the pressures up to 1.45 GPa. Under ambient pressure, the values of J_1, J_2 and J_2/J_1 obtained from this analysis agree with their previously obtained values[108] within the error bar. Since the $K_{iso,s}$ loses its identity below T_N all the analyses are done between $T_N \sim 1$ K and room temperature. Under pressures higher than 1.45 GPa, the $K_{iso,s}$ did not show any peak down to 1 K. Thus an unambiguous determination of the exchange coupling strengths was not possible for p >1.45 GPa from this analysis. We evaluated the values of J_1 and J_2 under different pressures by first reproducing the peak position of $K_{iso,s}$ with $\chi_{theoretical}$. Next we did a similar analysis but this time concentrating on fitting the experimental data in the high temperature region. Both fitting are shown in the figure 3.23. The values for the J_1, J_2 and J_2/J_1 under different pressures from the two different analyses are tabulated in Table 3.2.

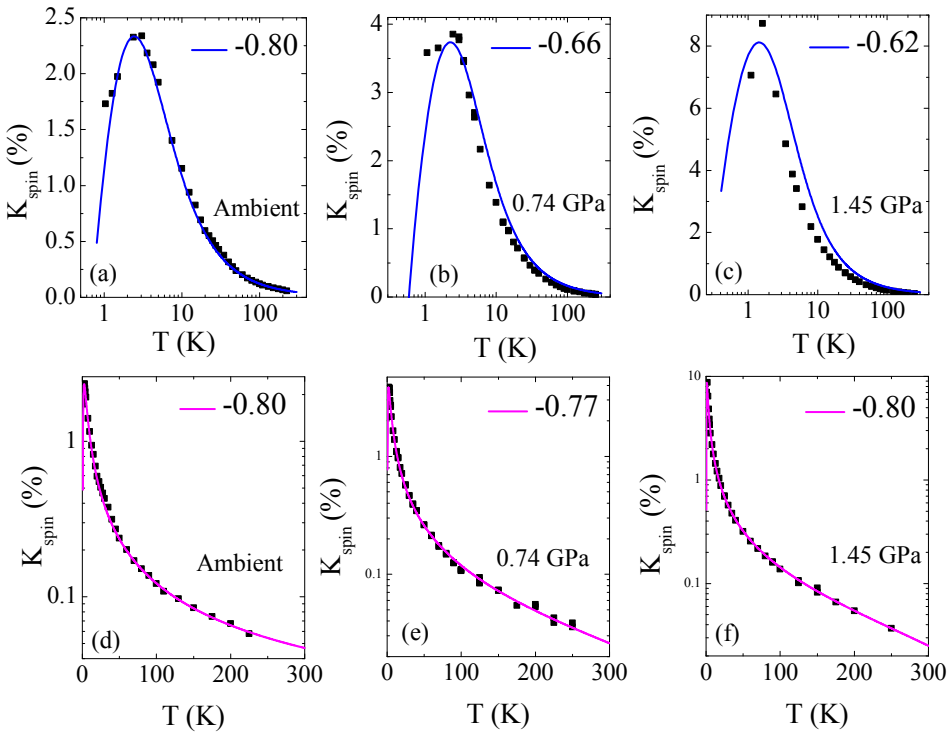

Figure 3.23 (Color online) Padé Fitting under different pressures from 'Peak' Analysis (a-c) and from 'High-Temperature' analysis (d-f).

Table 3.2 Estimation of values of J_1, J_2 and J_2/J_1 from the two analyses

Analysis	**Pressure (GPa)**	$\boldsymbol{J_1}$ **(K)**	$\boldsymbol{J_2}$ **(K)**	$\boldsymbol{J_2/J_1}$
Peak	0	-4.45 ± 0.45	3.55 ± 0.22	-0.8 ± 0.03
	0.74	-6.97 ± 2.61	4.44 ± 1.31	-0.66 ± 0.06
	1.45	-5.00 ± 1.25	3.06 ± 0.62	-0.62 ± 0.02
$High-T$	0	-4.45 ± 0.45	3.55 ± 0.22	-0.8 ± 0.03
	0.74	-3.85 ± 0.95	2.89 ± 0.48	-0.77 ± 0.06
	1.45	-1.93 ± 0.32	1.53 ± 0.16	-0.80 ± 0.05

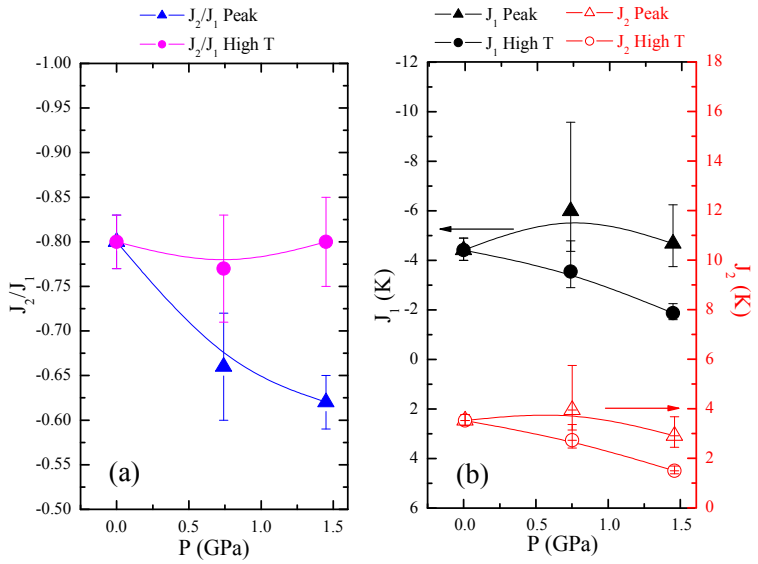

Figure 3.24 (Color online) p dependence of (a) the frustration ratio J_2/J_1 and (b) the exchange interactions J_1 and J_2 from two different analyses

Fig 3.24 shows how the J_1, J_2 and J_2/J_1 vary according to the two analyses done. From the peak position analysis, the ratio of J_2/J_1 seems to be decreasing with increase in pressure, and the magnitudes of J_1 and J_2 have a weak p dependence. $|J_2/J_1|$ is seen to decrease with pressure, from ~ 0.8 under ambient pressure to ~ 0.6 under $p = 1.45$ GPa. This indicates that with pressure the frustration ratio decreases and the system shifts more towards the questionable boundary between the CAF and the FM state in the $J_1 - J_2$ phase diagram. From the analysis

in the high-T, the ratio J_2/J_1 is almost constant for all pressures, and the magnitudes of both the exchange constants J_1 and J_2 decrease with pressure.

Thus, the two analyses gives us very different scenarios of the effects of pressure on this compound. Fig. 3.25 shows the $T_{\rm max}$ obtained from the $\chi_{\rm theoretical}$ as a function of $|J_2/J_1|$. This theoretical model does not work for $|J_2/J_1| < 0.6$. It shows that for both the analyses, *viz.* "Peak position" analysis as well as "High-T" analysis, the $T_{\rm max}$ decreases with p. But there is no clear way to figure out which analysis gives the correct trend of the behavior of $|J_2/J_1|$ with p only on the basis of the static study done. Thus, we look in to the dynamic study of the system to search for answers to clear this ambiguity.

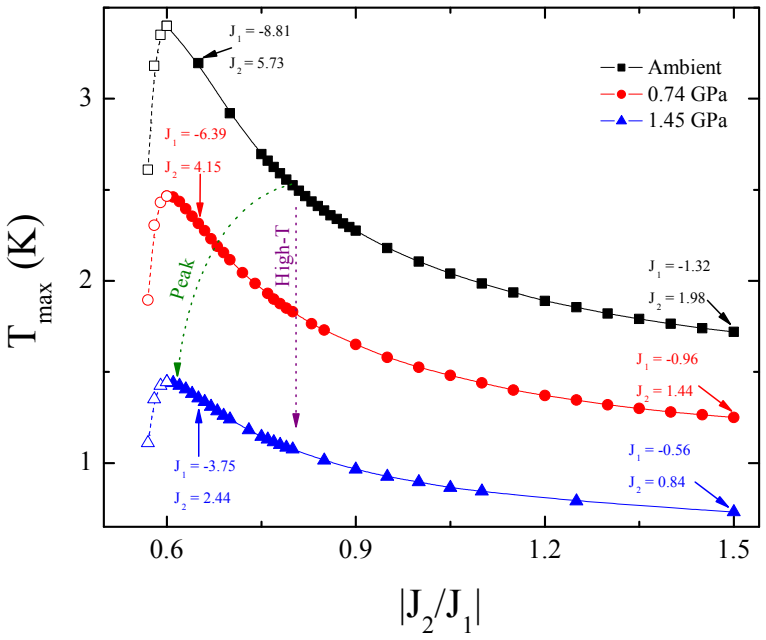

Figure 3.25 (Color online) $T_{\rm max}$ vs $|J_2/J_1|$.

Figures 3.26 (a-e) show the T and H dependence of the ^{31}P spin-lattice relaxation rate, $1/T_1$, measured at the peak position of the narrow line (P2 site) under different pressures. At high temperatures, $1/T_1$ is temperature-independent due to the exchange-narrowed hyperfine

interactions between the V spin moments in the paramagnetic state. On lowering the temperature close to T_N, $1/T_1$ increases and shows a divergent behavior due to critical slowing down of spin fluctuations. The columnar type antiferromagnetic spin fluctuations play an important role for driving the long range antiferromagnetic ordering in the system. The peak in the T dependence of $1/T_1$ is suppressed as the magnetic field approaches the saturation fields. But the CAF phase transition can still be clearly identified by the sudden decrease in $1/T_1$ just below T_N. Thus the H and p dependence of T_N (Fig. 3.29) is determined precisely from $1/T_1$ measurements under different fields for all the pressures. The T_N is also determined from the T-dependence of β, marked by sharp dips in $\beta - T$ plots (Fig. 3.26) under different H and different p.

Below T_N, $1/T_1$ in figure 3.26 decreases under all pressures but levels off below 0.3 K to 0.4 K under ambient pressure and under $p \geq 1.61$ GPa. The T-independent behavior of $1/T_1$ at low temperatures cannot be simply attributed to impurity spin effects because $1/T_1$ under 0.74 GPa and 1.45 GPa at the same magnetic field $H = 0.8$ T shows a different T dependence. The T-independent behavior below T_N is also observed in the temperature dependence of the muon relaxation rate λ in $BaCdVO(PO_4)_2$ [124]. The constant relaxation rates at low temperatures indicate temperature-independent spin fluctuations, which is a characteristic of a frustrated spin system with a degenerate ground state. For the intermediate pressures 0.74 GPa, 1.45 GPa and for high enough applied field ($H/H_s \approx 0.65$) under 1.61 GPa, $1/T_1$ is roughly proportional to $T^{2.7}$ below T_N as shown by solid lines in the figures 3.26 b-d. This T dependence is very similar to the T^3 dependence observed in $Pb_2VO(PO_4)_2$ [109]. The T^3 behavior below T_N is explained by the two-magnon Raman scattering process for nuclear relaxation in a 3-dimensional antiferromagnet [128].

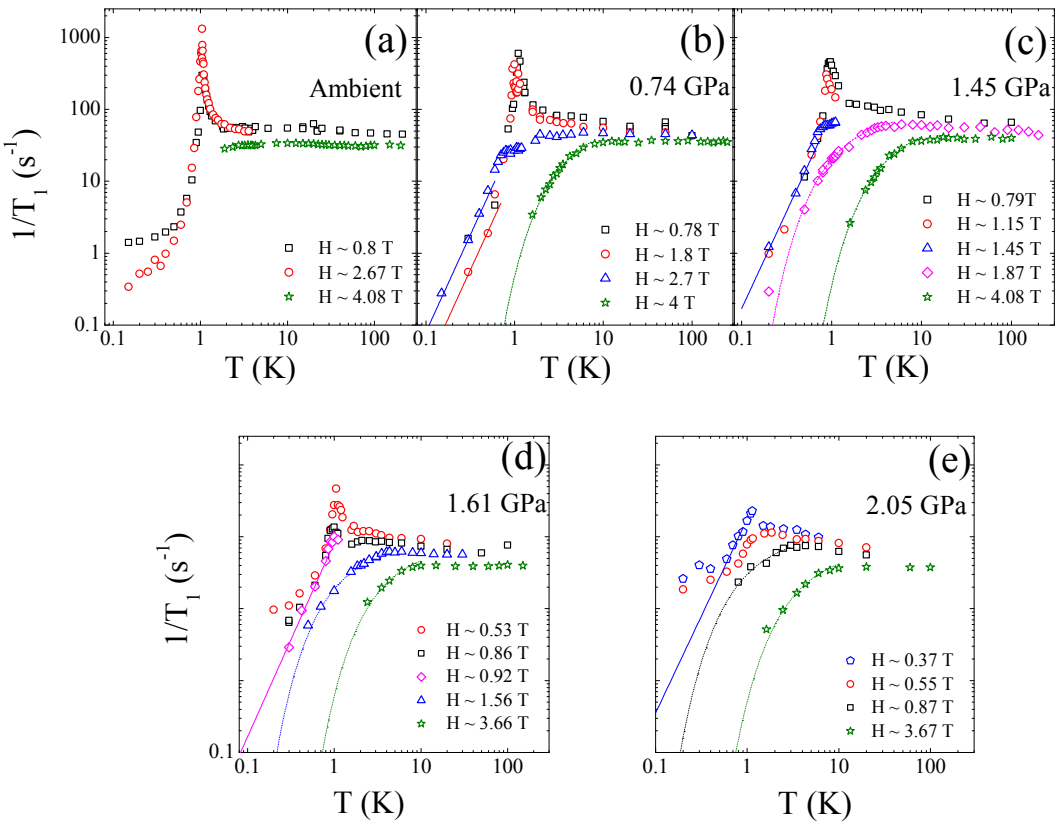

Figure 3.26 (Color online) T dependence of the ^{31}P spin-lattice relaxation rate at the P2 site at different applied magnetic fields and different pressures. While the solid lines indicate $T^{2.7}$ behavior of $1/T_1$, the dotted lines show the thermal activated behavior ($1/T_1 \approx \exp(-\Delta/k_B T)$)

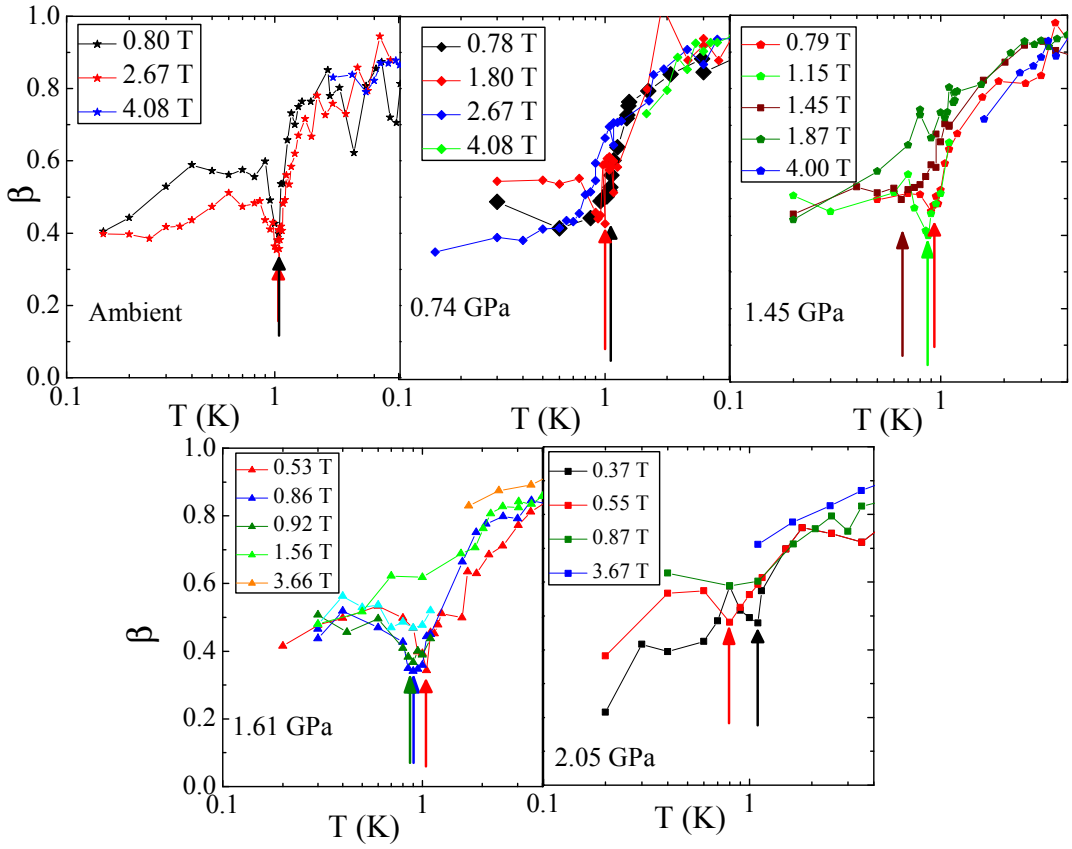

Figure 3.27 (Color online)T-dependence of β under different fields for $p = 0$ GPa, 0.74 GPa, 1.45 GPa, 1.61 GPa and 2.05 GPa. The T_{N} is marked with an arrow shown in the figure.

Table 3.3 Estimation of Δ from T_1 data and its comparison with $g\mu_B H$

Pressure (GPa)	H_s(T)	*Applied Field* H (T)	$g\mu_B H/k_B$ (K)	Δ/k_B (K) from T_1 *data*
0.74	2.9	4.00	5.29	5.00
1.45	1.7	1.87	2.47	1.50
		4.08	5.39	5.30
1.61	1.4	1.56	2.06	1.45
		3.66	4.84	4.81
1.88	0.7	0.87	1.15	1.25
		3.67	4.85	4.82
2.05	0.7	0.87	1.15	1.30
		3.67	4.85	4.89

Above saturation magnetic field, $1/T_1$ does not show a clear peak or sudden decrease but rather decreases gradually at low temperatures due to a crossover from the paramagnetic state to a fully polarized spin state. In the polarized state, $1/T_1$ is found to follow a thermal activated behavior $1/T_1 \approx \exp(-\Delta/k_B T)$ as shown by broken lines in the figures 3.26 b-e. The magnitude of Δ/k_B under different pressures and fields are listed in Table 3.3. $1/T_1$ originates from thermal fluctuations of spin moments which corresponds to the deviation of spin moments from fully polarized state. In this case, $1/T_1$ is known to be proportional to the derivative of the Brillouin function $\frac{dB_J(x)}{dx}$ [119] and follows a thermally activated behavior $1/T_1 \approx \exp(-g\mu_B B_J(x)/k_B T)$ [119]. The values for Δ are in a good agreement with the corresponding values for the Zeeman energy $g\mu_B H$ except for the cases of $p = 1.45$ GPa; $H = 1.87$ T, and $p = 1.61$ GPa; $H = 1.56$ T , i.e. in the vicinity of the corresponding saturation fields for the two intermediate pressures.

The analysis of J_1 and J_2 from the isotropic NMR shift is not conclusive since the two different methods give dissimilar p-dependence of the exchange couplings. In order to resolve that we try to estimate the p-dependence of the exchange couplings from $1/T_1$ measured at the P2 site. Following a similar approach given in [109], in the high-temperature limit (thermal energy > exchange energy), the nuclear spin-lattice relaxation rate according to Moriya [126] is given by,

$$\left(\frac{1}{T_1}\right)_{T\to\infty} = \frac{(\gamma_N g\mu_B)^2\sqrt{2\pi}z'S(S+1)}{3\omega_E}\left[\frac{\left(\frac{A^a_{hf}}{z'}\right)^2+\left(\frac{A^c_{hf}}{z'}\right)^2}{2}\right] \tag{3.17}$$

where $\omega_E = [\max(|J_1|,|J_2|)k_B/\hbar]\sqrt{2zS(S+1)/3}$ is the Heisenberg exchange frequency, z is the number of NN spins of V^{4+} ion, z' is the number of nearest-neighbor V^{4+} spins of the P2 site. We measured $1/T_1$ at the position which corresponds to $\theta = 90°$ (θ is the angle between the quantization axis (c -axis) and the direction of the applied field) in the powdered pattern spectrum for the P2 site. Thus, the hyperfine couplings in the ac (or the bc) plane, i.e. A^a_{hf} and A^c_{hf} are used in the above equation. For the P2 site in $BaCdVO(PO_4)_2$ system, the values used are $z' = 1$, S =1/2, $z = 4$. Using the values for A^a_{hf}, A^c_{hf} and $1/T_1$ (Table 3.4) under the different pressures the p-dependence of the exchange coupling $J \sim \max(|J_1|,|J_2|)$ were estimated. Fig. 3.28 shows that the exchange coupling is nearly independent of pressure.

Table 3.4 $J_{calculated}$

Pressure (GPa)	A^a_{hf} Oe/μ_B	A^c_{hf} Oe/μ_B	$1/T_1$ sec^{-1}	$J_{calculated}$ (K)
0	-264.0	378.0	31.7	5.3
0.74	-217.6	428.1	36.9	4.0
1.45	-285.6	399.3	39.9	5.1
1.61	-173.7	467.1	40.6	3.8
1.88	-200.4	325.4	37.9	5.6
2.05	-233.9	390.7	37.6	5.1

From this analysis it is evident that either or both of the exchange couplings J_1 or J_2 must be having a weak p dependence. Looking back at the analyses done from the NMR shift, the "Peak" position analysis seems to be more favorable. According to that analysis J_1 and J_2 are vary weakly with pressure and the frustration ratio $|J_2/J_1|$ decreases from ~ 0.8 under ambient pressure to ~ 0.6 under $p \sim 1.45$ GPa. T_N is identified with the temperature at which the system goes into the long-range ordered state, thus the explanation of the p-independent behavior of T_N (Fig. 3.29) requires the additional knowledge of strength of the exchange coupling between the magnetic layers $J_\perp$. Although $J_\perp$ is negligible, application of pressure might result in the

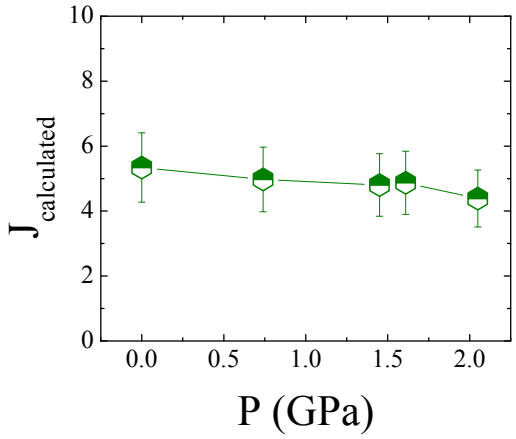

Figure 3.28 (Color online) p-dependence of the exchange coupling calculated from the high--temperature $1/T_1$

change of $J_\perp$ resulting in the observed behavior of $T_{\rm N}$. The reduction of $T_{\rm max}$ with pressure can be attributed to the suppression of the $|J_2/J_1|$ and a reduction of energy scale at which the short-range correlations start to emerge, which is indicative of the system moving towards a less ordered state or a state with less AFM character. Indeed the reduction of the ratio $|J_2/J_1|$ (Fig. 3.29) does lead to the questionable boundary between the CAF and the FM states. The extrapolation of $H_{\rm S}$ shows that at $p \approx 2.35$ GPa, the saturation field must completely vanish resulting in the absence of the CAF region in the phase diagram which indicates that the ground state will be a new phase. The question as to whether this new phase is an FM phase or some disordered phase requires further experiments under $p > 2.35$ GPa.

We are curious to study magnetic properties of $BaCdVO(PO_4)_2$ around 2.35 GPa at low temperatures to investigate the existence of the gapless nematic state. However, our clamp-type pressure cell modified for the dilution refrigerator would have a maximum limit of the pressure ≈ 2 GPa at low temperatures and would not reach 2.35 GPa. Higher pressure studies at low temperatures are highly required to confirm our proposal.

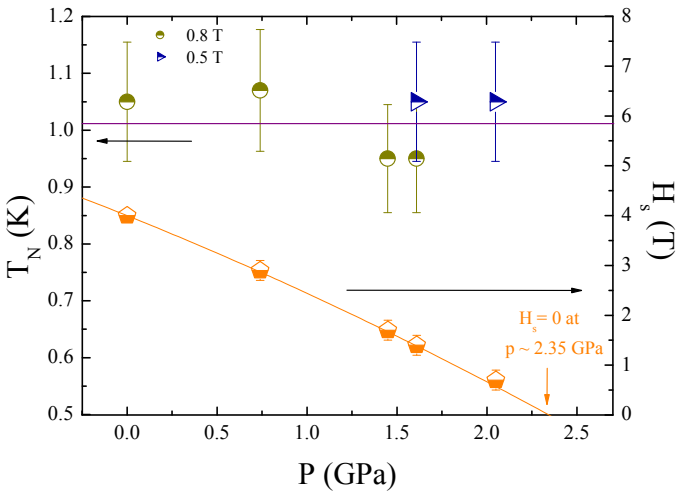

Figure 3.29 (Color online) Effect of pressure on the magnetic transition temperature $T_{\rm N}$ and the magnetization saturation field $H_{\rm s}$. From the plot $H_{\rm s} = 0$ at $p \approx 2.35$ GPa

3.2.5 Conclusion

We have conducted ^{31}P-NMR measurements under high pressures and low temperatures on $BaCdVO(PO_4)_2$. The frustration in this compound is much higher than in $Zn_2VO(PO_4)_2$ due to the comparable in-plane exchange couplings with opposite signs ($J_2/J_1 \simeq -0.88$). The in-plane anisotropy being negligible, this compound can be considered very close to an ideal J_1-J_2 model. AFM short-range correlations start emerging above 1 K as seen from the broad peak of $K_{\rm iso}$ and increase of $1/T_1T\chi$ above $T_{\rm N}$. The transition to a magnetically long-range-ordered (LRO) state at $\simeq$ 1 K is driven by the very small but finite intra-plane exchange coupling $J_\perp$. The in-plane exchange couplings are $\sim$ 3 K. The suppression of $T_{\rm N}$ originates from the effects of frustration. This compound lies in the vicinity of the very interesting but unidentified phase between Columnar AFM (CAF) phase and FM phase. Thus, we applied pressure on this compound to study its effects on J_1 and J_2. The first experimentally evidenced H-P-T phase diagram for FSL vandates has been established through this work (Fig 3.18). Under ambient pressure, $T_{\rm N}$ increases slightly with H from 0 to $\approx$ 2 T and then decreases with further increase

in the field. The slight increase of T_N at low magnetic field is considered to be due to the suppression of quantum fluctuations by the applied magnetic field. Then, once the magnetic field is strong enough to suppress the antiferromagnetic ordering, T_N is reduced and finally suppressed completely. With further increase in the field, the system is in a fully polarized spin state where all the spins orient themselves along the applied magnetic field. The ground state does not change from the CAF state with application of pressure up to 2.05 GPa, but the saturation field decreases strongly. The extrapolation of the saturation field (Fig 3.29) shows that H_S should completely vanish at $p \approx 2.35$ GPa. Pressure does not have any significant effect on T_N. The NMR shift and the nuclear spin-lattice relaxation measurements lead us to the conclusion that while J_1 and J_2 vary slightly with pressure and the frustration ratio ($|J_2/J_1|$) decreases to 0.62 under a pressure of 1.45 GPa. Study of this material under $p > 2.35$ GPa might yield answer to whether the system goes to the FM state via a first-order phase transtion or reaches a phase with a very novel ground state. Our experimental limitations allowed us to do measurements only up to 2.05 GPa in low temperatures. But it is clear that the results obtained have paved way for the experimental realization of the ground state of the very mysterious phase boundary in the $J_1 - J_2$ model.

CHAPTER 4. ITINERANT QUASI-2D SYSTEMS

4.1 $CaFe_2As_2$

This chapter is based on work published in [155] and [156].

4.1.1 Introduction

$CaFe_2As_2$ is a member of the family of high-T_c iron pnictides with the common formula AFe_2As_2 (known as "122" systems) and with a structure (Fig. 4.1) similar to that of $ThCr_2Si_2$ at room temperature [157]. It exhibits a collinear 'stripe'-type anitferromagnetic (AFM) ground state below $T_N = 170$ K, typical for the parent compound of this "122" series of superconductors ($T_N = 139(3)$ K for $BaFe_2As_2$[158], $T_N = 212(8)$ K for $SrFe_2As_2$[159], $T_N \approx 190$ K for $EuFe_2As_2$[160]). A simultaneous structural transition from a high-temperature (HT) tetragonal ($\mathcal{T}$) phase to a low-temperature (LT) orthorhombic ($\mathcal{O}$) phase occurs at 170 K along with the magnetic one[161][162][163].

Doping with Co or Ni induces superconductivity in $CaFe_2As_2$ with T_c up to 15 K [163] [164] [165] [166]. Application of pressure changes the LT AFM $\mathcal{O}$ phase to a non-magnetic collapsed-$\mathcal{T}$ (c-$\mathcal{T}$) phase. [163][167][168][169]. The c-$\mathcal{T}$ phase in $CaFe_2As_2$ is a non-magnetic phase with a reduction in the tetragonal c-axis by 10% from the value at HT [170][171][156]. Apart from doping and pressure application, different heat treatment conditions yield different magnetic or non-magnetic states in $CaFe_2As_2$[166][156]. Preparation of sample with various heat treatments controls the strains inside a crystal grown out of excess FeAs due to formation of nanoscale precitipates. While $CaFe_2As_2$ annealed at 400 °C for 24 hours undergoes a phase transition from the HT-$\mathcal{T}$ paramagnetic (PM) state to the LT-$\mathcal{O}$ AFM state at $T_N \approx 170$ K (similar to the case where crystals are grown with Sn flux), $CaFe_2As_2$ grown out of excess FeAs,

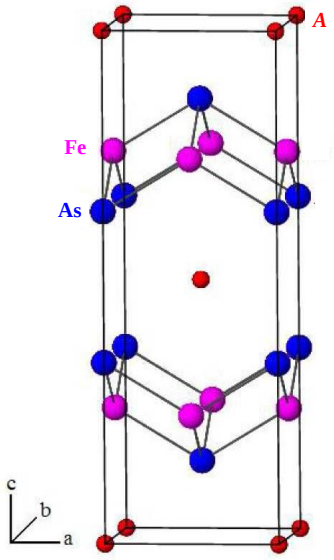

Figure 4.1 (Color online) Structure of AFe$_2$As$_2$ from [157] and [172]

quenched from 960 °C to room temperature, exhibits a transition to the cT nonmagnetic phase below $T_s \approx 95$ K.

Recently, absence of magnetic fluctuations in the nonsuperconducting c$\mathcal{T}$ phase was evidenced by the inelastic neutron scattering (INS)[173] and angle-resolved photoemission spectroscopy (ARPES) [174] study. This indicates that spin fluctuations are a necessary ingredient for unconventional SC in the iron pnictides. Nevertheless, INS measurements, probing mainly high-energy spin dynamics (order of Kelvin), could not exclude the presence of magnetic fluctuations completely in very low-energy regions such as a milli-Kelvin order which led us to utilize the technique of nuclear magnetic resonance (NMR) and nulcear quadrupole resonance (NQR) to detect low-energy spin dynamics in CaFe$_2$As$_2$ prepared with different heat treatments.

Prior ^{75}As-NQR studies showed a T-independent behavior of $1/T_1T$ [175][176] in the c-$\mathcal{T}$ phase in CaFe$_2$As$_2$ under a pressure of 10.8 kbar, indicating the absence of the superconducting state in the c-$\mathcal{T}$ phase. Ma et al. [177] have carried out ^{75}As-NMR in Pr-doped CaFe$_2$As$_2$ and found a large increase in a nuclear quadrupole frequency ν_Q in the LT c-$\mathcal{T}$ phase, similar to the case of ^{75}As-NMR in the quenched CaFe$_2$As$_2$ [156]. They have also reported the T dependence of $1/T_1$ in the c-$\mathcal{T}$ phase showing a broad peak at ∼25 K, which is attributed to originate from

Pr^{3+} spin dynamics, and not due to the spin correlations of Fe spins. Given these results, a detailed study of static and dynamic spin correlations in the c-$\mathcal{T}$ phase of $CaFe_2As_2$ measured under ambient pressure is intriguing and important, and also would provide some clues about the origin of superconductivity (SC) in the c-$\mathcal{T}$ phase of $(Ca_{1-x}Sr_x)Fe_2As_2$ with $T_c \sim 22$ K in [178] and $(Ca_{1-x}R_x)Fe_2As_2$ ($R \equiv$ Pr, Nd) with $T_c > 45$ K in [179], as well as for the observation of SC in other carrier-doped $CaFe_2As_2$ [180][181][182].

Using conventional high-temperature growth techniques[183][184], single crystals of $CaFe_2As_2$ were grown out of FeAs flux [166][156] which were used in this NMR study. We compare crystals grown by using two different heat treatments. The "as-grown" sample where the crystals were prepared by quenching from 960°C to room temperature, and "annealed" sample where the crystals were annealed at 400°C for 24 hours and then quenched to room temperature [166][156].

In the next section, we discuss about ^{75}As-NMR ad NQR measurements done on both "as-grown" and "annealed" crystals of $CaFe_2As_2$ to compare their electronic and magnetic properties due to different heat treatments and also to investigate the characteristics of c-$\mathcal{T}$ phase in $CaFe_2As_2$. From the NMR and NQR study it is seen that while the "annealed" $CaFe_2As_2$ undergoes a phase transition from the *HT* $\mathcal{T}$ paramagnetic state to a *LT* $\mathcal{O}$ AFM state at $T_N \sim 170$ K, the "as-grown" crystal shows a *HT* $\mathcal{T}$ - *LT* c-$\mathcal{T}$ phase transition at $T_s \sim 96$ K. From the T dependence of $1/T_1$, stripe-type AFM spin correlations are realized in the *HT* $\mathcal{T}$ phase. On the other hand, no trace of the AFM spin correlations can be found in the nonsuperconducting *LT* c-$\mathcal{T}$ phase, demonstrating a quenching of Fe moments in the *LT* c-$\mathcal{T}$ phase from a microscopic viewpoint. These results are consistent with the recently reported INS [173] and ARPES [174] results.

4.1.2 Experimental Details

Single crystals of $CaFe_2As_2$ were prepared under different heat condicitons. The sample referred to as "as-grown" is a single crystal of $CaFe_2As_2$, prepared by quenching from 960°C to room temperature. Another single crystal of $CaFe_2As_2$ was prepared by annealing at 400°C for 24 hours and then quenching it to room temperature, which is reffered to as "annealed" sample.

Details of the growth, annealing, and quenching procedures are reported in Refs.[166][156].

NMR and NQR measurements were carried out on ^{75}As ($I = 3/2$, $\gamma/2\pi = 7.2919$ MHz/T, $Q = 0.29$ Barns) by using a homemade, phase-coherent, spin-echo pulse spectrometer. The ^{75}As-NMR spectra were obtained by sweeping the magnetic field H at a fixed frequency $\nu = 51$ MHz, while the ^{75}As-NQR spectrum in zero field was measured in steps of frequency by measuring the intensity of the Hahn spin echo. The magnetic field was applied parallel to either the crystal c-axis or the ab-plane. The ^{75}As-$1/T_1$ was measured with a saturation recovery method. The $1/T_1$ at each T was determined by fitting the nuclear magnetization M versus time t using the exponential functions 1-$M(t)/M(\infty) = 0.1\ e^{-t/T_1} + 0.9\ e^{-6t/T_1}$ for ^{75}As-NMR, and 1-$M(t)/M(\infty) = e^{3t/T_1}$ for ^{75}As-NQR, where $M(t)$ and $M(\infty)$ are the nuclear magnetization at time t after the saturation and the equilibrium nuclear magnetization at $t \to \infty$, respectively.

4.1.3 NMR Study

Fig. 4.2a and 4.2b show field-swept ^{75}As-NMR spectra for the "annealed" and the "as-grown" $CaFe_2As_2$ samples respectively at 51 MHz for the field applied along the c-axis ($H \parallel c$) and along the ab-plane ($H \parallel ab$). In the HT $\mathcal{T}$ phase we witness a spectrum split into three lines (sharp central line and two satellites) by quadrupole interaction typical for a nucleus with $I = 3/2$ in a non-cubic environment. The observed quadrupole-split NMR spectra can be reproduced (shown by the blue lines in the Fig. 4.2 and the red lines in Fig. 4.3) by the spin Hamiltonian with the Zeeman term and the quadrupolar term:

$$\mathcal{H} = \gamma_N \hbar \vec{I} \cdot \vec{H}_{\text{eff}} + \frac{h\nu_Q}{6}[3I_z^2 - I(I+1)] \tag{4.1}$$

where $\vec{H}_{\text{eff}}$ is effective field at the As-site (external field + hyperfine field $\vec{H}_{\text{hf}}$), h is the Planck's constant, and $\nu_Q = eQV_{zz}/2h$ is the nuclear quadrupole frequency with Q being the quadrupole moment of the As nucleus, V_{zz} is the EFG at the As site (discussed in detail in chapter 1). Although the "as-grown" $CaFe_2As_2$ sample shows a similar quadrupole-split NMR spectra (Fig. 4.2b) at $T > 96$ K, the observed $\nu_Q \sim 18$ -18.5 MHz at $T = 140$ - 110 K is larger than that in the "annealed" crystal ($\nu_Q \sim 13.7$ MHz at 200 K).

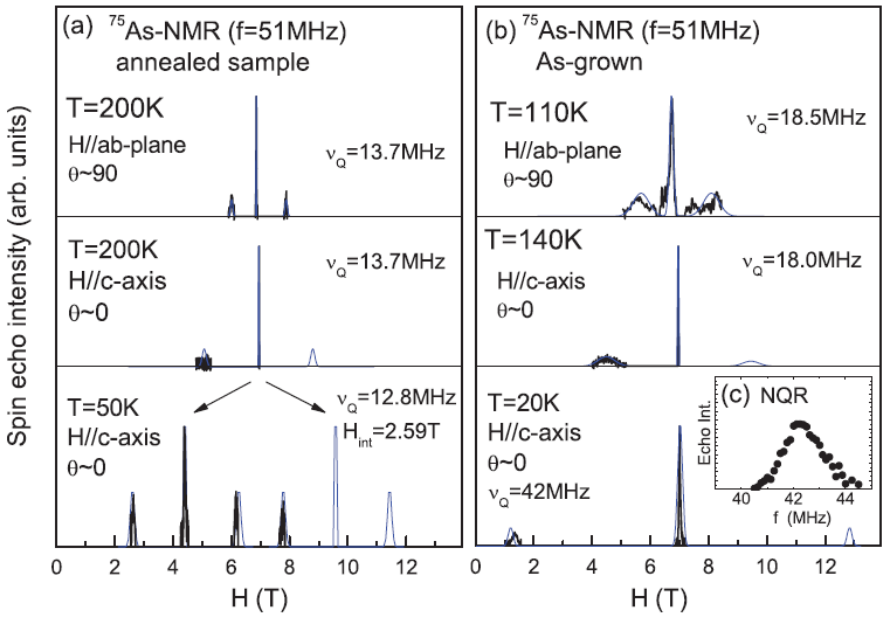

Figure 4.2 (Color online) ^{75}As-NMR spectra measured at $\nu = 51$ MHz for (a) 400°C "annealed" $CaFe_2As_2$ crystal and (b) for the "as-grown" $CaFe_2As_2$ crystal. Black and blue lines are observed and simulated spectra, respectively. Expected lines above 9 T are not measured due to the limited maximum magnetic field for our SC magnet. (c) ^{75}As-NQR spectrum at $T = 4.2$ K and $H = 0$ T.

The satellite linewidth, which reflects the distribution of electric field gradient (EFG) due to defects or lattice distortion, is significantly larger in the case of "as-grown" sample than in the "annealed" sample. To reproduce the linewidth, one needs to introduce $\sim$ 15% distribution ($\Delta\nu_Q = 2.7$ MHz) in "as-grown" sample at $T = 110$ K as shown by the red curves in the figure 4.3a, much larger than the $\sim$4% distribution of $\Delta\nu_Q = 13.7$ MHz at $T = 200$ K for the case of ^{75}As-NMR in the "annealed" $CaFe_2As_2$ crystal shown at the top panel in Fig. 4.3a. This indicates a higher degree of inhomogeneity of the local As environment in the "as-grown" $CaFe_2As_2$ than in the "annealed" $CaFe_2As_2$, which supports the idea that the higher-temperature quenching introduces strains inside the crystal.

Below 160 K, each NMR line for $H \parallel c$ axis in the case of "annealed" crystals splits into two lines due to internal field $H_{\rm int}$ (parallel or antiparallel to H) which is produced by the Fe

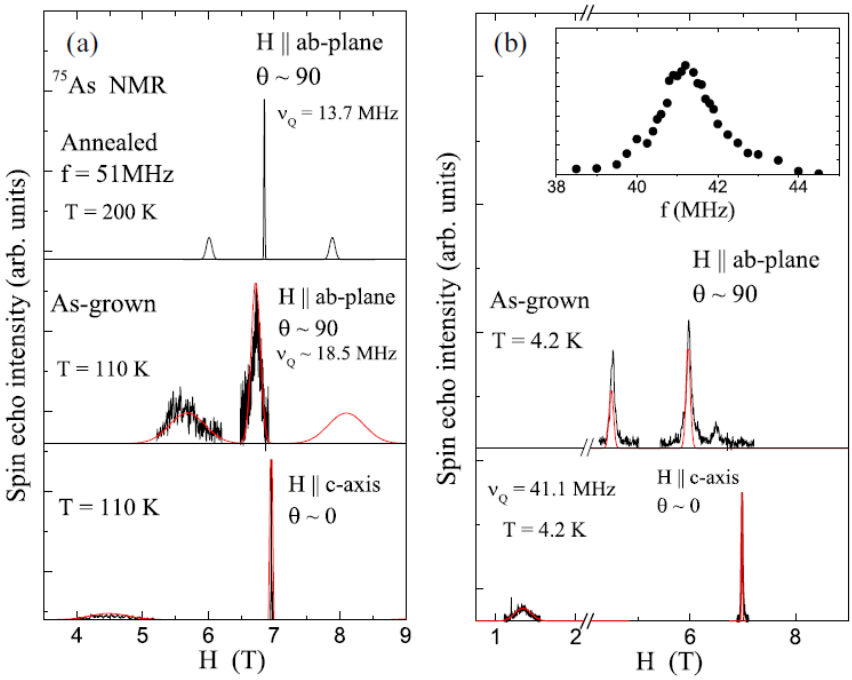

Figure 4.3 (Color online) (a) Field-swept ^{75}As-NMR spectra for the "as-grown" cc crystal at $\nu = 51$ MHz in the high-temperature tetragonal phase (measured at T = 110 K) for magnetic field parallel to the c-axis (bottom) and perpendicular to the c-axis (middle), together with ^{75}As-NMR spectrum at $T = 200$ K for the "annealed" $CaFe_2As_2$ crystal with H perpendicular to the c-axis (top). The black and red lines are observed and simulated spectra, respectively. Expected lines above 8.5 T are not measured due to the limited maximum magnetic field for our SC magnet. (b) Same as described in (a) but in the low-temperature collapsed tetragonal phase (measured at $T = 4.2$ K). (Inset) ^{75}As-NQR spectrum at $T = 4.2$ K and $H = 0$ T.

spin-ordered moment. A typical example of the split NMR lines for $H \parallel c$ axis is shown at the bottom of Fig 4.2a. The spectrum is reproduced well by $H_{\rm int} = 2.59$ T and $\nu_{\rm Q} = 12.8$ MHz at $T = 50$ K. These values are in good agreement with previously reported values for ^{75}As-NMR of single crystals ($T_{\rm N} = 167$ K) grown from Sn flux,[185] once again indicating that the sample annealed at 400°C is essentially the same as previously reported ones grown from Sn.

In the case of "as-grown" sample, no splitting of the NMR lines is observed below the transition temperature, $T_{\rm s} \sim 96$ K, (indicating that there is no antiferromagnetic order). The full width of half maximum of the central line at $T = 4.2$ K is 290 Oe and 895 Oe for $H \parallel c$-axis and $H \parallel ab$-plane, respectively, and we do not see any magnetic broadening in the NMR spectra

even at the lowest temperature (1.5 K) measured. But below 96 K, the spectra for both H directions change drastically [see Fig. 4.3b] due to a dramatic change in $\nu_{\rm Q}$ from $\sim$ 18.5 MHz in the HT $\mathcal{T}$ phase to 41.1 MHz at T = 4.2 K in the LT c$-\mathcal{T}$ phase. Such a drastic change of $\nu_{\rm Q}$ (more than 230%) cannot be explained by thermal expansion of lattice (which can cause an increase of just a few %) but is attributed to a structural phase transition. A $\nu_{\rm Q}$ of 41.1 MHz is also confirmed by the observation of nuclear quadrupole resonance (NQR) spectrum at zero magnetic field at T = 4.2 K [Fig. 4.2 and inset of 4.3b]. This value of $\nu_{\rm Q}$ is comparable to 35.8 MHz and 41.5 MHz in the LT c$-\mathcal{T}$ phase in $(Ca_{1-x}Pr_x)Fe_2As_2$ for x = 0.075 and 0.15, respectively [177], but is higher than those reported for $\mathcal{T}$ phase (25 MHz) and c$-\mathcal{T}$ phase (30.4 MHz) of $CaFe_2As_2$ under ambient pressure and high pressure respectively as per previous reports [175]. Structural phase transition without any magnetic transition has been established as the cause for this large change in $\nu_{\rm Q}$[177].

The distribution of the $\nu_{\rm Q}$ in the LT c$-\mathcal{T}$ phase is estimated to be $\Delta\nu_{\rm Q} \sim$ 2 MHz, which is smaller than $\Delta\nu_{\rm Q} \sim$ 2.7 MHz in the HT $\mathcal{T}$ phase which indicates that there is less inhomogenity in the local As environment in the LT c$-\mathcal{T}$ phase in the "as-grown" sample as compared to it's HT $\mathcal{T}$ phase. Below $T_{\rm s}$ (in the LT c$-\mathcal{T}$ phase) $\nu_{\rm Q}$ is nearly independent of T which differs from the scenario in the HT $\mathcal{T}$ phase where $\nu_{\rm Q}$ decreases from $\sim$18.5 MHz at T = 110 K to $\sim$18.0 MHz at T = 140 K (Fig. 4.2b), as well as the case in the HT $\mathcal{T}$ phase of the Sn-flux $CaFe_2As_2$ where $\nu_{\rm Q}$ decreases from $\sim$14 MHz at 170 K to $\sim$12 MHz at 270K [185]. Since $V_{\rm ZZ}$ arises from hybridization between the As-4p and Fe-3d orbitals with an additional contribution from the noncubic part of the spatial distribution of surrounding ions, the larger $\nu_{\rm Q}$ in the c$-\mathcal{T}$ phase indicates a strong hybridization between the orbitals. The difference of $\nu_{\rm Q}$ in magnitude and in its T dependence can be qualitatively interpreted when one takes into consideration the difference in magnitude and T dependence of c-axis lattice constant in the corresponding phases: a nearly T-independent behavior ($\sim$ 10.65 Å) below $T_{\rm s}$ and a monotonic increase from 11.2 Å at T = 100 K to 11.58 Å at 300 K in the $\mathcal{T}$ phase [156].

Figure 4.4a shows the T dependence of Knight shift for the "as-grown" $CaFe_2As_2$ sample, $K_{\rm ab}$ and $K_{\rm c}$ for H parallel to the ab plane and to the c axis, respectively, where the second-order quadrupole shift was corrected for in $K_{\rm ab}$. With decreasing T, $K_{\rm c}$ decreases slightly

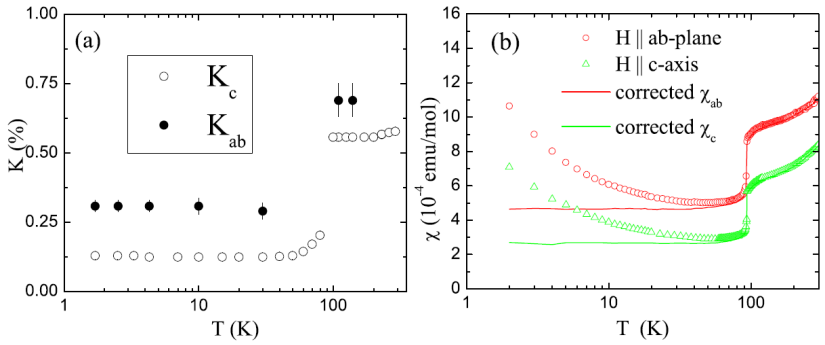

Figure 4.4 (Color online) (a) Temperature T dependence of ^{75}As NMR shifts K_{ab} and K_c for the "as-grown" $CaFe_2As_2$. (b) Anisotropic magnetic susceptibility $\chi \equiv M/H$ vs T (where M is magnetization and H is applied magnetic field) for the "as-grown" $CaFe_2As_2$ crystal measured at $H = 1$ T. From the NMR Knight shift measurements shown in (a), the upturns in $\chi(T)$ below ∼50 K are not intrinsic, originating from impurities. The solid lines are corrected $\chi(T)$ by subtracting the impurity contributions

down to ∼100 K, and shows a sudden decrease at T_s similar to the $\chi(T)$ behavior shown in Fig. 4.4b, and then levels off at low temperatures without showing upturns. It is noted that $K_c \sim 0.55\%$ in the HT $\mathcal{T}$ phase is greater than $K_c = 0.15\%$-0.3% for the "annealed" $CaFe_2As_2$ (not shown here) and Sn-flux $CaFe_2As_2$ [185], but close to $K_c = 0.58\%$ in Pr-doped $CaFe_2As_2$ [177]. K_{ab} also shows the similar T-independent behavior in the LT c$-\mathcal{T}$ phase: the data are limited above T_s due to very poor signal intensity. The upturns in $\chi(T)$ observed at low T in Fig. 4.4b are therefore not intrinsic and evidently arise from a small amount of a paramagnetic impurity. The solid lines in Fig. 4.4b are corrected $\chi(T)$ obtained by subtracting the impurity contributions, where the T-independent χ indicates a Pauli paramagnetic state, including diamagnetic conduction electron Landau and coreelectrons susceptibilities, for the LT c$-\mathcal{T}$ phase.

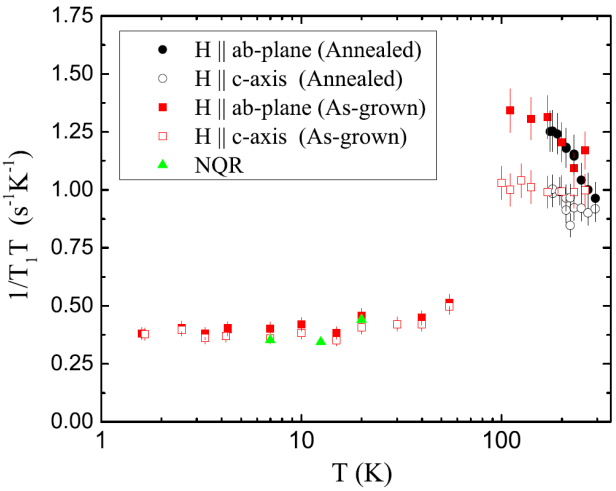

Figure 4.5 (Color online) Temperature dependence of $1/T_1T$ for both magnetic field directions, $H \parallel ab$ plane and $H \parallel c$ axis and at zero field (NQR) for the "as-grown" $CaFe_2As_2$, together with the data measured in the "annealed" $CaFe_2As_2$.

Figure 4.5 shows $1/T_1T$ versus T for $H \parallel ab$ plane and $H \parallel c$ axis at $H = 6$ -7 T. In both the "as-grown" and "annealed" samples, above $T_s(\sim 96$ K) and $T_N(\sim 167$ K) respectively, $1/T_1T$ for $H \parallel ab$ plane shows a monotonic increase with decreasing T, while $1/T_1T$ for $H \parallel c$ axis is nearly independent of T. The T dependencies of $1/T_1T$ in the "annealed" $CaFe_2As_2$ are in good agreement with that of $1/T_1T$ in the Sn-flux $CaFe_2As_2$ [185].

Below T_s, $1/T_1T$ decrease suddenly and become T-independent following the Korringa relation $(T_1T)^{-1} =$ constant at low T. There is no anisotropy in $1/T_1T$ below T_s. $1/T_1T$ is also measured by the ^{75}As NQR, which are shown in Fig. 4.5 by solid light green triangles. The results are in good agreement with the T dependence of ^{75}As NQR in the LT c$-\mathcal{T}$ phase induced by the application of high pressure 10.8 kbar on $CaFe_2As_2$ crystals [175][176]. The $1/T_1T$ data by NQR at zero field are in good agreement with that obtained from the NMR with $H \parallel c$ axis values which is consistent with the fact that the EFG at the As-site is parallel to the c-axis which is the quantization axis. This also implies that there is no effect of magnetic field on T_1 values.

In order to see spin fluctuation effects in the paramagnetic state, it is useful to replot the

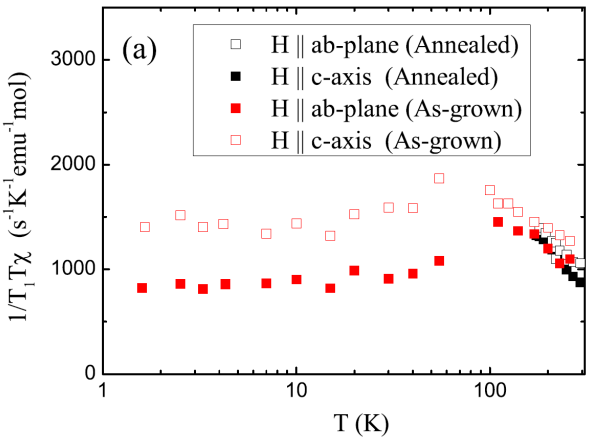

Figure 4.6 (Color online) $1/T_1T\chi$ vs T for both magnetic field directions, $H \parallel c$ axis and $H \parallel ab$ plane in the "as-grown" sample. T dependencies of $1/T_1T\chi$ for both H directions in the "annealed" $CaFe_2As_2$ are also plotted for comparison. The increase of $1/T_1T\chi$ vs T observed above T_s indicates the growth of the stripe-type AFM spin correlations

data by changing the vertical axis from $1/T_1T$ to $1/T_1T\chi$ as shown in Fig. 4.6, where the corresponding corrected χ was used for each H direction. $1/T_1T$ can be expressed in terms of the imaginary part of the dynamic susceptibility $\chi''(\vec{q},\omega_0)$ per mole of electronic spins as[150]:

$$\frac{1}{T_1T} = \frac{2\gamma_N^2 k_B}{N_A^2} \sum_{\vec{q}} |A(\vec{q})|^2 \frac{\chi''_M(\vec{q},\omega_0)}{\omega_0} \tag{4.2}$$

where the sum is over the wave vectors $\vec{q}$ within the first Brillouin zone, $A(\vec{q})$ is the form factor of the hyperfine interactions, and $\chi''(\vec{q},\omega_0)$ is the imaginary part of the dynamic susceptibility at the Larmor frequency ω_0. On the other hand, the uniform χ corresponds to the real component $\chi'(\vec{q},\omega_0)$ with $q = 0$ and $\omega_0 = 0$. Thus a plot of $1/T_1T\chi$ versus T shows the T dependence of $\sum_{\vec{q}} |A(\vec{q})|^2 \chi''_M(\vec{q},\omega_0)$ with respect to that of the uniform susceptibility $\chi'(0,0)$. Above T_s, $1/T_1T\chi$ for $H \parallel c$ axis and $H \parallel ab$ plane in both samples increase with decreasing temperature. The increase implies $\sum_{\vec{q}} |A(\vec{q})|^2 \chi''_M(\vec{q},\omega_0)$ increases more than $\chi'(0,0)$, which is due to a growth of spin correlations with $q \neq 0$, stripe-type AFM wave vector $\vec{q} = Q_{AF}$ as discussed in the following. Thus we conclude that strong AFM spin fluctuations are realized in the HT $\mathcal{T}$ phase in both the "annealed" and "as-grown" $CaFe_2As_2$ crystals, consistent with INS measurements

[173][186]. Below T_s, in the LT c$-\mathcal{T}$ phase, on the other hand, $1/T_1T\chi$ are nearly independent of T showing that the T dependence of $\sum_{\vec{q}}|A(\vec{q})|^2\chi''_M(\vec{q},\omega_0)$ is almost similar to the T dependence of χ. This indicates that the LT c$-\mathcal{T}$ phase is devoid of AFM spin correlations.

According to previous NMR studies performed on Fe pnictides [187][188][189] and on $SrCo_2As_2$ [190], the ratio $r \equiv T_{1,c}/T_{1,ab}$ depends on AFM spin correlation modes as:

$$r = \begin{cases} 0.5 + \left(\frac{\mathcal{S}_{ab}}{\mathcal{S}_c}\right)^2 & \text{for stripe AFM fluctuations,} \\ 0.5 & \text{for Nèel-type AFM fluctuations} \end{cases} \tag{4.3}$$

where $\mathcal{S}_\alpha$ is the amplitude of the spin fluctuation spectral density at NMR frequency along the α direction. Fig. 4.7 shows that the $r > 1$ in both HT $\mathcal{T}$ phase and the LT c$-\mathcal{T}$ phase of both the "as-grown" and "annealed" crystals of $CaFe_2As_2$. In the HT $\mathcal{T}$ phase, r increases with decreasing T, while in the LT c$-\mathcal{T}$ phase it is almost constant ≈ 1. This result backed up with the increase of $1/T_1T\chi$ shown in Fig. 4.6, enables us to conclude that stripe-type AFM spin fluctuations are realized in the HT $\mathcal{T}$ paramagnetic state. Nèel-type spin fluctuations can be clearly ruled out because according to Eq. 4.3, that would require $r = 0.5$, which is in conflict with our measurements shown in Fig. 4.7 which gives $r > 1.0$.

On the contrary since we do not observe any signature of AFM correlations in LT c$-\mathcal{T}$ phase either from the T dependence of $1/T_1T\chi$ or from the NMR spectrum, we conclude that electron correlations melt in this phase. This is consistent with inelastic neutron scattering measurements [173][186] and with the results of ARPES [190], both of which demonstrate the evidence of the absence of magnetic fluctuations in the nonsuperconducting c$-\mathcal{T}$ phase in $CaFe_2As_2$.

4.1.4 Conclusion

In this chapter we focussed on the parent compound of the family of "122" iron arsenide $CaFe_2As_2$. Different magnetic properties at low temperatures originating from different heat treatments in the preparation of the sample were studied by ^{75}As NMR and NQR. From the NMR and NQR spectra, the Knight shift and the $1/T_1$ data, we could conclude that while at high temperatures both the "as-grown" and the "annealed" crystals of $CaFe_2As_2$ are in

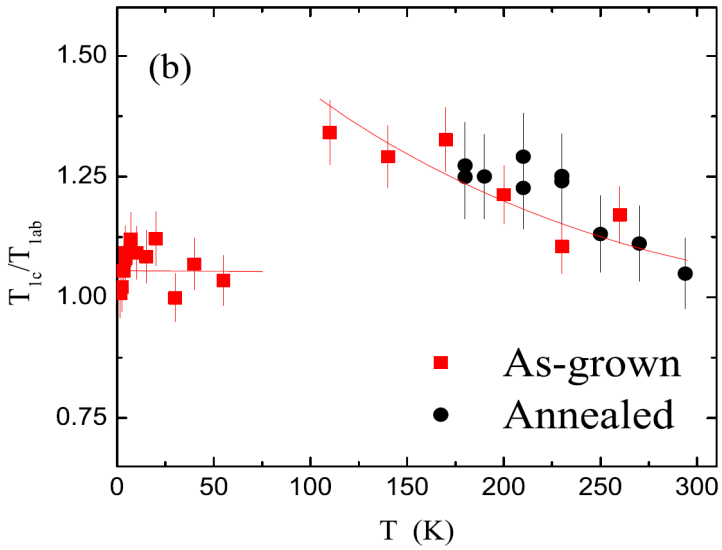

Figure 4.7 (Color online) T dependence of the ratio $r \equiv T_{1,c}/T_{1,ab}$. The solid lines are guides to the eye.

the $\mathcal{T}$ paramagnetic phase, at low temperatures their magnetic properties differ drastically. Below $T_N \sim 167$ K, the "annealed" sample showed magnetically long-range ordered $\mathcal{O}$ phase, whereas the "as-grown" sample showed a structural transition at $T_s \sim 96$ K to a non-magnetic c$-\mathcal{T}$ phase. Stripe-type AFM correlations in the HT $\mathcal{T}$ phase were confirmed from the T dependence of $1/T_1T\chi$ and of the ratio $r \equiv T_{1,c}/T_{1,ab}$, while no magnetic correlations were seen in the LT c$-\mathcal{T}$. The lack of any magnetic broadening of NMR spectrum and T-independent Knight shift demonstrate no development of static Fe spin correlations in the c$-\mathcal{T}$ phase. These observations, combined with the recent INS measurements showing the absence of magnetic fluctuations, bring us to the conclusion that electron correlations completely disappear in a wide energy scale from NMR to INS techniques in the nonsuperconducting c$-\mathcal{T}$ phase in $CaFe_2As_2$.

CHAPTER 5. LOCALIZED FRUSTRATED 3D SYSTEMS - I

5.1 $CoAl_2O_4$

The ambient pressure NMR data on $CoAl_2O_4$ mentioned in this chapter is published in [191].

5.1.1 Introduction

The investigation of magnetism in the insulating A-site spinel-structure compound $CoAl_2O_4$ has a long history which started with a suggestion of a long-range antiferromagnetic (AFM) ordering below 4 K from magnetic susceptibility χ and neutron diffraction measurements performed by Roth.[192] The magnetism of this system originates from Co^{2+} ions $[(e_g)^4(t_{2g})^3]$ with spin $S = 3/2$ at the tetrahedral A-sites which form a diamond lattice. Later on, the interest shifted to the spin frustration effects in the A-site spinel compounds after the ground state of the diamond lattice AFM was investigated theoretically.[193] The diamond lattice is composed of two interpenetrating face-centered cubic (fcc) sublattices(Fig. 5.1). The frustration is caused by the next-nearest-neighbor antiferromagnetic interaction J_2 which couples nearest neighbor sites of each fcc sublattice of the diamond structure, while the nearest-neighbor interaction J_1 between the two fcc sublattices alone does not induce any frustration for AFM ordering.

Different A-site spinels exhibit various ground states depending on what the A and the B ions are: a spin-orbital ground state is proposed in the case of $FeSc_2S_4$,[194, 195] and a spin-glass state for $FeAl_2O_4$.[196, 197] Mn compounds are spin-only systems. An orbital glass state is inferred for $FeCr_2S_4$.[194, 198] $MnSc_2S_4$ shows a spiral magnetic ordering[194, 195, 199] while $MnAl_2O_4$[196, 200, 201] has a long range antiferromagnetically ordered ground state. $CoRh_2O_4$[203] and $CoCo_2O_4$[192, 202, 203] both have antiferromagnetic ground states with T_N

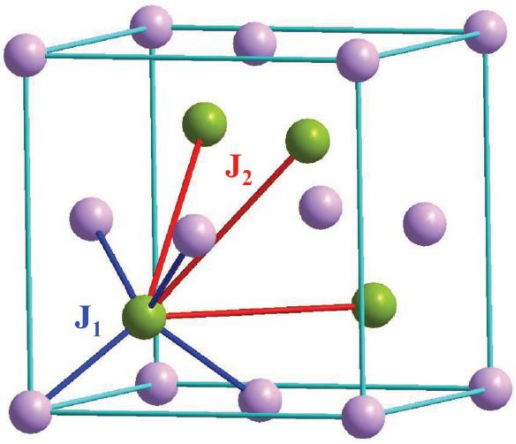

Figure 5.1 (Color online) Structure of $CoAl_2O_4$[191]

= 25 K and 34-40 K, respectively.

Bergman *et al.*[193] pointed out theoretically that the ground state of the diamond lattice is a Néel-type antiferromagnet for a ratio of $J_2/J_1 < 1/8 = 0.125$. The ground state changes to a spiral spin liquid state for $J_2/J_1 > 1/8$. J_1 and J_2 for $CoAl_2O_4$ are reported to be $J_1 = 0.92(1)$ meV ≈ 10.67 K and with $J_2 = 0.101(2)$ meV ≈ 1.17 K, $J_2/J_1 = 0.11$.[204] Since the ratio is close to the critical ratio of $J_2/J_1 = 1/8$, $CoAl_2O_4$ is considered to be located in the critical region between the AFM and the spiral spin liquid states.

Experimental observations of the ground state of $CoAl_2O_4$ are contradictory. Tristan *et al.*[196] reported from neutron scattering experiments on powder samples that a spin-glass state is realized below 4.8 K with a high frustration parameter[205] $f = |\theta_{CW}|/T_M = 22$, where θ_{CW} is the Curie-Weiss temperature and T_M is the AFM magnetic ordering temperature T_N or the spin-glass transition temperature T_g, as the case may be. On the other hand, Suzuki proposed a possible spin liquid ground state below 9 K[203] with $f = 10$ (where T_M is taken to be T^*, the temperature at which a broad peak of the heat capacity C is observed). Zaharko *et al.* suggested a magnetically ordered phase which remains 'nonconventional' down to 1.5 K from neutron powder diffraction[206] (below 5 K) and single-crystal neutron diffraction experiment[204] (below 8 K). MacDougall also carried out a neutron diffraction experiment on a single crystal of $CoAl_2O_4$ which showed a sharp cusp at 6 K in the T-dependence of χ and

an AFM state below 6 K.[207] The origin of this ambiguity is probably the microstructure effects such as site inversion, as has been pointed out by Zaharko *et al.*[204] The degree of site inversion between the A- and B-sites is usually defined by an inversion parameter x in the formula $(Co_{1-x}Al_x)[Al_{2-x}Co_x]O_4$. The x value depends on the method of preparation. The x values of the polycrystalline samples reported by Suzuki *et al.*[203], Tristan *et al.*[196, 208] and Zaharko *et al.*[206] are 0.04(1), 0.08-0.104 and 0.17, respectively. The x values for the single-crystal samples studied by Zaharko[204] and MacDougall[207] are 0.08 and 0.02(4), respectively.

Quite recently Hanashima *et al.*[209] carried out a systematic study of the effects of site inversion on the magnetic properties of $(Co_{1-x}Al_x)[Al_{2-x}Co_x]O_4$ where x is controlled from 0.0467 to 0.153 by changing the heat treatment. The χ of the highest-quality sample with $x = 0.0467$ shows a broad maximum at 14 K and does not show any signature of magnetic ordering down to 2 K, similar to that reported by Suzuki *et al.*,[203] indicating a spin liquid state. With increasing x, the broad maximum moves to lower temperature (10 K for $x = 0.0643$), and for $x > 0.101$, a clear cusp in the T-dependence of χ is observed which is attributed to a spin-glass transition below $T_g \approx 4.5$ K. In the intermediate region $0.0791 < x < 0.847$, a coexistence of the spin-liquid state and spin-glass state is proposed. Hanashima concludes that with increasing x the spin-liquid state collapses and the spin-glass order emerges for $x > 0.101$. It is important to understand whether the intrinsic ground state of $CoAl_2O_4$ for small values of x is a spin-glass state, a collinear antiferromagnet or a spin-liquid state due to the spin frustration. To investigate the ground state of $CoAl_2O_4$ one needs a high-quality sample with small value of the inversion parameter x.

It is also interesting to note that the value of frustration parameter f depends strongly on the site disorder x. Table 5.1 shows the comparison of f and x of $CoAl_2O_4$ from different papers. The details of the structural, the neutron diffraction and the magnetization properties of the sample used for our NMR study is in Ref.[191]. Thus we utilize the tool of nuclear magnetic resonance (NMR) to investigate the ground state of $CoAl_2O_4$.

Table 5.1 Parameters obtained from magnetic susceptibility $\chi(T)$ data and their fit using high temperature Curie-Weiss law for some $CoAl_2O_4$ samples reported in the literature have been shown. The listed parameters in the table are site-inversion parameter x, AF magnetic ordering temperature T_N, temperature at which the ZFC and FC susceptibilities deviate and the temperature are at which broad peak of heat capacity is observed both denoted by T^*, spin-glass transition T_g, Curie-Weiss temperature θ_{CW}, frustration parameter $f = |\theta_{CW}|/T_M$ (where T_M is T_N, T^* or T_g), effective paramagnetic moment μ_{eff} and spectroscopic splitting factor g obtained by considering spin only $S = 3/2$ state of Co^{2+} ions.

x	T_N	T^*	T_g	θ_{CW}	$f = \lvert\theta_{CW}\rvert$	μ_{eff}	g	Ground	Ref.
(%)	(K)	(K)	(K)	(K)	$/T_M$	(μ_B)		State	
6(1)	9.8(2)			-73(8)	8(1)	4.1(1)	2.12(5)	AFM	[191]
4(2)		9		-89(6)	9.9(7)	4.45(8)	2.30(4)	Spin Liquid	[203]
4.67		9.6		-93.0	9.7	4.36	2.25	Spin Liquid	[209]
2(4)	6			-109(1)	18.0(2)	4.89(3)	2.53(2)	AFM	[207]
8(3)			4.8(2)	-104(2)	22(1)	4.65(9)	2.40(4)	Spin Glass	[196]
8	8			-94(1)	12(1)	4.63(2)	2.40(1)	Magnetically	[204],
								ordered	[210]

5.1.2 Experimental Details

A well-characterized polycrystalline $CoAl_2O_4$ sample with the inversion parameter $x = 0.06(1)$ was used for the NMR experiments. The polycrystalline sample was synthesized by the solid-state reaction method using Co_3O_4 (99.9985%) and Al_2O_3 (99.995%) from Alfa Aesar as the starting materials, the details of which can be found in Ref.[191]. Nuclear magnetic resonance (NMR) measurements were conducted by probing the ^{27}Al nuclei ($I = 5/2$, $\gamma/2\pi = 11.09375$ MHz/T, $Q = 0.149$ barns) and the ^{59}Co nuclei ($I = 7/2$, $\gamma/2\pi = 10.03$ MHz/T, $Q = 0.4$ barns) by using a phase-coherent spin-echo pulse spectrometer. The NMR spectrum was taken by recording the spin-echo signal intensity while sweeping the external magnetic field at a fixed resonance frequency. The Co NMR spectrum under zero magnetic field was obtained by plotting the spin-echo intensity point by point at different fixed frequencies. The $CoAl_2O_4$ exhibits an antiferromagnetic ordering below the Néel temperature of 9.8(2) K confirmed by the neutron diffraction study[191] which indicates a collinear antiferromagnetic ordering below T_N. The ground state properties do not change much with application of pressure.

5.1.3 Nuclear Magnetic Resonance measurements : ^{27}Al-NMR

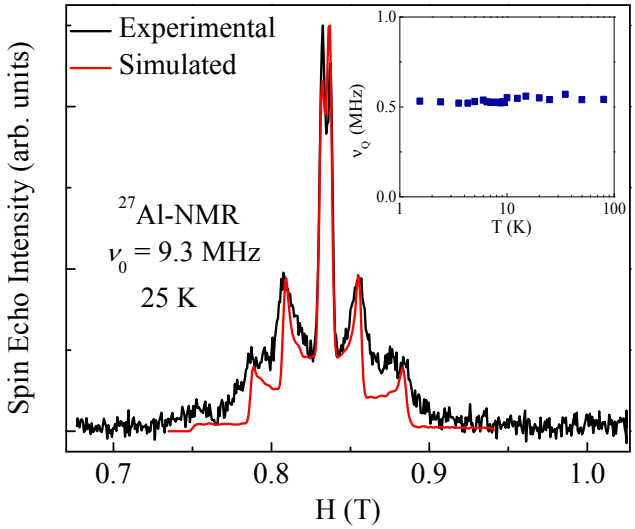

Figure 5.2 (Color online) Field-swept ^{27}Al-NMR spectrum at 25 K and ν_0 = 9.3 MHz. The red line shows the simulated spectrum with ν_Q = 0.55 MHz and η =0. The inset shows the temperature independence of the quadrupole frequency ν_Q.

Figure 5.2 shows the field-swept ^{27}Al NMR spectrum at T = 25 K and resonance frequency ν_0= 9.3 MHz. Since our sample consists of grains with randomly oriented crystal axes, the spectrum is a powder pattern. The spectrum can be explained by a combination of a large Zeeman interaction $\mathcal{H}_Z$ and a small quadrupole interaction $\mathcal{H}_Q$. The nuclear spin Hamiltonian can be expressed as,

$$\mathcal{H} = \mathcal{H}_Z + \mathcal{H}_Q \tag{5.1}$$

where $\mathcal{H}_Z = -\gamma\hbar H_0(1+K)I_z$ and $\mathcal{H}_Q = \frac{e^2qQ}{4I(2I-1)}[(3I_z^2 - I^2) + \frac{1}{2}\eta(I_+^2 + I_-^2)]$, Q is the quadrupole moment of the ^{27}Al nucleus and K is the NMR shift which is a sum of isotropic ($K_{\rm iso}$) and axial ($K_{\rm ax}$) parts. η is the asymmetry parameter for the electric field gradient (EFG) defined by $\frac{\frac{\partial^2 V}{\partial X^2} - \frac{\partial^2 V}{\partial Y^2}}{\frac{\partial^2 V}{\partial Z^2}}$, $|\frac{\partial^2 V}{\partial Z^2}| > |\frac{\partial^2 V}{\partial Y^2}| > |\frac{\partial^2 V}{\partial X^2}|$, $eq = |\frac{\partial^2 V}{\partial Z^2}|$ and the quadrupole frequency $\nu_Q = \frac{3e^2qQ}{2I(2I-1)h}$. The z and Z axes are the quantization axes for the Zeeman and quadrupole interactions, respectively. The observed spectrum is well reproduced by a simulated spectrum shown by a red line in

Fig. 5.2 with $\nu_Q = 0.55$ MHz and $\eta = 0$. The value of ν_Q is independent of T in the measured range of 1.8 K - 300 K within our experimental uncertainty as shown in the inset of Fig. 5.2. In contrast, $K_{\rm iso}$ and $K_{\rm ax}$ show weak temperature dependences. The weak T dependencies of the NMR shifts are consistent with previous data reported by Miyatani *et al.*[211] who measured the ^{27}Al-NMR spectrum in $CoAl_2O_4$ with the continuous-wave NMR method above 77 K, although the $K_{\rm ax}$ component was not detected in the previous measurement.

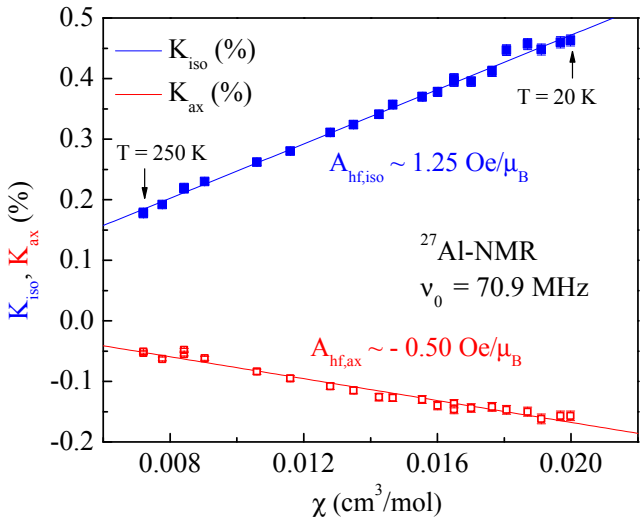

Figure 5.3 (Color online)^{27}Al-NMR shifts ($K_{\rm iso}$ and $K_{\rm ax}$) versus χ plots with T as an implicit parameter. The solid lines show the linear fit using the Eq. (6.1).

The T dependencies of $K_{\rm iso}$ and $K_{\rm ax}$ follow the T dependence of χ as shown in Fig. 5.3 where the NMR shifts are plotted as a function of χ with T as an implicit parameter. Here the NMR shifts are determined by measuring the NMR spectrum with a higher resonance frequency of 70.9 MHz to improve the accuracy. The NMR shift has contributions from the T-dependent spin part $K_{\rm spin}$ and a small T-independent orbital part K_0. $K_{\rm spin}(T)$ is related to the spin susceptibility with hyperfine coupling constant $A_{\rm hf}$ as follows:

$$K(T) = K_0 + \frac{A_{\rm hf}}{N_{\rm A}}\chi(T), \tag{5.2}$$

where $N_{\rm A}$ is the Avogadro number. The isotropic ($A_{\rm hf,iso}$) and axial ($A_{\rm hf,ax}$) parts of the

hyperfine coupling constants for the Al nucleus are evaluated from the slope of the K-χ plots (Fig. 5.3) to be 1.25(2) kOe/μ_B and $-0.50(2)$ kOe/μ_B respectively, and K_0 is 0.023(4) % and 0.013(3) % for the isotropic and axial parts, respectively. Classical dipolar field calculations indicate that the hyperfine field cannot be due to the classical dipolar field at the Al-sites from neighboring Co^{2+} ($S = 3/2$) spins, but is rather due to the transferred hyperfine field due to finite spin transfer from Co^{2+} spins. The anisotropy in the hyperfine field suggests that anisotropic orbitals such as the $2p$ and $3p$ orbitals on Al atoms are polarized by the spin transfer from the neighboring Co atoms.

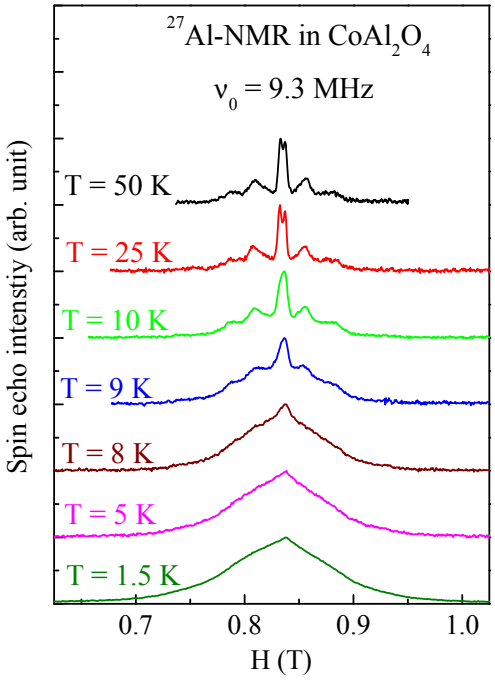

Figure 5.4 (Color online) Field-swept ^{27}Al-NMR spectra at various temperatures with resonance frequency $\nu_0 = 9.3$ MHz.

The spectrum starts to broaden suddenly below ≈ 10 K, as shown in Fig. 5.4. The broadening indicates a static magnetic ordering of the Co^{2+} spins which produce a finite static internal field at the Al-sites. The symmetric line broadening indicates an antiferromagnetic

state. Figure 5.5 shows the T dependence of the line width (ΔH) determined at 10 % of the peak intensity. Since the broadening of the ^{27}Al-NMR linewidth in our polycrystalline sample below ≈10 K is produced by the Co^{2+} spin moments in the magnetically ordered state, the T dependence of the linewidth reflects that of the sublattice magnetization in the AFM state. The Néel temperature T_N and the critical exponent β are determined by fitting ΔH near T_N in Fig 5.5 by

$$\Delta H(T) = \Delta H_0 \left(1 - \frac{T}{T_N}\right)^{\beta} + c, \tag{5.3}$$

where $\Delta H_0 \approx 1669$ Oe and $c \approx 1145$ Oe is a constant determined by averaging the nearly T-independent ΔH above T_N. By fitting data in the temperature range of 7.5 K $< T <$ 10 K, by Eq. 5.3, T_N is estimated to be 9.8(2) K and $\beta = 0.65(5)$.

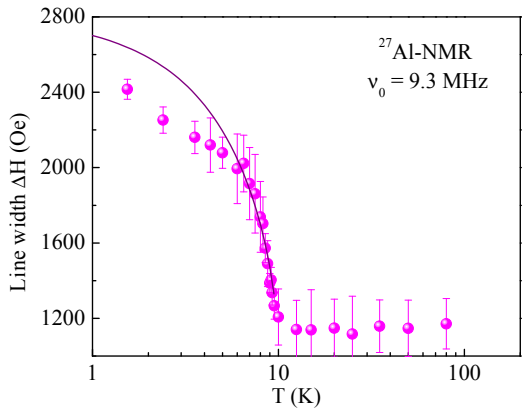

Figure 5.5 (Color online) T-dependence of line width at 10% of the peak intensity. The solid purple line shows the fit by Eq. 5.3 in the temperature range 7.5 K $< T <$ 10 K.

5.1.4 Nuclear Magnetic Resonance measurements : ^{59}Co-NMR

In the paramagnetic state at $T = 125$ K, we observe two peaks in the ^{59}Co-NMR spectrum as shown in Fig. 5.6. With decreasing T, the peak observed at $H \approx 6.9$ T shifts to higher magnetic field and the other peak at $H \approx 6.8$ T moves to slightly lower magnetic field. While the former peak disappeared below 10 K, the latter peak could be observed down to the lowest

temperature of 1.5 K. These behaviors are very similar to ^{59}Co-NMR data for the magnetic Co^{2+} ($S = \frac{3}{2}$) at the A-site and nonmagnetic low-spin Co^{3+} [$(t_{2g})^6(e_g)^0$, $S = 0$] at the B-site in the spinel-structure antiferromagnet Co_3O_4 with $T_N = 34$ K. [202] Thus the former signal, which vanishes due to very large internal field at Co^{2+} site, can be assigned to be the Co at the tetrahedral A-site and the latter signal can be attributed to the Co occupying the octahedral B-site.

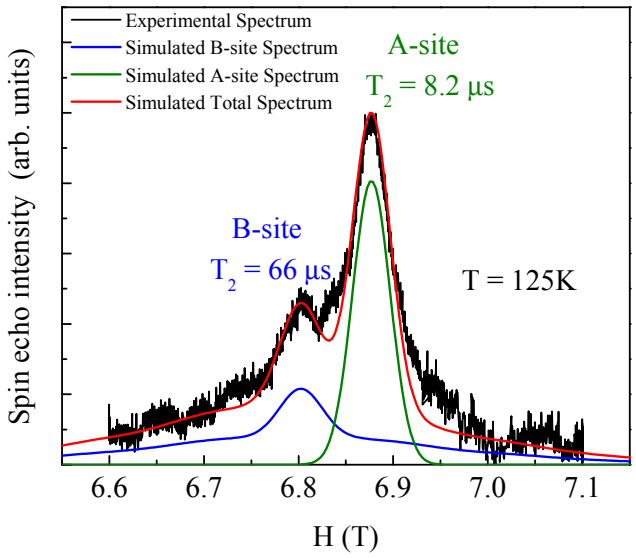

Figure 5.6 (Color online) Field-swept ^{59}Co-NMR spectrum at $T = 125$ K and resonance frequency $\nu_0 = 70.2$ MHz. The two peaks correspond to the Co ions occupying the A-site (magnetic Co^{2+} ion) and the B-site (nonmagnetic Co^{3+} ion), respectively. The transverse relaxation time $T_2 = 8.2$ μs and $T_2 = 66$ μs for the A- and B-sites, respectively.

From the intensities of the Co signals occupying the A and the B sites, corrected by their respective longitudinal and transverse relaxation times (T_1 and T_2, respectively), we have evaluated the inversion parameter to be $x \approx 0.06(2)$. This value is in good agreement with that obtained from the x-ray analysis[191]. We notice that the T dependence and the magnitude of the NMR shift of the Co signal from the B-sites in $CoAl_2O_4$ is very close to that observed in the

Co NMR signal from the B-sites in Co_3O_4 where the Co^{3+} ions are in nonmagnetic state with low spin $S = 0$ state.[202] From these results, we may consider that the Co ions occupying the B site in $CoAl_2O_4$ could be Co^{3+} with low spin state as in the case of Co ions at the B site in Co_3O_4. This could be possible if we assume that the deviation from oxygen stoichiometry exists as in $(Co_{1-x}Al_x)[Al_{2-x}Co_x]O_{4+\delta}$ to satisfy charge compensation of the compound. However, we can not rule out completely that the observed nonmagnetic Co is from an impurity phase, although it seems unlikely.

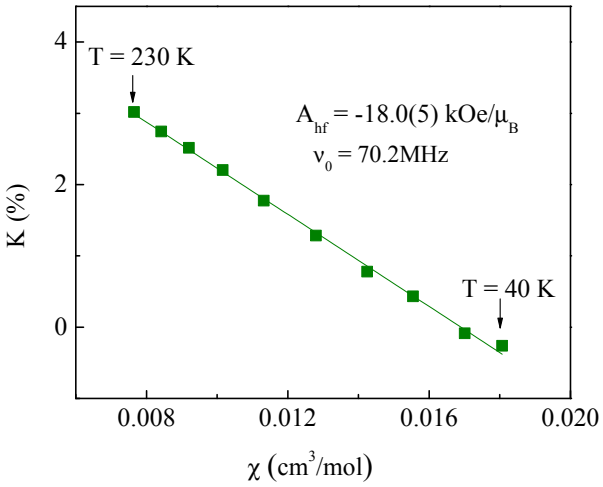

Figure 5.7 (Color online) ^{59}Co-NMR shift K versus χ plots with T as an implicit parameter. The solid line is a linear fit.

The hyperfine coupling constant of Co at the A-site is estimated from the $K - \chi$ plot in Fig. 5.7 to be $-18.0(5)$ kOe/μ_B which is considerably smaller in magnitude than the value of -105 kOe/μ_B for a free Co^{2+} ion. Such a small Co hyperfine coupling constant at the A-site has been reported previously to be -18.3 kOe/μ_B and -15.7 kOe/μ_B in the antiferromagnetic Co_3O_4 ($T_N = 34$ K) (Ref. [202]) and in ferrimagnetic $CoCr_2O_4$ ($T_C = 97$ K) (Ref. [212]), respectively. The small coupling constant was well explained by taking the second-order orbital moment due to the spin-orbit interaction into consideration. Here we present a similar discussion as shown in the previous papers.[212, 202]

The major contributions to the magnetic hyperfine coupling constant at the ^{59}Co nucleus are dominated by the d core polarization ($A_{\rm hf}^{\rm core}$), dipolar ($A_{\rm hf}^{\rm dip}$) and orbital ($A_{\rm hf}^{\rm orb}$) terms:[212, 202, 213]

$$A_{\rm hf} = A_{\rm hf}^{\rm core} + A_{\rm hf}^{\rm dip} + A_{\rm hf}^{\rm orb}. \tag{5.4}$$

Due to the crystal-field effect, the ground state of the $Co^{2+}(d^7)$ ion occupying the tetrahedral A-site has four electrons in the two lower $e_{\rm g}$ orbitals and three in the upper three $t_{2\rm g}$ orbitals. So this electronic configuration results in $A_{\rm hf}^{\rm dip} = 0$. [202] For a free Co^{2+} ion, the d core polarization coupling constant is -105 kOe/$\mu_{\rm B}$. [214] Due to quenching of the orbital moment L_z, there is no finite contribution of the L_z in the first order. But if we consider the second order perturbation of the spin-orbit interaction, the orbital quenching is partially lifted. This contribution due to the spin-orbit coupling has a positive sign and is estimated to be 85.1 kOe/$\mu_{\rm B}$ for Co^{2+} ions at the tetrahedral sites.[202] From the Eq. 5.4, we obtain $A_{\rm hf} = -19.9$ kOe/$\mu_{\rm B}$, which can reasonably explain the experimental value of $-18.0(5)$ kOe/$\mu_{\rm B}$.

The temperature-independent orbital part of the NMR shift for the Co^{2+} at the A site is estimated to be $K_{\rm orb} = 5.46(3)$ % from the $K - \chi$ analysis. The $K_{\rm orb}$ relates to Van Vleck susceptibility $\chi_{\rm VV}$ for Co^{2+} at the A site as $K_{\rm orb} = \frac{A_{\rm orb}}{N_{\rm A}}\chi_{\rm VV}$ where $K_{\rm orb}$ is the orbital hyperfine coupling constant given by [215]:

$$A_{\rm orb} = 2\mu_{\rm B}\left\langle \frac{1}{r^3} \right\rangle \tag{5.5}$$

Here $\left\langle \frac{1}{r^3} \right\rangle$ is an average of $\frac{1}{r^3}$ over $3d$ electrons. Using $\left\langle \frac{1}{r^3} \right\rangle = 6.02$ a.u. for Co^{2+} (Ref. [216]), $\chi_{\rm VV}$ is estimated to be $4(2) \times 10^{-4}$ cm^3/mol which is in good agreement with T-independent magnetic susceptibility[191].

Below $T_{\rm N}$, we observe an NMR signal of Co nuclei at the A-site under zero magnetic field, which again confirms long-range magnetic ordering. Figure 5.8 shows the zero-field ^{59}Co-NMR spectrum at 1.6 K. A similar zero-field ^{59}Co-NMR spectrum at the A-site has been previously reported for the spinel compound Co_3O_4 in the antiferromagnetic state.[202] The resonance frequency $\nu_0 = 43.5(4)$ MHz at the peak intensity point is lower than $\nu_0 = 55.7$ MHz in Co_3O_4.[202] The internal field $H_{\rm int}$ at the Co A-site is evaluated to be 43.3(4) kOe at 1.6 K. With the value of $A_{\rm hf} = -18.0$ kOe/$\mu_{\rm B}$ deduced from the $K - \chi$ plot, the ordered moment

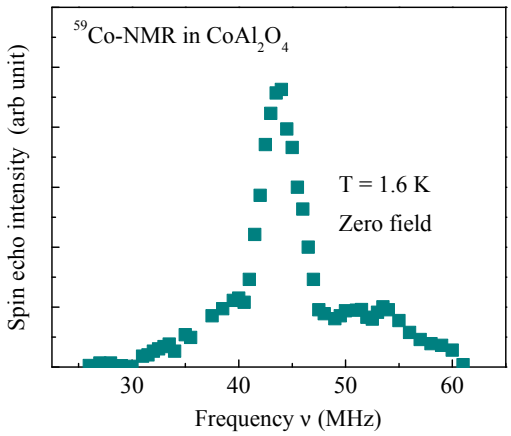

Figure 5.8 (Color online) ^{59}Co-NMR spectrum under zero external field at 1.6 K.

$\langle\mu\rangle$ of Co^{2+} is estimated to be 2.41(9) μ_B/Co using a relation $H_{int} = |A_{hf}|\langle\mu\rangle$. This value is smaller than the expected value of 3 μ_B/Co for $S = 3/2$ of Co^{2+} ions with $g = 2$ and is larger than the value of 1.58 μ_B/Co reported from the neutron diffraction study done previously by Zaharko *et al.*[204] The shoulderlike structures of the spectrum are due to a distribution of Co^{2+} ordered moments in the AFM state.

5.1.5 Nuclear Magnetic Resonance measurements : ^{27}Al spin lattice relaxation rates

In order to investigate the dynamical behavior of the Co^{2+} spins in $CoAl_2O_4$, ^{27}Al nuclear spin-lattice relaxation rates ($1/T_1$) were measured at different temperatures. In the case of ^{27}Al ($I = 5/2$), the nuclear magnetization recovery of the central transition after a $\pi/2$ saturation pulse is given by [217]

$$\frac{M(\infty) - M(t)}{M(\infty)} = (0.029e^{-t/T_1}) + (0.18e^{-6t/T_1}) + (0.79e^{-15t/T_1}) \tag{5.6}$$

where $M(t)$ is the nuclear magnetization at time t after the saturation pulse. The experimental recovery curves above T_N were well fitted by the equation, while below T_N the equation could

not fit the experimental data due to distributions of T_1. The distributions of T_1 are mainly due to the inhomogeneous broadening of the ^{27}Al-NMR spectrum in our powder sample and also due to the distribution of the Co^{2+} ordered moments in the AFM state. Then, we tentatively assumed that the experimental recovery curve is composed of two components, one with a short relaxation time T_{1S} and another with long relaxation time T_{1L} and we carried out a fit using the following equation:

$$\begin{aligned}\frac{M(\infty)-M(t)}{M(\infty)} = [M_S[(0.029e^{-t/T_{1S}}) + (0.18e^{-6t/T_{1S}}) \\ + (0.79e^{-15t/T_{1S}})] + M_L[(0.029e^{-t/T_{1L}}) \\ + (0.18e^{-6t/T_{1L}}) + (0.79e^{-15t/T_{1L}})]]\end{aligned} \tag{5.7}$$

where $M_S + M_L = 1$. The temperature dependence of M_S is shown in the inset of Fig. 5.9.

Figure 5.9 shows the temperature dependence of $1/T_{1S}$ and $1/T_{1L}$. With decreasing T, $1/T_{1S}$ decreases and shows a minimum around 50 K and exhibits a sharp peak at $T = 10.0(5)$ K. The sharp peak of $1/T_1$ is due to critical slowing down of spin fluctuations expected for a second-order phase transition, which again confirms the AFM long-range magnetic ordering at T_N. Below 10 K, $1/T_1$ rapidly falls and then decreases slowly where both $1/T_{1S}$ and $1/T_{1L}$ show $T^{0.6}$ power-law behavior (shown by the straight lines in the figure) below 4 K. In the antiferromagnetically ordered state, $1/T_1$ is usually mainly driven by scattering of magnons, leading to T^3 or T^5 power-law temperature dependences due to a two- or three-magnon Raman process, respectively. The weak T dependence of $1/T_1 \sim T^{0.6}$ below 4 K cannot be explained by magnon scattering, and suggests the presence of other magnetic fluctuations in the magnetically ordered state, which could originate from spin frustrations and/or short-range magnetic coerrelations revealed by the neutron scattering measurements described in Ref. [191].

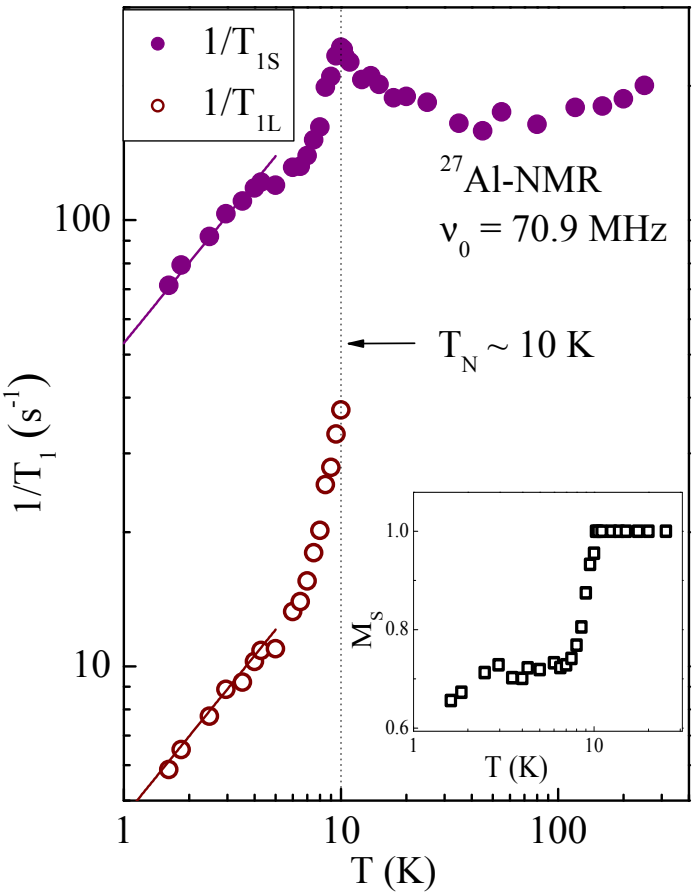

Figure 5.9 (Color online) T dependence of $1/T_{1S}$ and $1/T_{1L}$. Below 4 K, both $1/T_{1S}$ and $1/T_{1L}$ show $T^{0.6}$ power law behavior shown by the solid lines. The inset shows the T dependence of M_S.

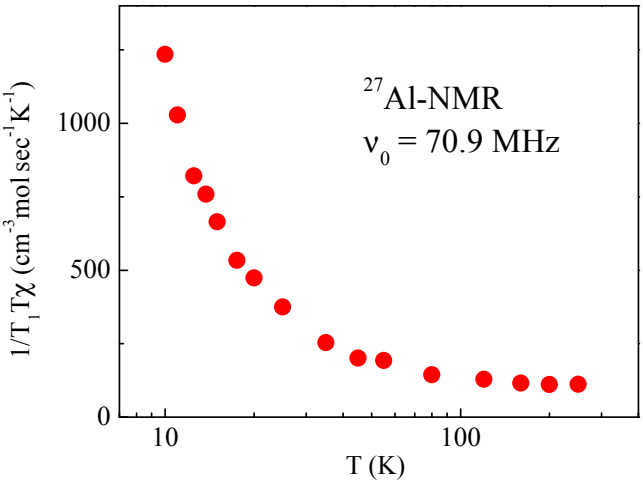

Figure 5.10 (Color online) Plot of $1/T_1T\chi$ versus temperature for a resonance frequency of 70.9 MHz. $1/T_1T\chi$ increases with decreasing temperature below 100 K indicating the growth of AFM spin correlations.

In order to see spin fluctuation effects in the paramagnetic state, it is useful to re-plot the data by changing the vertical axis from $1/T_1$ to $1/T_1T\chi$ as shown in Fig. 5.10. $1/T_1T$ can be expressed in terms of the imaginary part of the dynamic susceptibility $\chi''_{\rm M}(\vec{q},\omega_0)$ per mole of electronic spins as:[150, 218]

$$\frac{1}{T_1T} = \frac{2\gamma_N^2 k_{\rm B}}{N_{\rm A}^2}\sum_{\vec{q}}|A(\vec{q})|^2\frac{\chi''_{\rm M}(\vec{q},\omega_0)}{\omega_0} \tag{5.8}$$

where the sum is over the wave vectors $\vec{q}$ within the first Brillouin zone, $A(\vec{q})$ is the form factor of the hyperfine interactions and $\chi''_{\rm M}(\vec{q},\omega_0)$ is the imaginary part of the dynamic susceptibility at the Larmor frequency ω_0. On the other hand, the uniform χ corresponds to the real component $\chi'(\vec{q},\omega_0)$ with $q = 0$ and $\omega_0 = 0$. Thus, a plot of $1/T_1T\chi$ versus T in Fig. 5.10 shows the relative magnitude of $\sum_{\vec{q}}|A(\vec{q})|^2\chi''_{\rm M}(\vec{q},\omega_0)$ as compared to the uniform susceptibility $\chi(0,0)$. For high temperatures above 100 K, $1/T_1T\chi$ is nearly a constant showing that the temperature dependence of $\sum_{\vec{q}}|A(\vec{q})|^2\chi''_{\rm M}(\vec{q},\omega_0)$ is equivalent to that of $\chi'(0,0)$. On the other hand, with decrease in temperature, $1/T_1T\chi$ in Fig. 5.10 starts to increase below 100 K which is ~ 10 times

higher than T_N. The increase of the $1/T_1T\chi$ at $T >> T_N$ cannot be simply attributed to the critical slowing down of spin fluctuations near T_N. This implies $\sum_{\vec{q}}|A(\vec{q})|^2\chi''_M(\vec{q},\omega_0)$ increases more than $\chi'(0,0)$, which is due to a growth of spin fluctuations with $q \neq 0$, most likely with AFM wave vector $q = Q_{AF}$, even at T much higher than T_N. Thus we conclude that strong antiferromagnetic spin fluctuations are realized in a wide temperature region up to ∼100 K in the paramagnetic state.

5.1.6 High Pressure NMR study

Since the ratio of J_2/J_1 for $CoAl_2O_4$ is very close to the critical value of 1/8 which marks the boundary between an AFM state and a spiral spin liquid state[193], we wanted to observe whether application of pressure altered the J_2/J_1 ratio of the system such that its ground state changes from the AFM to the spin-liquid state. To study the effect of high pressure on the transition temperature and the ground state of $CoAl_2O_4$, we used a hybrid Cu-Be/NiCrAl clamp-type high-p cell (discussed in Chapter 1) to produce high pressure (p) on the sample up to 1.9 GPa at low temperature. Daphne oil 7373 was used as the p-transmitting medium. The sample pressure was calibrated using ^{63}Cu nuclear quadrupole resonance (NQR) measurements of Cu_2O based on the p and T dependences of the Cu-NQR frequency reported previously.[219, 220] We have done ^{27}Al-NMR study under 0.87 GPa and 1.90 GPa pressure.

The NMR spectra under pressure showed almost no change in shape or in the T dependence of line width as compared to the NMR spectra under ambient pressure. We witness a clear broadening of the spectra under pressure up to 1.9 GPa below the magnetic transition temperature $T_N \sim 10$ K and a distinct peak in the temperature dependence of $1/T_1$ (Fig. 5.11) at around ~ 10 K indicating a transition to a magnetic long-range ordered state. While above T_N, $1/T_1$ under all pressures (ambient, 0.87 GPa and 1.90 GPa) are same, in the magnetically ordered state they are different. It is observed that with pressure, the $1/T_1$ is suppressed for temperatures below T_N. A longer T_1 below T_N with application of pressure must be due to a change in the spin-wave spectrum since T_1 carries the information of the low-energy elementary excitations in the magnetically ordered state.

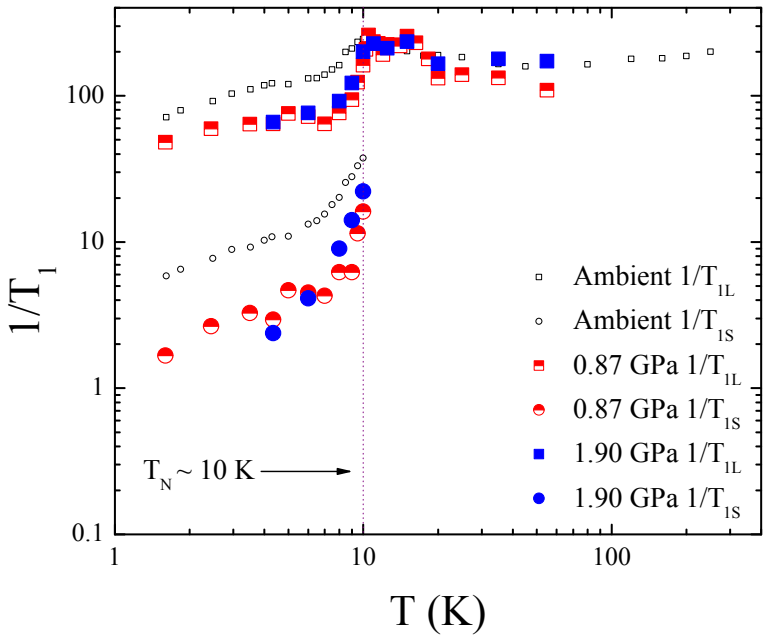

Figure 5.11 (Color online) $1/T_1$ for under high pressure

5.1.7 Conclusion

The NMR data clearly demonstrates that $CoAl_2O_4$ exhibits an AFM ground state below $T_N = 9.8(2)$ K. The symmetric broadening of the ^{27}Al-NMR spectrum below 10 K indicated the presence of a long-range AFM ordered ground state for this compound. Furthermore, the line width of the ^{27}Al-NMR spectrum which is proportional to the order parameter shows a continuous increase below 10 K. The presence of spontaneous magnetization below 10 K is confirmed directly by the observation of a ^{59}Co NMR signal under zero magnetic field in the magnetically ordered state. The sharp peak of $1/T_1$ for ^{27}Al-nucleus at around 10 K further confirms a phase transition to a long-range magnetically ordered state at the same temperature. This is consistent with the presence of a sharp peak in the heat capacity at $\simeq 9.7$ K[191] for this sample and with the neutron diffraction study[191] showing the emergence of (002) magnetic reflection intensity and its dependence on the scattering angle 2θ. The results from the neutron

diffraction measurements[191] are not only consistent with the NMR results but also indicate a collinear long-range AFM-ordered ground state for this compound with an ordered moment of 1.9(5) μ_B/Co.

The emergence of AFM correlations was manifested by the increase of $1/T_1T\chi$ for ^{27}Al-nucleus below 100 K. The presence of short-range correlations was also indicated by the magnetic entropy S_{Mag} at T_N which was considerably smaller than its value at high temperature[191]. Also, broad magnetic peaks are observed below 50 K in the neutron diffraction measurements, and the broad peak in χ (T) at $\approx$ 15 K [Ref.[191]] confirms the existence of short-range AFM correlations at $T > T_N$.

There are two interesting factors which govern the magnetic properties of this system, *viz*. frustration and site-inversion. We used a specially prepared polycrystalline sample of $CoAl_2O_4$ with a low inversion parameter $x = 0.057(20)$ for our NMR study. The value of x is a key parameter that determines the magnetic properties of $CoAl_2O_4$. Site disorder creates spin vacancies and increased randomness of exchange interactions in the already frustrated compound.[209] The suppression of the value of magnetic entropy[191] at high temperatures from the value expected for $S = 3/2$ suggests that the effective spin of the Co at the A-site is smaller than 3/2, which could be a manifestation of Co-Al site inversion effects. The low-temperature ordered magnetic moment is calculated from the NMR measurements to be around 2.4 μ_B which is smaller than the value of 3 μ_B expected for $g = 2$ and $S = 3/2$ system, mainly due to spin frustration effects. The site inversion between the A- and the B-sites creates spin vacancies in the system. The presence of short-range correlations below 100 K can be argued to be caused by frustration which suppresses the T_N to 10 K. In addition short-range correlations can arise due to disorder, associated with the site inversion. As pointed out previously, although a spin-liquid ground state has been proposed from magnetic susceptibility measurements for $CoAl_2O_4$ with low values of x,[203, 209] our NMR data conclusively proved the existence of a long-range AFM-ordered state below 10 K. Since site inversion plays a crucial role in determining the magnetic properties of this spinel compound, it will also be interesting to perform systematic NMR and neutron diffraction measurements in a highly disordered (high x) $CoAl_2O_4$ to investigate how the system changes from the AFM state to a spin glass state.

Application of pressure does not have any significant change in the magnetic transition temperature or on the ground state of the compound. The only effect is the suppression of the $1/T_1$ below T_N under pressure, the origin of which is not clear.

CHAPTER 6. LOCALIZED FRUSTRATED 3D SYSTEMS - II

6.1 $BiMn_2PO_6$

This chapter describes NMR work on $BiMn_2PO_6$ published in [120].

The family of compounds BiM_2PO_6 ($M \equiv$ Mn, Zn, Cu) represents very interesting two-leg spin-ladder systems. The structure of these compounds consists of MO_5 square pyramids with M^{2+} at its center. There are two crystallographically inequivalent M sites, $M1$ and $M2$ which share edges and form rungs of the ladder. These rungs are connected by the corner-sharing MO_5 square pyramids which build the buckled double chain ladder along the b-axis (Fig. 6.1). In this series of compounds, the exchange interactions between the nearest-neighbor (NN) M spins along the chain (J_1), along the rung (J_3) and in between ladders (J_4) and the next-nearest-neighbor (NNN) (J_2) along the chain are the most dominant interactions. In this chapter energies are expressed in temperature units.

The spin $S = 1/2$ member of this series of compounds $BiCu_2PO_6$ [221] shows low-dimensional magnetic features with a gapped spin liquid ($\Delta \sim 34$ K) ground state. For this compound J_1 and J_2 are almost equal in strength and sign (~ 170 K)[120] causing frustration. While the rungs are formed between the structural ladder units i.e., by the strong AFM J_4 (~ 154 K), the comparitively weak J_3 (~ 22 K) forms the interladder coupling. The spin dimensionality of the system still remains an open question. Depending on the strength of J_3 it can be quasi one-dimensional (1D) or quasi two-dimensional (2D). Thus, the very intricate magnetic structure of this low-spin system encouraged us to look into its high-spin analog $BiMn_2PO_6$.

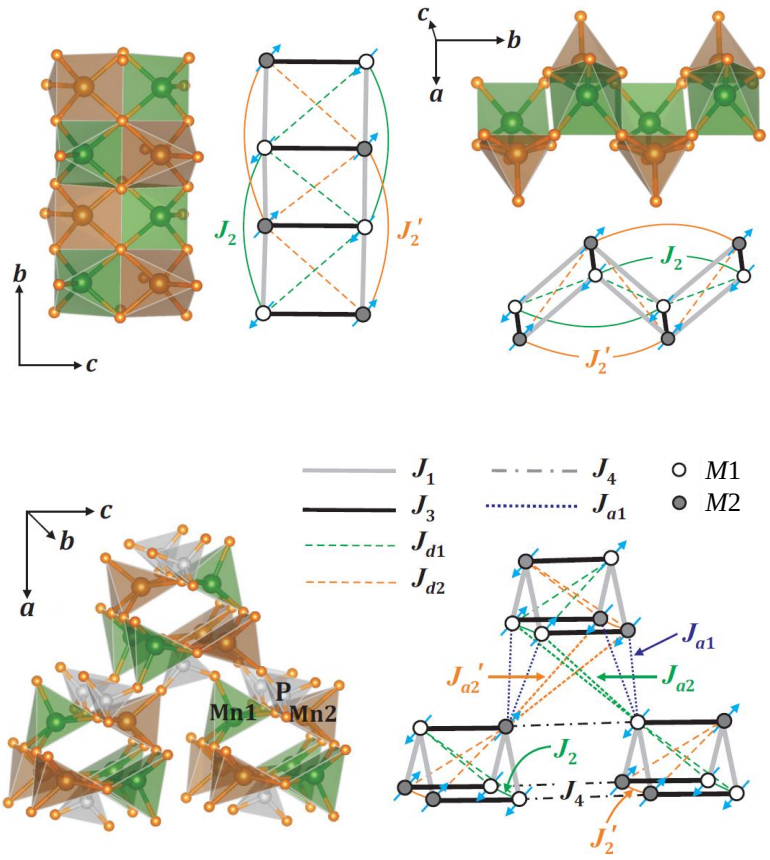

Figure 6.1 (Color online) [120] Crystal structure of $BiMn_2PO_6$. Green, brown, and gray polyhedra show Mn1O5, Mn2O5, and PO4, respectively. Open and filled circles denote the Mn1 and Mn2 positions, respectively. The definitions and signs of the different exchange couplings are discussed in the text.

While $BiCu_2PO_6$ presents a case of low-spin (Cu^{2+}, $S = 1/2, 3d^9$) system with low-dimensional magnetic behavior (broad peak in the temperature(T)-dependence of specific heat and magnetic susceptibility), $BiMn_2PO_6$ pushes the study towards classical limit with a large spin (Mn^{2+}, $S = 1/2, 3d^5$) and long-range ordering at ≈ 30 K with a 1D spatial anisotropy. In the latter compound the rungs are formed by the J_3, while the J_4 forms the interlayer exchange interaction. From the density-functional theory (DFT) band-structure calculations [120] $J_1 = 6.7$ K and $J_3 = 5.6$ K are estimated. The third dominant exchange interaction is between the neighboring spin ladders J_4 and is estimated to be 2.2 K. The comparable exchange interaction strengths play a primary role in the three-dimensional (3D) character of this compound. The magnetic susceptibility (χ) or the heat capacity ($C_{\rm p}(T)$) [120] do not show any broad peak characteristic of low-dimensional magnetism in this compound. Instead, we see a peak in the temperature (T)-dependence of χ and a sharp λ-type anomaly in the T-dependence of $C_{\rm p}(T)$ at $T_{\rm N} \approx 30$ K associated with magnetic LRO[120]. Additionally the T-dependent χ data for $BiMn_2PO_6$ suggested the possibility of two more phase transitions with a sudden jump at 43 K and a change in slope at 10 K in the $\chi - T$ plot [120]. No signature of a magnetic transition at 43 K or at 10 K was observed in the heat capacity data. Thus, to microscopically investigate the magnetic properties of the ground state and also to analyze the nature of the three transitions suggested by the χ data we did a ^{31}P-NMR study on $BiMn_2PO_6$. We present the results of the same in this chapter.

6.1.1 Experimental Details

Polycrystalline samples of $BiMn_2PO_6$ were prepared by solid-state reaction techniques using Bi_2O_3 (99.999%), MnO (99.99%), ZnO (99.99%), and $NH_4H_2PO_4$ (99.9%) as starting materials. The details of the sample preparation are given in Ref.[120]

Nuclear magnetic resonance (NMR) measurements were carried out on a polycrystalline sample using pulsed NMR techniques on ^{31}P nuclei with spin $I = 1/2$ and gyromagnetic ratio $\gamma_{\rm N}/2\pi = 17.2356$ MHz/T, over the T range 4 K $\leq T \leq$ 300 K. The NMR measurements were done at two radio frequencies, 77.5 MHz and 49.15 MHz. Spectra were obtained either by Fourier transform of the NMR echo signal or by sweeping the field at fixed frequency. The

NMR shift $K(T) = [H_{\rm ref} - H(T)]/H(T)$ was determined by measuring the resonance field $H(T)$ of the sample with respect to a standard H_3PO_4 solution (resonance field $H_{\rm ref}$). The ^{31}P nuclear spin-lattice relaxation rate $(1/T_1)$ was measured after applying a comb of saturation pulses.

6.1.2 NMR Measurements

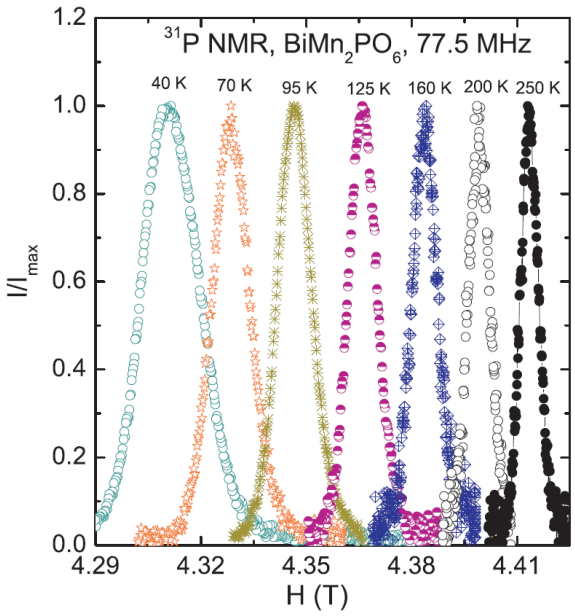

Figure 6.2 (Color online) ^{31}P-NMR spectra of intensity I versus magnetic field H measured at 77.5 MHz and at different temperatures.

With the purpose of examining the nature of the magnetic transitions and to elucidate static as well as dynamic properties of $BiMn_2PO_6$, we performed ^{31}P-NMR measurements on $BiMn_2PO_6$. Since all P atoms are crystallographically equivalent, for a nuclear spin $I = 1/2$, one would expect a single spectral line [118][108]. Indeed, we observe one narrow spectral line. Figure 6.2 shows how the ^{31}P-NMR spectra shifts with temperature. Figure 6.3 presents the T-dependence of the NMR shift, $K(T)$. At high T, K varies in a Curie-Weiss manner and shows a change in slope at about 30 K associated with the AFM ordering. Since the NMR shift is a direct measure of the spin susceptibility $\chi_{\rm spin}$, one can write $K(T)$ in terms of $\chi_{\rm spin}(T)$

$$K(T) = K_0 + \frac{A_{\rm hf}}{N_{\rm A}}\chi_{\rm spin}(T) \tag{6.1}$$

where K_0 is the T-independent chemical shift, $A_{\rm hf}$ is the hyperfine coupling constant of the ^{31}P nuclei to the Mn^{+2} spins, and $N_{\rm A}$ is Avogadro's number. $A_{\rm hf}$ can be calculated from the slope of a K versus χ plot with T as an implicit parameter. As seen in the inset of Fig. 6.3, the K versus χ plot is linear at high temperatures (T = 35 K - 250 K), yielding K_0 = (0.13 ± 0.03)% and $A_{\rm hf}$ = (7224 ± 85) Oe/$\mu_{\rm B}$. The temperature-independent shift K_0 contains an intrinsic chemical shift together with extrinsic contributions, including the remnant field of the field-sweep magnet which is not known exactly.

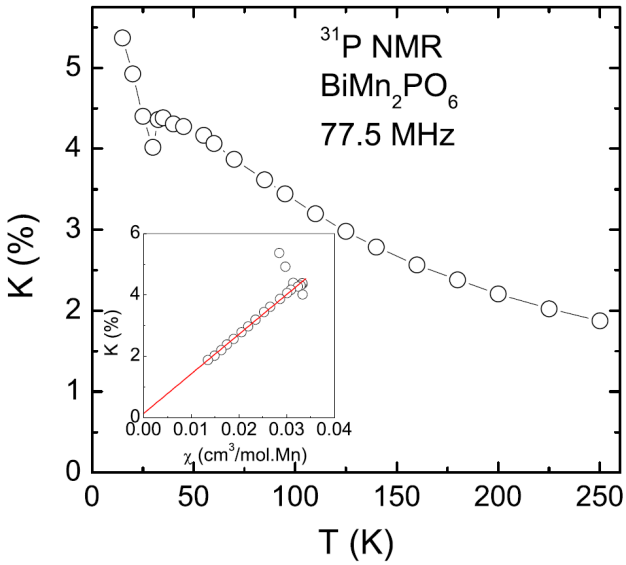

Figure 6.3 (Color online) ^{31}P-NMR shift K versus temperature T. The inset shows the K versus χ plot measured at H = 5 T with temperature as an implicit parameter. The solid (red) line is the linear fit.

The total hyperfine coupling constant at the P site is generally the sum of the transferred hyperfine ($A_{\rm trans}$) and dipolar ($A_{\rm dip}$) couplings produced by the Mn^{2+} spins, i.e., $A_{\rm hf} = z'\,A_{\rm trans} + A_{\rm dip}$, where z' is the number of nearest neighbor Mn^{+2} spins of the P site. The anisotropic dipolar couplings were calculated for three orientations using lattice sums. The maximum dipolar field contribution was calculated to be 800 Oe/$\mu_{\rm B}$, which is one order of magnitude

smaller than the total hyperfine field, suggesting that the dominant contribution to the total hyperfine coupling is due to the transferred hyperfine coupling at the P site. The total $A_{\rm hf}$ of the P site with the Mn^{2+} ions is 7224 Oe/$\mu_{\rm B}$. Each P atom has $z' = 6$ neighboring Mn^{2+} spins, so the $A_{\rm hf}$ due to one spin is $A_{\rm hf}/z' = 1.2$ kOe/($\mu_{\rm B}$ Mn) assuming a uniform hyperfine coupling to all z' Mn spins.

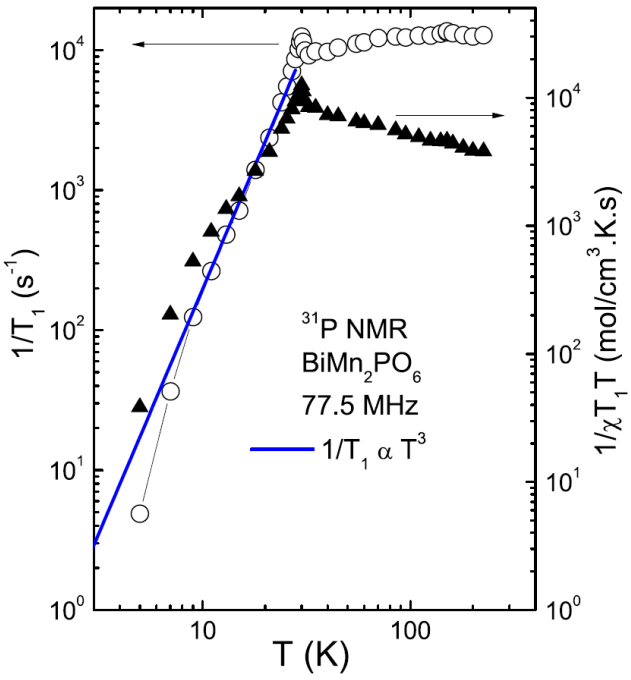

Figure 6.4 (Color online)^{31}P-nuclear spin-lattice relaxation rate $1/T_1$ and the corresponding $1/\chi T_1 T$ as a function of the temperature T are plotted along the left and right y-axes, respectively. The solid (blue) line corresponds to $1/T_1 \propto T^3$.

For an $I = 1/2$ nucleus, the recovery of the longitudinal magnetization is expected to follow a single-exponential behavior. In $BiMn_2PO_6$, the recovery of the nuclear magnetization after a combination of saturation pulses was indeed fitted well by the exponential function $[1-M(t)/M_0] = Ae^{-t/T_1}$, where $M(t)$ is the nuclear magnetization at time t after the saturation pulse and M_0 is the equilibrium magnetization. The temperature dependence of the nuclear spin-lattice relaxation rate $1/T_1$ estimated from the above fit is presented in Fig. 6.4. At high temperatures ($T \geq 70$ K), $1/T_1$ is almost temperature-independent, which is typical in the paramagnetic regime ($T >> J_{\rm max}/k_{\rm B}$), where $J_{\rm max}$ is the maximum exchange interaction in

the system [126]. With decreasing T, $1/T_1$ decreases slowly for $T < 70$ K and then shows a peak at around 30 K. This decrease in $1/T_1$ with decreasing T above T_N resembles the behavior of the AFM square-lattice compound $Pb_2VO(PO_4)_2$ [109]. The peak at $T_N \approx 30$ K is associated with the onset of 3D LRO and is consistent with the thermodynamic measurements [120]. For $T < T_N$, $1/T_1$ decreases rapidly.

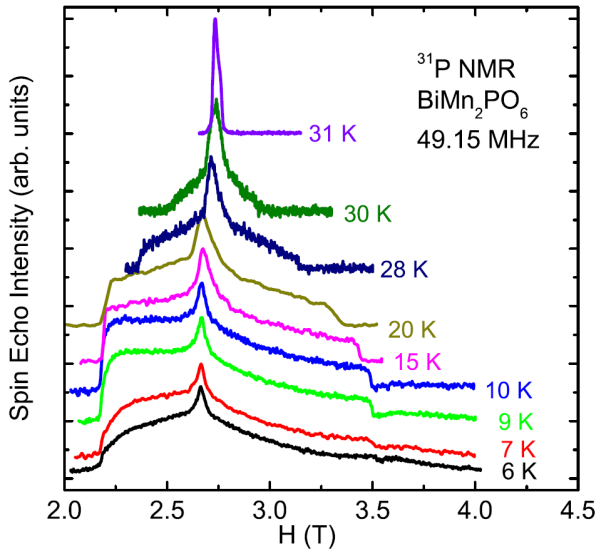

Figure 6.5 (Color online) Field-sweep ^{31}P-NMR spectra measured at 49.15 MHz below $T_N \approx 30$ K

The ^{31}P spectrum measured at 77.5 MHz is broadened abruptly below T_N, indicating that the P site is experiencing the static internal field in the ordered state. In order to precisely probe the line shape associated with the magnetic ordering, we remeasured the spectra below 45 K at a lower frequency of 49.15 MHz. No noticeable line broadening was observed around 43 K, the temperature at which a jump was observed in the $\chi - T$ data [120]. Since NMR is capable of probing the intrinsic spin properties, the absence of an anomaly at 43 K suggests that its origin is extrinsic. As suggested by Nath *et al.*[120], the jump in the $\chi - T$ data at 43 K might be due to the presence of the ferrimagnetic impurity Mn_3O_4[225][226]. As demonstrated in Fig. 6.5, with decreasing T a systematic line broadening on either side of the narrow central line occurs below 30 K. This line broadening increases and the intensity of

the central line decreases with decreasing temperature. At low temperatures the broad line takes an almost rectangular shape down to 10 K, whereas below 10 K the edges of the line are smeared following the 10 K magnetic transition which is evidenced in the $\chi(T)$ measurements [120] as a change in slope. The possible origin of these changes in the line shape is discussed later. Even far below 10 K, the central line related to the high-T paramagnetic phase does not disappear from the experimental spectra completely. The coexistence of the high-T phase with the low-T phase has been observed before in $BaCuP_2O_7$ [118], (Li,Na)VGe_2O_6 [227][228][229], and $(Ca_4Al_2O_6)Fe_2(As_{1x}P_x)_2$ [230]. One could argue that the coexistence of the two phases is due to a spread of the transition temperatures within the polycrystalline sample, but in this case it would seem quite unlikely to observe the distinct peak in the temperature dependence of $1/T_1$ as seen in Fig. 6.4. Another possible origin of the narrow central line is the presence of crystal defects or local dislocations in a polycrystalline sample. A very broad background signal was also observed at 4.2 K, extending over a large field range. This signal can be attributed to the ^{209}Bi nuclei.

At $T \leq T_N$, the ^{31}P-NMR line broadens abruptly and has an almost rectangular shape at low temperatures, similar to that reported for (Li,Na)VGe_2O_6, CuV_2O_6, $BaCo_2V_2O_8$, and $BaCuP_2O_7$ in the AFM-ordered state [118][227][228][229][231][232]. The broad and rectangular NMR spectra at $T << T_N$ represent the powder spectra of a commensurate antiferromagnetically ordered phase in which the P site feels the internal field of Mn^{+2} spins [233]. If the ^{31}P site is located symmetrically between the neighboring up and down spins, their hyperfine fields induced at this site will be equal and opposite. In this case, one finds a symmetric powder spectrum or, for a single crystal, two narrow lines of equal intensity will appear on both sides of the zero-shift position, as in $Pb_2VO(PO_4)_2$ and (Ba,Sr)Fe_2As_2[234][235]. In order to determine the magnitude of internal field H_i at the ^{31}P-NMR site, we calculated the line shape of the NMR spectrum in the AFM-ordered state and fitted the calculated spectrum to the experiment. In powder samples, the angle between the direction of the external magnetic field H and that of the internal magnetic field H_i due to the AFM-ordered spins is randomly distributed. Therefore, the NMR spectrum denoted by $f(H)$ has the form [231][233]

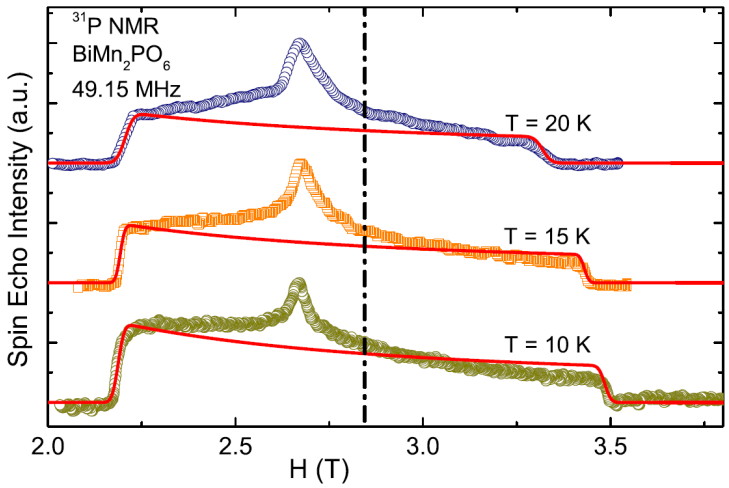

Figure 6.6 (Color online) ^{31}P-NMR spectra in the ordered state at $T < T_{\rm N}$ 30 K measured at 49.15 MHz. The solid lines represent the calculated spectra at different temperatures using eqn (6.3) with a distribution function $g(H)$. The dashed vertical line represents the zero-shift central position $\omega_0/\gamma_{\rm N}$= 2.845 T for ^{31}P nuclei. The parameters used to simulate the spectrum at T = 10 K are $H_{\rm i}$ = 6.546 kOe and $\Delta H_{\rm i} \simeq 0.13$ kOe.

$$f(H) \propto \frac{H^2 - H_i^2 + \omega^2/\gamma_{\rm N}^2}{H_{\rm i} H^2} \tag{6.2}$$

where ω is the NMR angular frequency, which is assumed to be larger than $\gamma_{\rm N} H_{\rm i}$. The spectrum has two cutoff fields, $\omega/\gamma_{\rm N} - H_{\rm i}$ and $\omega/\gamma_{\rm N} + H_{\rm i}$, at which the spectrum has two sharp edges. In powder samples, these sharp edges are normally smoothed because of the inhomogeneous distribution of internal fields. This effect is modeled by the Gaussian distribution function for $H_{\rm i}$. Finally, the spectra were simulated using the convolution of Eq. 6.2 and the distribution function as [231]

$$F(H) = \int_0^\infty f(H - H') g(H') dH' \tag{6.3}$$

where $g(H') = \frac{1}{\sqrt{2\pi\Delta H_{\rm i}^2}} \exp[-\frac{1}{2}\frac{(H-H_{\rm i})^2}{\Delta H_{\rm i}^2}]$ (Gaussian distribution function). Since in the AFM-ordered state the center of gravity of the rectangular spectra coincides with the zero-shift position, $\omega/\gamma_{\rm N}$ = 2.845 T was kept fixed for all temperatures. As shown in Fig. 6.6, the

simulated spectra reproduce the edges of the experimentally obtained broad and rectangular spectra quite well down to 10 K. This indicates that the ordered state is commensurate between 10 K and 30 K.

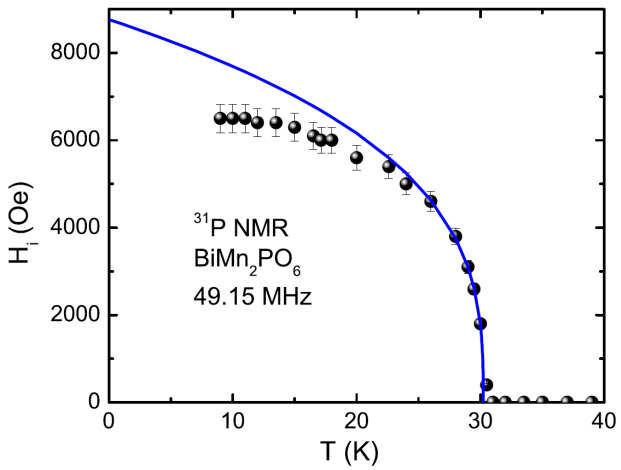

Figure 6.7 (Color online) T dependence of the internal field $H_{\rm i}$ obtained from ^{31}P-NMR spectra measured at 49.15 MHz above 10 K in the ordered state. The solid (blue) line is a fit of the data with 26 K $\leq T \leq$ 30.5 K by Eq. 6.4 using the parameters given in the text.

The T dependence of the internal field $H_{\rm i}$ at the ^{31}P site, which is proportional to the Mn sublattice magnetization in the ordered state, was obtained from fitting our $F(H)$ data by Eq. 6.3 as shown in Fig. 6.7. Below 15 K, $H_{\rm i}(T)$ reaches saturation and remains almost constant. At higher temperatures, $H_{\rm i}(T)$ decreases as T approaches $T_{\rm N}$. In order to extract the critical exponent (β) of the order parameter (sublattice magnetization), $H_{\rm i}$ versus T was fitted by the power law

$$H_{\rm i}(T) = H_0\left(1 - \frac{T}{T_{\rm N}}\right)^{\beta} \tag{6.4}$$

where H_0 is a constant. For an accurate determination of the critical exponent β, we used data points close to $T_{\rm N}$, i.e., in the critical region. As shown in Fig. 6.7, by fitting the data points in the temperature range 26 K $\leq T \leq$ 30.5 K by Eq. 6.4 we obtained $H_0 \simeq 8760$ Oe, $T_{\rm N} = 30\pm1$ K, and $\beta = 0.325\pm0.02$. For comparison, we included the data points below 26 K and arrived at the lower value of $\beta \simeq 0.27$ with $T_{\rm N} \simeq 30.13$ K. The critical exponent β reflects the

universality class or, equivalently, the dimensionality of the spin Hamiltonian. The expected values of β for different universality classes are listed in Ref.[109]. In $BiMn_2PO_6$, the fitted value of β in the critical regime is close to the one expected for the 3D Heisenberg model, thus suggesting the 3D nature of the magnetic ordering transition at 30 K.

In general, $1/T_1T$ is expressed in terms of the generalized susceptibility $\chi_M(\vec{q},\omega_0)$ per mole of electronic spins as [150][236]

$$\frac{1}{T_1T} = \frac{2\gamma_N^2 k_B}{N_A^2}\sum_{\vec{q}}|A(\vec{q})|^2\frac{\chi_M^{''}(\vec{q},\omega_0)}{\omega_0} \tag{6.5}$$

where the sum is over wave vectors $\vec{q}$ within the first Brillouin zone, $A(\vec{q})$ is the form factor of the hyperfine interactions as a function of $\vec{q}$, and $\chi_M^{''}(\vec{q},\omega_0)$ is the imaginary part of the dynamic susceptibility at the nuclear Larmor frequency ω_0. The uniform static molar susceptibility $\chi = \chi_M^{'}(0,0)$ corresponds to the real component $\chi_M^{'}(\vec{q},\omega_0)$ with $q = 0$, ω_0 =0. In the paramagnetic regime, $1/(\chi T_1T)$ should remain T-independent. The $1/(\chi T_1T)$ is plotted along the right y-axis in Fig. 6.4. Instead of a T-independent behavior, an increase in $1/(\chi T_1T)$ was observed upon cooling below 300 K, indicating that $\sum_{\vec{q}}|A(\vec{q})|^2\chi_M^{''}(\vec{q},\omega_0)$ increases more than χ does due to the growth of AFM correlations. This increase persists up to the highest measured temperature.

At sufficiently high temperatures, $1/T_1$ is constant in a system with exchange-coupled local moments and can be expressed within the Gaussian approximation of the correlation function of the electronic spin as [126]

$$\left(\frac{1}{T_1}\right)_{T\to\infty} = \frac{(\gamma_N g\mu_B)^2\sqrt{2\pi}z'S(S+1)}{3\omega_{ex}}\left(\frac{A_{hf}}{z'}\right)^2 \tag{6.6}$$

where $\omega_{ex} = (|J_{max}|k_B/\hbar)\sqrt{2zS(S+1)/3}$ is the Heisenberg exchange frequency, z is the number of nearest-neighbor spins of each Mn^{2+} ion, and z' is the number of nearest-neighbor Mn^{2+} spins for a given P site. The z' coefficient in the numerator is due to the fact that the P site feels fluctuations arising from all nearest-neighbor Mn^{2+} spins. Using the relevant parameters, $A_{hf} \simeq 7224$ Oe/μ_B, $\gamma_N = 1.08\times10^8$ rad $s^{-1}T^{-1}$, $z = 3$, $z' = 6$, $g = 2$, $S = 5/2$, and a high-temperature (250 K) relaxation rate of $(\frac{1}{T_1})_{T\to\infty} \simeq 12800$ s^{-1} for the P site, the magnitude of the maximum exchange coupling constant is calculated to be $J_{max}/k_B \simeq 4.3$ K, which is in reasonable agreement with the values obtained from the density-functional theory (DFT) band-structure calculations [120].

In the AFM-ordered state, $1/T_1$ is mainly driven by scattering of magnons off nuclear spins, leading to a power law T dependence [238][239][240]. For $T >> \Delta/k_B$, where Δ is the energy gap in the spin wave spectrum, $1/T_1$ follows either a T^3 behavior due to a two-magnon Raman process or a T^5 behavior due to a three-magnon process, while for $T << \Delta/k_B$, it follows an activated behavior, $1/T_1 \propto T^2 \exp(-\Delta/k_B T)$ As seen from Fig. 6.4, our ^{31}P-$1/T_1$ data below T_N follow a T^3 behavior rather than a T^5 behavior, suggesting that the relaxation is mainly governed by the two-magnon Raman process. However, a deviation from the power law was observed for $T \leq 10$ K which is either due to the opening of a gap or due to the formation of an incommensurate or canted AFM ordering. The heat capacity data at low T argue against the spin-gap interpretation[120].

6.1.3 Conclusion

The ^{31}P-NMR measurements done on the polycrystalline $BiMn_2PO_6$ compound suggests that it has an AFM long-range ordered ground state below $T_N \simeq 30$ K. A kink in the $\chi - T$ data [120], a sharp peak in the heat capacity[120] and in $1/T_1$ at the same temperature confirms the above. Also, no signature of low dimensionality was observed in the thermodynamic properties [120] of the compound[120]. The shape of the NMR spectra between 10 K and 30 K proved the existence of commensurate magnetic order. Below 10 K, the shape of the NMR spectrum changes either due to an incommensurate magnetic order or due to spin reorientation. A change of slope is observed at 10 K in the $\chi - T$ [120] plot suggesting some magnetic transition occuring at that T. The value of the Curie-Weiss temperature ($\theta_{CW} \simeq 78$ K) [120] and the value of T_N calculated from the Mean-Field Theory (MFT) ($\simeq 68$ K) [120] without any effects of frustration are more than twice the experimentally observed $T_N \simeq 30$ K. This can attributed to three factors: (i) 1D anisotropy of the exchange couplings $J_{inter}/J_{intra} \sim 0.22$, where J_{inter} and J_{intra} are the the total sum of inter- and intra-ladder exchange couplings [120], (ii) finite size of the spin $= 5/2$ (instead of the classical $S \to \infty$) and (iii) the frustration effect. Neutron diffraction study on this compound can refine the conclusions discussed here and can also provide a more precise nature of the transition at 10 K and of the magnetic structure in the ordered ground state.

CHAPTER 7. CONCLUSIONS AND FUTURE WORK

7.1 Conclusions

This thesis is focussed mainly on using the microscopic tool of nuclear magnetic resonance NMR to study different classes of compounds characterized by the fascinating effects of frustration. NMR enables the investigation of solely the local magnetic properties of compounds. This becomes hugely important because practically it is very difficult to completely eliminate impurities from the compound, and bulk property measurement techniques like magnetization and heat capacity experiments are unable to conclusively detect instrinsic contribution alone. Also NMR is a great tool for gaining an insight into microscopic aspects of the materials. As discussed in Chapter 2, frustrated systems are an area of research which has huge possibilities for the revelation of new physics and novel ground states. The magnetic properties are highly affected by the frustration. The frustrated systems are characterized by suppression of $T_{\rm N}$ yielding high frustration parameter ($f \equiv |\theta_{\rm CW}|/T_{\rm N}$ or J_2/J_1), emergence of short-range magnetic correlations at temperatures much higher than the long-range magnetic ordering temperature and the quantum effects at low temperatures resulting in a temperature (T)-independent behavior or a very weak T dependence of $1/T_1$ at very low T or an increase of the AFM ordering temperature with applied field at low enough fields. The ground state of all the frustrated compounds discussed in this thesis have long-range ordered antiferromagnetic (AFM) ground states. But since frustration is dominantly present in most of the cases, a small perturbation can cause a change in the ground state to a quantum disordered state such as a quantum spin liquid state marked with short range fluctuations present to the lowest T. These perturbations include applying high pressure, site-disorder or dilution of the spin lattice with non-magnetic impurities.

The compounds discussed in this thesis ranged from a non-frustrated itinerant compound $CaFe_2As_2$ to a weakly frustrated localized moment material $Zn_2VO(PO_4)_2$ to a strongly frustrated insulating system $BaCdVO(PO_4)_2$. All three of these above-mentioned compounds can be roughly categorized as described by the $J_1 - J_2$ model. Next the thesis moved to the discussion of frustrated systems in higher spin dimensions *viz.* the spinel compound $CoAl_2O_4$, with a diamond lattice structure and a spin ladder compound $BiMn_2PO_6$ with a strong inter-ladder coupling yielding it three-dimensional rather than a one-dimensional chain magnetic structure typical for weakly-coupled spin ladders with low spin values.

In Chapter 3 the localized quasi-2D (two-dimensional) systems $Zn_2VO(PO_4)_2$ and $BaCdVO(PO_4)_2$ are discussed. ^{31}P-NMR study evidenced that $Zn_2VO(PO_4)_2$ is a *quasi*-2D AFM square lattice with weak frustration. Growth of short-range magnetic correlations is evidenced from broad maxima in both $K_{\rm iso} - T$ and $K_{\rm ax} - T$ plots at $\sim$9 K and from the increase of $1/T_1T\chi$ above $T_{\rm N}$. The compound exhibits long-range ordering below the magnetic transition temperature $T_{\rm N} \simeq 3.75$ K. NMR spectra show a commensurate magnetic order in the system. From the dynamic NMR study done it is evident that in the ordered state relaxation is mainly driven by the three-magnon process. A 2D nature of $Zn_2VO(PO_4)_2$ is clear from the field dependence of $1/T_1$.

$BaCdVO(PO_4)_2$ is another frustrated square-lattice (FSL) compound with similar formula discussed in Chapter 3. We have conducted ^{31}P-NMR measurements under high pressures and low temperatures on $BaCdVO(PO_4)_2$. The frustration in this compound is much higher than in $Zn_2VO(PO_4)_2$ due to the comparable in-plane exchange couplings with opposite signs ($J_2/J_1 \simeq 0.88$). The in-plane anisotropy being negligible, this compound can be considered very close to an ideal $J_1 - J_2$ model compound. AFM short-range correlations start emerging above 1 K as seen from the broad peak of $K_{\rm iso}$, increase of $1/T_1T\chi$ above $T_{\rm N}$. The transition to a magnetically long-range-ordered (LRO) state at $\simeq$ 1 K is driven by the very small but finite intra-plane exchange coupling $J_\perp$. The in-plane exchange couplings are $\sim$ 3 K. The suppression of $T_{\rm N}$ originates from the effects of frustration. This compound lies in the vicinity of the very interesting but unidentified phase between Columnar AFM (CAF) phase and FM phase. Thus, we applied pressure on this compound to study its effects on J_1 and J_2. The first

experimentally evidenced $H-P-T$ phase diagram for FSL vanadates has been established through this work. Under ambient pressure, $T_{\rm N}$ increases slightly with H from 0 to ≈ 2 T and then decreases with further increase in the field. The slight increase of $T_{\rm N}$ at low magnetic field is considered to be due to the suppression of quantum fluctuations by the applied magnetic field. Then, once the magnetic field is strong enough to suppress the antiferromagnetic ordering, $T_{\rm N}$ is reduced and is finally suppressed completely. With further increase in the field, the system is in a fully polarized spin state where all the spins orient themselves along the applied magnetic field. The ground state does not change from the CAF state with application of pressure up to 2.05 GPa, but the saturation field decreases strongly. The extrapolation of the saturation field ($H_{\rm S}$) shows that $H_{\rm S}$ should completely vanish at $p \approx 2.35$ GPa. Pressure does not have any significant effect on $T_{\rm N}$. Together from the NMR shift and the nuclear spin-lattice relaxation measurements lead us to the conclusion that J_1 and J_2 are almost p-independent and the frustration ratio decreases to 0.62 under a pressure of 1.45 GPa. Study of this material under $p > 2.35$ GPa might yield an answer to whether the system goes to the FM state via a first-order phase transtion or reaches a phase with a very novel ground state. Our experimental limitations allowed us to do measurements only up to 2.05 GPa in low temperatures. But it is clear that the results obtained have paved way for the experimental realization of the ground state of the very mysterious phase boundary in the J_1-J_2 model.

In Chapter 4 we focussed on the parent compound of the family of "122" iron arsenide $CaFe_2As_2$ in which FeAs layer has a J_1-J_2 model. Different magnetic properties at low temperatures originating from different heat treatments in the preparation of the sample were studied by ^{75}As NMR and NQR. From the NMR and NQR spectra, the Knight shift and the $1/T_1$ data, we could conclude that while at high temperatures both the "as-grown" and the "annealed" crystals of $CaFe_2As_2$ are in the tetragonal ($\mathcal{T}$) paramagnetic phase, at low temperatures their magnetic properties differ drastically. Below $T_{\rm N} \sim 167$ K, the "annealed" sample showed magnetically long-range ordered orthorhombic ($\mathcal{O}$) phase, whereas the "as-grown" sample showed a structural transition at $T_{\rm s} \sim 96$ K to a non-magnetic collapsed(c)$-\mathcal{T}$ phase. Stripe-type AFM correlations in the HT $\mathcal{T}$ phase were confirmed from the T dependence of $1/T_1T\chi$ and of the ratio $r \equiv T_{1,\rm c}/T_{1,\rm ab}$, while no magnetic correlations were seen in the LT

c$-\mathcal{T}$ phase. The lack of any magnetic broadening of the NMR spectrum and T-independent Knight shift demonstrate no development of static Fe spin correlations in the c$-\mathcal{T}$ phase. These observations, combined with the recent INS measurements showing the absence of magnetic fluctuations, bring us to the conclusion that electron correlations completely disappear in a wide energy scale from NMR to INS techniques in the nonsuperconducting c$-\mathcal{T}$ phase in $CaFe_2As_2$.

Chapter 5 demonstrates the magnetic properties of the spinel compound $CoAl_2O_4$ in which the frustration is caused by the next-nearest-neighbor AFM interaction J_2 which couples nearest neighbor sites of each fcc sublattice of the diamond structure, while the nearest-neighbor interaction J_1 between the two fcc sublattices alone does not induce any frustration for AFM ordering. It is seen that the degree of site disorder x between A and B sites in a spinel $(A_{1-x}B_x)[B_{2-x}A_x]O_4$ plays an important role in determination of the frustration parameter of the compound. The suggested ground states for $CoAl_2O_4$ were spin glass, spin liquid and AFM state. Thus to precisely determine the ground state of the system, ^{27}Al NMR and ^{59}Co-NMR and NQR were done on a very high quality (low $x \sim 0.06$) sample of $CoAl_2O_4$. The NMR data clearly demonstrates that $CoAl_2O_4$ exhibits an AFM ground state below $T_N = 9.8(2)$ K. The symmetric broadening of the ^{27}Al-NMR spectrum below 10 K indicated the presence of a long-range AFM ordered ground state for this compound. Furthermore, the line width of the NMR spectrum which is proportional to the order parameter shows a continuous increase below 10 K. The presence of spontaneous magnetization below 10 K is confirmed directly by the observation of a ^{59}Co NMR signal under zero magnetic field in the magnetically ordered state. The sharp peak of $1/T_1$ at around 10 K further confirms a phase transition to a long-range magnetically ordered state at the same temperature. This is consistent with the presence of a sharp peak in the heat capacity at $\simeq 9.7$ K and with the neutron diffraction study showing the emergence of (002) magnetic reflection intensity and its dependence on the scattering angle 2θ. The results from the neutron diffraction measurements are not only consistent with the NMR results but also indicate a collinear long-range AFM-ordered ground state for this compound with an ordered moment of 1.9(5) μ_B/Co. The emergence of AFM correlations was manifested by the increase of $1/T_1T\chi$ below 100 K. The presence of short-range correlations was also indicated by the magnetic entropy S_{Mag} at T_N which was considerably smaller than

its value at high temperature. Also, broad magnetic peaks observed below 50 K in the neutron diffraction measurements, and the broad peak in χ (T) at $\approx$ 15 K confirms the existence of short-range AFM correlations. There are two interesting factors which govern the magnetic properties of this system, *viz*. frustration and site-inversion. We had used a successfully prepared polycrystalline sample of $CoAl_2O_4$ with a low inversion parameter $x = 0.057(20)$ for our NMR study. The value of x is a key parameter that determines the magnetic properties of $CoAl_2O_4$. Site disorder creates spin vacancies and increased randomness of exchange interactions in the already frustrated compound. The suppresion of the value of magnetic entropy at high temperatures from the value expected for $S = 3/2$ suggests that the effective spin of the Co at the A-site is smaller than 3/2, which could be a manifestation of both spin frustration and Co-Al site inversion effects. The average ordered magnetic moment is calculated from the NMR measurements to be around 2.4 μ_B which is smaller than the value of 3 μ_B expected for $g = 2$ and $S = 3/2$ system, mainly due to spin frustration effects. The site inversion between the A- and the B-sites creates spin vacancies in the system. The presence of short-range correlations below 100 K can be argued to be caused by frustration which suppresses the T_N to 10 K. In addition short-range correlations can arise due to disorder, associated with the site inversion. As pointed out previously, although a spin-liquid ground state has been proposed from magnetic susceptibility measurements for $CoAl_2O_4$ with low values of x, our NMR data conclusively proved the existence of a long-range AFM-ordered state below 10 K. Since site inversion plays a crucial role in determining the magnetic properties of this spinel compound, it will also be interesting to perform systematic NMR and neutron diffraction measurements in a highly disordered (high x) $CoAl_2O_4$ to investigate how the system changes from the AFM state to a spin glass state. Application of pressure does not have any significant change in the magnetic transition temperature or on the ground state of the compound. The only effect is the suppression of the $1/T_1$ below T_N under pressure.

In Chapter 6 spin ladder compound $BiMn_2PO_6$ was discussed. It showed very interesting properties due to the dominance of several exchange couplings simultaneously. Generally spin ladders with low spin values are seen to have a 1D nature and with increase in spin value we expect the compound to behave more classically. But in practice $S \neq \infty$ but finite (5/2). Thus

the system still has quantum effects in its ground state properties. The ^{31}P-NMR measurements done on the polycrystalline $BiMn_2PO_6$ compound suggest that it has an AFM long-range ordered ground state below $T_N \simeq 30$ K. A kink in the $\chi - T$ data, a sharp peak in the heat capacity and in $1/T_1$ at the same temperature confirms the above. Also, no signature of low dimensionality was observed in the thermodynamic properties of the compound. The shape of the NMR spectra between 10 K and 30 K proved the existence of commensurate magnetic order. Below 10 K, the shape of the NMR spectrum changes either due to an incommensurate magnetic order or due to spin reorientation. A change of slope is observed at 10 K in the $\chi - T$ plot suggesting some magnetic transition occuring at that T. The value of the Curie-Weiss temperature ($\theta_{CW} \simeq 78$ K) and the value of T_N calculated from the Molecular-Field Theory (MFT) ($\simeq 68$ K) without any effects of frustration are more than twice the experimentally observed $T_N \simeq 30$ K. This can attributed to three factors: (i) 1D anisotropy of the exchange couplings $J_{inter}/J_{intra} \sim 0.22$, where J_{inter} and J_{intra} are the the total sum of inter- and intra-ladder exchange couplings, (ii) finite size of the spin = 5/2 (instead of the classical $S \to \infty$) and (iii) the frustration effect. Neutron diffraction studies on this compound can refine the conclusions discussed here and can also provide a more precise nature of the transition at 10 K and of the magnetic structure in the ordered state.

7.2 Future Prospects

The work done in this thesis paves way for exploration of interesting physics in new ground states.

As mentioned in Chapter 3 application of a pressure ≥ 2.35 GPa on $BaCdVO(PO_4)_2$ will result in the complete suppression of the columnar antiferromagnetic ground state and thus might lead to a new ground state. The vicinity of this compound to the probable disordered ground state makes this study very important. Thus, microscopic examination such as NMR or neutron diffraction study on this material under high pressure might yield very exciting results.

Long-range ordering can be suppressed by frustration and also by the dilution of the spin-lattice with non-magnetic impurity. Theoretically it is predicted that for systems diluted with a critical value of $p_c \gtrsim 0.407$ [241][242], where p is the fraction of removed sites or the doping

level, LRO vanishes completely. Also it is suggested, from quantum Monte Carlo simulations [241], that diluted systems behave clasically even for a spin as low as 1/2. Experimental results portray that non-magnetic Ti^{4+}-doping in Li_2VOSiO_4 shows very weak effects on the transition temperature and on the sublattice magnetization[243]. If we define $s \equiv$ slope of the T_N vs x plot then for $Li_2V_{1-x}Ti_xOSiO_4$, $s \simeq 2$ which is lower than the value expected from theory which is $s \simeq 3.2$ [244]. Now as discussed by Papinutto *et al.*[245] frustration prevalent in Li_2VOSiO_4 can play a role in diminishing the effect expected from theoretical study. The material discussed in Chapter 3, $Zn_2VO(PO_4)_2$, was also diluted with non-magnetic Ti^{4+} and the effects were studied by Yogi *et al.*[102]. Fig. 7.1 shows the doping effect on the heat capacity and T_N. The slope $s \simeq 1.5$ is further lowered. The thing to be noted here is frustration has a very weak effect in $Zn_2VO(PO_4)_2$. Yogi *et al.*[102] suggest that the origin of this may be due to anisotropy. Thus, detailed study of the anisotropy in this compound can lead to a clear picture of how dilution is affecting the magnetic properties of this compound.

Chapter 5 proposes very strongly that the degree of site inversion (x) affects the frustration ratio and also the ground state of the A-site spinel compound $CoAl_2O_4$. First it was naively thought that pressure might change the ratio of the exchange couplings J_2/J_1 which might in turn lead to the change of ground state. But we did not find any change in the ground state from our high-pressure study. In our experiment we tried to make a sample as ordered as possible (*i.e.* very low $x \simeq 0.06$). We can now try to explore the other end, which means prepare a sample of $CoAl_2O_4$ with a high degree of site-disorder (high x) and investigate its ground state properties which might lead us to a new disordered phase.

The spin ladder compound $BiMn_2PO_6$ with a high spin and with competing exchange couplings forms a good candidate for study. Indeed we saw that it showed two intrinsic phase transitions. While the transition at $\simeq 30$ K was the one to a long-range ordered state, the transition at $\simeq 10$ K is probably due to a spin reorientation or the transition from a commensurate to a incommensurate magnetic ordering. Thus, to understand the nature of transition at 10 K, a neutron diffraction study on $BiMn_2PO_6$ will be a good idea.

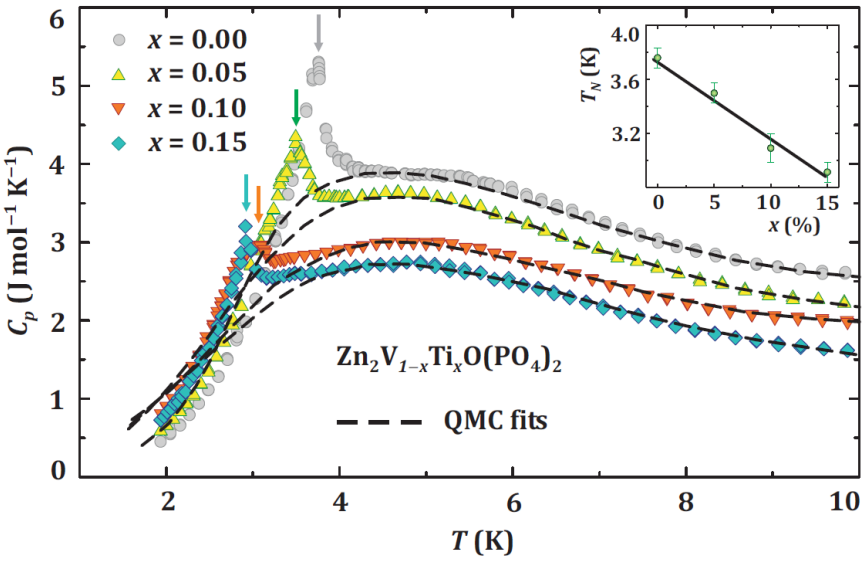

Figure 7.1 (Color online) T dependence of heat capacity of $Zn_2V_{1-x}Ti_xO(PO_4)_2$ is shown. The inset shows how the T_N decreases with x[102].

Bibliography

[1] C. Slichter, *Principles of Magnetic Resonance*, (Springer-Verlag, Berlin, 1990).

[2] X. Zong, Ph.D. thesis, Iowa State University (2008).

[3] L. D. Landau and E. M. Lifshitz, *Quantum Mechanics* (Butterworth Heinemann, New York, 2003).

[4] L. Schiff, *Quantum Mechanics* (McGraw-Hill, New York, 1955).

[5] A. Abragam, *Principles of Nuclear Magnetism* (Clarendon Press, Oxford, 1961).

[6] E. Fukushima and S. B. W. Roeder, *Experimental Pulse NMR: A Nuts and Bolts Approach*, (Addison Wesley Longman Publishing Co., December 1981).

[7] W. D. Knight, Phys. Rev. **76**, 1259 (1949).

[8] C. H. Townes, C. Herring, and W. D. Knight, Phys. Rev. **77**, 852 (1950).

[9] L. L. Lumata, Ph.D. thesis, The Florida State University (2008).

[10] G. C. Carter, L. H. Bennett and D. J. Kahan, *Metallic Shifts in NMR* (Pergamon Press, England, 1977).

[11] R. Kubo and Y. Obata, J. Phys. Soc. Jpn. **11**, 547 (1956).

[12] T. P. Das and E. H. Sondheimer, Phil. Mag. **5**, 529 (1960).

[13] J. Korringa, Physica **16**, 601 (1950).

[14] T. Caldwell, Ph.D. thesis, The Florida State University (2004).

[15] R. Kubo, Rep. Prog. Phys. **29**, 255 (1966).

[16] E. L. Hahn, Phys. Rev. **80**, 580 (1950).

[17] H. Y. Carr and E. M. Purcell, Phys. Rev. **94**, 630 (1954).

[18] R. S. Smith, Ph.D. thesis, The Florida State University (2010).

[19] N. D. Mathur, F. M. Grosche, S. R. Julian, I. R. Walker, D. M. Freye, R. K. W. Haselwimmer, and G. G. Lonzarich, Nature **394**, 39 (1998); E. Pavarini, S. C. Tarantino, T. Boffa Ballaran, M. Zema, P. Ghigna, and P. Carretta, Phys. Rev. B **77**, 014425 (2008); S. K. Kim, M. S. Torikachvili, E. Colombier, A. Thaler, S. L. Bud'ko, and P. C. Canfield, Phys. Rev. B **84**, 134525 (2011).

[20] I. R. Walker, Cryogenics **45**, 87 (2005).

[21] Keiichi Yokogawa, Keizo Murata, Harukazu Yoshino and Shoji Aoyama, Jpn. J. Appl. Phys. **46**, 3636 (2007).

[22] Tamas Vargaa, Angus P. Wilkinson and Ross J. Angel, Rev. Sci. Instrum. **74**, 4564, (2003).

[23] W. J. Duncan, O. P. Welzel, C. Harrison, X. F. Wang, X. H. Chen, F. M. Grosche and P. G. Niklowitz, J. Phys.: Condens. Matter **22**, 052201 (2010).

[24] Naofumi Aso, Tetsuya Fujiwara, Yoshiya Uwatoko, Hiroyuki Miyano, and Hideki Yoshizawa, J. Phys. Soc. Jpn. **76**, 228 (2007).

[25] A. P. Reyes, E. T. Ahrens, R. H. Heffner, P. C. Hammel and J. D. Thompson, Rev. Sci. Instrum. **63**, 3120 (1992).

[26] D. A. Tennant, T. G. Perring, R. A. Cowley and S. E. Nagler, Phys. Rev. Lett. **70**, 4003 (1993); S. Majumdar, V. Hardy, M. R. Lees, D. McK. Paul, H. Rousselière, and D. Grebille, Phys. Rev. B **69**, 024405 (2004).

[27] E. Dagotto, Rep. Prog. Phys. **62**, 1525 (1999); Z. Hiroi and M. Takano, Nature **377**, 41 (1995); Z. Hiroi, J. Solid State Chem. **123** 223 (1996); B. C. Watson, V. N. Kotov, M. W. Meisel, D. W. Hall, G. E. Granroth, W. T. Montfrooij, S. E. Nagler, D. A Jensen,

R. Backov, M. A. Petruska, G. E. Fanucci, and D. R. Talham, Phys. Rev. Lett. **86**, 5168 (2001) .

[28] H. Kageyama, K. Yoshimura, R. Stern, N. V. Mushnikov, K. Onizuka, M. Kato, K. Kosuge, C. P. Slichter, T. Goto, and Y. Ueda, Phys. Rev. Lett. **82**, 3168 (1999); H. Kageyama, M. Nishi, N. Aso, K. Onizuka, T. Yosihama, K. Nukui, K. Kodama, K. Kakurai, and Y. Ueda, Phys. Rev. Lett., **84**, 5876 (2000) ; T. Muto, K. Kobayashi, T. Goto, A. Oosawa, S. Yoshii, T. Sasaki, N. Kobayashi, S. Michimura, F. Iga, and T. Takabatake, J. Phys.: Conf. Ser. **400**, 032059 (2012); D. Vaknin, S. K. Sinha, D. E. Moncton, D. C. Johnston, J. M. Newsam, C. R. Safinya, and H. E. King, Jr., Phys. Rev. Lett. **58**, 2802 (1987); K. B. Lyons, P. A. Fleury, J. P. Remeika, and T. J. Nergan, Phys. Rev. B **37**, 2353 (1988).

[29] N. W. Ashcroft and N. D. Mermin, *Solid State Physics* (Thomson and Brookes/Cole, Singapore, 1976).

[30] R. Moessner, A. P. Ramirez, Physics Today **59**(2), 24 (2006).

[31] G. Toulouse, Commun. Phys. **2**, 115 (1977).

[32] H. T. Diep, *Frustrated Spin Systems* (World Scientific, Singapore, 2004).

[33] G. H. Wannier, Phys. Rev. **79**, 357 (1950); Phys. Rev. B **7**, 5017 (1973) .

[34] I. S. Hagemann, Q. Huang, X. P. A. Gao, A. P. Ramirez, and R. J. Cava, Phys. Rev. Lett. **86**, 894 (2001); J. S. Helton, K. Matan, M. P. Shores, E. A. Nytko, B. M. Bartlett, Y. Yoshida, Y. Takano, A. Suslov, Y. Qiu, J.-H. Chung, D. G. Nocera, and Y. S. Lee, Phys. Rev. Lett. **98**, 107204 (2007).

[35] John E. Greedan, J. Mater. Chem. **11**, 37 (2001); H.-M. Guo and M. Franz, Phys. Rev. Lett. **103**, 206805 (2009).

[36] J Villain, J. Phys. C: Solid State Phys. **10**, 1717 (1977).

[37] S. M. Disseler, J. N. Svensson, S. C. Peter, C. P. Byers, C. Baines, A. Amato, S. R. Giblin, P. Carretta, and M. J. Graf, Phys. Rev. B **84**, 174429 (2011).

[38] A. A. Aczel, D. E. Bugaris, L. Li, J.-Q. Yan, C. de la Cruz, H.-C. zur Loye, and S. E. Nagler, Phys. Rev. B **87**, 014435 (2013).

[39] T. Hikihara and O. A. Starykh, Phys. Rev. B **81**, 064432 (2010).

[40] P. W. Anderson, Mat. Res. Bull. **8**, 153 (1973) ; P. Fazekas and P. W. Anderson, Phil. Mag. **30**, 432 (1974); T. M. Rice, Prog. Theor. Phys. Suppl. **160**, 39 (2005).

[41] L. Balents, Nature **464**, 199 (2010); J. Knolle, D. L. Kovrizhin, J. T. Chalker, and R. Moessner, Phys. Rev. Lett. **112**, 207203 (2014).

[42] W. Wu, B. Ellman, T. F. Rosenbaum, G. Aeppli, and D. H. Reich, Phys. Rev. Lett. **67**, 2076 (1991); W. Wu, D. Bitko, T. F. Rosenbaum, and G. Aeppli, Phys. Rev. Lett. **71**, 1919 (1993).

[43] P. W. Anderson, Science **235**, 1196 (1987).

[44] D. C. Johnston, R. J. McQueeney, B. Lake, A. Honecker, M. E. Zhitomirsky, R. Nath, Y. Furukawa, V. P. Antropov, and Yogesh Singh, Phys. Rev. B **84**, 094445 (2011).

[45] K. Hirakawa, H. Kadowaki, and K. Ubukoshi, J. Phys. Soc. Jpn. **54**, 3526 (1985).

[46] S. Hov, H. Bratsberg, and A. T. Skjeltorp, J. Magn. Magn. Mater. **15**, 455 (1980).

[47] A. P. Ramirez, Annu. Rev. Mater. Sci. **24**, 453 (1994).

[48] L. Siurakshina, D. Ihle, and R. Hayn, Phys. Rev. B **61**, 14601 (2000).

[49] N. D. Mermin and H. Wagner, Phys. Rev. Lett. **17**, 1133 (1966).

[50] C. de la Cruz, Q. Huang, J. W. Lynn, J. Li, W. Ratcliff II, J. L. Zarestky, H. A. Mook, G. F. Chen, J. L. Luo, N. L. Wang, and P. Dai, Nature **453**, 899 (2008); S. T. Bramwell, M. J. Harris, B. C. den Hertog, M. J. P. Gingras, J. S. Gardner, D. F. McMorrow, A. R. Wildes, A. L. Cornelius, J. D. M. Champion, R. G. Melko, and T. Fennell, Phys. Rev. Lett. **87**, 47205 (2001).

[51] Y. Yamashita and K. Ueda, Phys. Rev. Lett. **85**, 4960 (2000).

[52] M. Y. Veillette, J. T. Chalker, and R. Coldea, Phys. Rev. B **71**, 214426 (2005).

[53] J. Villain, R. Bidaux, J. P. Carton, and R. Conte, J. Physique **41**, 1263 (1980); E. Rastelli and A. Tassi, J. Phys. C **20**, L303 (1987); C. L. Henley, Phys. Rev. Lett. **62**, 2056 (1989); A. Chubukov, Phys. Rev. Lett. **69**, 832 (1992); C. L. Henley, J. Appl. Phys. **61**, 3962 (1987).

[54] F. Becca, *Quantum Spin Liquids* (CNR and SISSA 2014).

[55] N. Shannon, B. Schmidt, K. Penc, and P. Thalmeier, Eur. Phys. J. B **38**, 599 (2004) ; B. Schmidt, N. Shannon, and P. Thalmeier, J. Phys.: Condens. Matter **19**, 145211 (2007).

[56] N. Shannon, T. Momoi, and P. Sindzingre, Phys. Rev. Lett. **96**, 027213 (2006).

[57] O. P. Sushkov, J. Oitmaa, and Zheng Weihong, Phys. Rev. B **63**, 104420 (2001).

[58] J. Richter, R. Darradi, J. Schulenburg, D. J. J. Farnell, and H. Rosner, Phys. Rev. B **81**, 174429 (2010).

[59] R. Melzi, S. Aldrovandi, F. Tedoldi, P. Carretta, P. Millet, and F. Mila, Phys. Rev. B **64**, 024409 (2001); R. Melzi, P. Carretta, A. Lascialfari, M. Mambrini, M. Troyer, P. Millet, and F. Mila, Phys. Rev. Lett. **85**, 1318 (2000).

[60] N. S. Kini, E. E. Kaul, and C. Geibel, J. Phys.: Condens. Matter **18**, 1303 (2006).

[61] L. Bossoni, P. Carretta, R. Nath, M. Moscardini, M. Baenitz, and C. Geibel, Phys. Rev. B **83**, 014412 (2011).

[62] B. Roy, Y. Furukawa, R. Nath, and D. C. Johnston, J. Phys.: Conf. Ser. **320**, 012048 (2011).

[63] R. Nath, Y. Furukawa, F. Borsa, E. E. Kaul, M. Baenitz, C. Geibel, and D. C. Johnston, Phys. Rev. B **80**, 214430 (2009).

[64] R. S. Dhaka, R. Jiang, S. Ran, S. L. Bud'ko, P. C. Canfield, B. N. Harmon, A. Kaminski, M. Tomić, R. Valentí, and Y. Lee, Phys. Rev. B **89**, 020511(R) (2014).

[65] S.-H. Baek, N. J. Curro, T. Klimczuk, E. D. Bauer, F. Ronning, and J. D. Thompson, Phys. Rev. B **79**, 052504 (2009).

[66] K. Kitagawa, N. Katayama, K. Ohgushi, and M. Takigawa, J. Phys. Soc. Jpn. **78**, 063706 (2009).

[67] T. Shimojima, K. Ishizaka, Y. Ishida, N. Katayama, K. Ohgushi, T. Kiss, M. Okawa, T. Togashi, X. Y. Wang, C. T. Chen, S. Watanabe, R. Kadota, T. Oguchi, A. Chainani, and S. Shin, Phys. Rev Lett. **104**, 057002 (2010).

[68] A. Pandey, D. G. Quirinale, W. Jayasekara, A. Sapkota, M. G. Kim, R. S. Dhaka, Y. Lee, T. W. Heitmann, P. W. Stephens, V. Ogloblichev, A. Kreyssig, R. J. McQueeney, A. I. Goldman, Adam Kaminski, B. N. Harmon, Y. Furukawa, and D. C. Johnston, Phys. Rev. B **88**, 014526 (2013).

[69] S. Kitagawa, Y. Nakai, T. Iye, K. Ishida, Y. Kamihara, M. Hirano, and H. Hosono, Phys. Rev. B **81**, 212502 (2010).

[70] B. Canals and C. Lacroix, Phys. Rev. Lett. **80**, 2933 (1998).

[71] Jason S. Gardner, Michel J. P. Gingras, and John E. Greedan, Rev. Mod. Phys. **82**, 53 (2010).

[72] Sergii Khmelevskyi, Phys. Rev. B **86**, 104429 (2012).

[73] Ch. Kant, J. Deisenhofer, V. Tsurkan, and A. Loidl, J. Phys.: Conf. Ser. **200** 032032, (2010); Y. Shimizu, H. Takeda, M. Tanaka, M. Itoh, S. Niitaka, and H. Takagi, Nature Commun. **3**, 981 (2012).

[74] L. Balents, Nature (London) **464**, 487 (2010).

[75] K. Binder and A. P. Young, Rev. Mod. Phys. **58**, 801 (1986).

[76] S. Sachdev, Physics World **7**(10), 25 (October 1994)

[77] A. P. Ramirez, A. Hayashi, R. J. Cava, R. Siddharthan and B. S. Shastry, Nature (London) **399**, 333 (1999).

[78] P. W. Anderson, Phys. Rev. **102**, 1008 (1956).

[79] S.-H. Lee, C. Broholm, T. H. Kim, W. Ratcliff, II, and S-W. Cheong, Phys. Rev. Lett. **84**, 3718 (2000).

[80] S. Ji, S.-H. Lee, C. Broholm, T. Y. Koo, W. Ratcliff, S.-W. Cheong, and P. Zschack, Phys. Rev. Lett. **103**, 037201 (2009).

[81] G. F. Goya, H. R. Rechenberg, M. Chen, and W. B. Yelon, J. Appl. Phys. **87**, 8005 (2000).

[82] O. Tchernyshyov, Phys. Rev. Lett. **93**, 157206 (2004).

[83] O. Zaharko, N. B. Christensen, A. Cervellino, V. Tsurkan, A. Maljuk, U. Stuhr, C. Niedermayer, F. Yokaichiya, D. N. Argyriou, M. Boehm, and A. Loidl, Phys. Rev. B **84**, 094403 (2011).

[84] N. Büttgen, J. Hemberger, V. Fritsch, A. Krimmel, M. Mücksch, H.-A. Krug von Nidda, P. Lunkenheimer, R. Fichtl, V. Tsurkan, and A. Loidl, New J. Phys. **6**, 191 (2004).

[85] V. Fritsch, J. Hemberger, N. Büttgen, E.-W. Scheidt, H.-A. Krug von Nidda, A. Loidl, and V. Tsurkan, Phys. Rev. Lett. **92**, 116401 (2004).

[86] R. Fichtl, V. Tsurkan, P. Lunkenheimer, J. Hemberger, V. Fritsch, H.-A. Krug von Nidda, E.-W. Scheidt, and A. Loidl, Phys. Rev. Lett. **94**, 027601 (2005).

[87] N. Tristan, J. Hemberger, A. Krimmel, H-A. Krug von Nidda, V. Tsurkan, and A. Loidl, Phys. Rev. B **72**, 174404 (2005).

[88] A. Krimmel, H. Mutka, M. M. Koza, V. Tsurkan, and A. Loidl, Phys. Rev. B **79**, 134406 (2009).

[89] A. Krimmel, M. Mücksch, V. Tsurkan, M. M. Koza, H. Mutka, C. Ritter, D. V. Sheptyakov, S. Horn, and A. Loidl, Phys. Rev. B **73**, 014413 (2006).

[90] G. M. Kalvius, A. Krimmel, O. Hartmann, F. J. Litterst, R. Wäppling, V. Tsurkan, and A. Loidl, Physica B **404**, 660 (2009).

[91] A. Krimmel, V. Tsurkan, D. Sheptyakov and A. Loidl, Physica B **378**, 583 (2006).

[92] T. Suzuki, H. Nagai, M. Nohara, and H. Takagi, J. Phys.: Condens. Matter **19**, 145265 (2007).

[93] Toshio Fukai, Yuji Furukawa, Shinji Wada, and Kazuo Miyatani, J. Phys. Soc. Jpn. **65**, 4067 (1996).

[94] D. Bergman, J. Alicea, E. Gull, S. Trebst, and L. Balents, Nature Phys. **3**, 487 (2007).

[95] E. Lieb and D. C. Mattis, J. Math. Phys. **3** 749 (1962).

[96] S. R. White, R. M. Noack, and D. J. Scalapino, Phys. Rev. Lett. **73**, 886 (1994).

[97] Ian Affleck, Phys. Rev. B **37**, 5186 (1988).

[98] M. Azuma, Z. Hiroi, M. Takano, K. Ishida, and Y. Kitaoka, Phys. Rev. Lett. **73**, 3463 (1994).

[99] T. Nagata, M. Uehara, J. Goto, J. Akimitsu, N. Motoyama, H. Eisaki, S. Uchida, H. Takahashi, T. Nakanishi, and N. Môri, Phys. Rev. Lett. **81**, 1090 (1998).

[100] M. Valldor, O. Heyer, A. C. Komarek, A. Senyshyn, M. Braden, and T. Lorenz, Phys. Rev. B **83**, 024418 (2011).

[101] S. R. White, R. M. Noack, and D. J. Scalapino Phys. Rev. Lett. **73**, 886 (1994).

[102] A. Yogi, N. Ahmad, R. Nath, A. A. Tsirlin, J. Sichelschmidt, B. Roy, and Y. Furukawa, arXiv:1409.3076 (submitted to Phys. Rev. B).

[103] K. Lii and H. Tsai, J. Solid State Chem. **90**, 291 (1991).

[104] F. Bayi, G. Pourroy, M. Belaiche, P. Legoll, M. Drillon, and R. Kuentzler, Eur. J. Solid State Inorg. Chem. **30**, 55 (1993).

[105] N. Kini, E. Kaul, and C. Geibel, J. Phys.: Condens. Matter **18**, 1303 (2006).

[106] S. M. Yusuf, A. K. Bera, N. S. Kini, I. Mirebeau, and S. Petit, Phys. Rev. B **82**, 094412 (2010).

[107] S. Kanungo, S. Kar, and T. Saha-Dasgupta, Phys. Rev. B **87**, 054431 (2013).

[108] R. Nath, A. A. Tsirlin, H. Rosner, and C. Geibel, Phys. Rev. B **78**, 064422 (2008).

[109] R. Nath, Y. Furukawa, F. Borsa, E. E. Kaul, M. Baenitz, C. Geibel, and D. C. Johnston, Phys. Rev. B **80**, 214430 (2009).

[110] H. Rosner, R. R. P. Singh, W. H. Zheng, J. Oitmaa, S.-L. Drechsler, and W. E. Pickett, Phys. Rev. Lett. **88**, 186405 (2002); H. Rosner, R. R. P. Singh, W. H. Zheng, J. Oitmaa, and W. E. Pickett, Phys. Rev. B **67**, 014416 (2003).

[111] P. Carretta, N. Papinutto, C. B. Azzoni, M. C. Mozzati, E. Pavarini, S. Gonthier, and P. Millet, Phys. Rev. B **66**, 094420 (2002).

[112] A. A. Tsirlin, A. A. Belik, R. V. Shpanchenko, E. V. Antipov, E. Takayama-Muromachi, and H. Rosner, Phys. Rev. B **77**, 092402 (2008).

[113] H. Rosner, R. R. P. Singh, W. H. Zheng, J. Oitmaa, and W. E. Pickett Phys. Rev. B **67**, 014416 (2003); R. Melzi, S. Aldrovandi, F. Tedoldi, P. Carretta, P. Millet, and F. Mila, Phys. Rev. B **64**, 024409 (2001).

[114] L. Bossoni, P. Carretta, R. Nath, M. Moscardini, M. Baenitz, and C. Geibel, Phys. Rev. B **83**, 014412 (2011).

[115] E. E. Kaul, Ph.D. thesis, Technical University Dresden, 2005.

[116] Alexander A. Tsirlin, Ramesh Nath, Artem M. Abakumov, Roman V. Shpanchenko, Christoph Geibel, and Helge Rosner, Phys. Rev. B **81**, 174424 (2010).

[117] G. S. Rushbrooke and P. J. Wood, Mol. Phys. **1**, 257 (1958).

[118] R. Nath, A. V. Mahajan, N. Büttgen, C. Kegler, A. Loidl, and J. Bobroff, Phys. Rev. B **71**, 174436 (2005).

[119] Y. Furukawa, M. Luban, F. Borsa, D. C. Johnston, A. V. Mahajan, L. L. Miller, D. Mentrup, J. Schnack, and A. Bino, Phys. Rev. B **61**, 8635 (2000).

[120] R. Nath, K. M. Ranjith, B. Roy, D. C. Johnston, Y. Furukawa, and A. A. Tsirlin, Phys. Rev. B **90**, 024431 (2014).

[121] R. Melzi, P. Carretta, A. Lascialfari, M. Mambrini, M. Troyer, P. Millet, and F. Mila, Phys. Rev. Lett. **85**, 1318 (2000).

[122] M. Belesi, F. Borsa, and A. K. Powell, Phys. Rev. B **74**, 184408 (2006).

[123] T. Förster, F. A. Garcia, T. Gruner, E. E. Kaul, B. Schmidt, C. Geibel, and J. Sichelschmidt, Phys. Rev. B **87**, 180401(R) (2013).

[124] P. Carretta, M. Filibian, R. Nath, C. Geibel, and P. J. C. King, Phys. Rev. B **79**, 224432 (2009).

[125] T. Förster, F. A. Garcia, A. N. Ponomaryov, R. Nath, E. E. Kaul, B. Schmidt, S. A. Zvyagin, C. Geibel, and J. Sichelschmidt, J. Phys. Soc. Jpn. Conf. Proc. **3**, 014032 (2014).

[126] T. Moriya, Prog. Theor. Phys. **16**, 23 (1956).

[127] P. Carretta, T. Ciabattoni, A. Cuccoli, E. Mognaschi, A. Rigamonti, V. Tognetti, and P. Verrucchi, Phys. Rev. Lett. **84**, 366 (2000).

[128] D D. Beeman and P. Pincus, Phys. Rev. **166**, 359 (1968).

[129] D. Hone, C. Scherer, and F. Borsa, Phys. Rev. B **9**, 2215 (1974).

[130] Y. Ajiro, Y. Nakajima, Y. Furukawa, and H. Kiriyama, J. Phys. Soc. Jpn. **44**, 420 (1978).

[131] M. Takigawa, N. Motoyama, H. Eisaki, and S. Uchida, Phys. Rev. Lett. **76**, 2173 (1996).

[132] Y. Furukawa, A. Iwai, K. Kumagai, and A. Yakubovsky, J. Phys. Soc. Jpn. **65**, 2393 (1996).

[133] R. Nath, D. Kasinathan, H. Rosner, M. Baenitz, and C. Geibel, *ibidem* **77**, 134451 (2008); R. Nath, A. A. Tsirlin, E. E. Kaul, M. Baenitz, N. Büttgen, C. Geibel, and H. Rosner, *ibidem* **78**, 024418 (2008).

[134] P. Vonlanthen, K. B. Tanaka, A. Goto, W. G. Clark, P. Millet, J. Y. Henry, J. L. Gavilano, H. R. Ott, F. Mila, C. Berthier, M. Horvatic, Y. Tokunaga, P. Kuhns, A. P. Reyes, and W. G. Moulton, Phys. Rev. B **65**, 214413 (2002).

[135] J. L. Gavilano, S. Mushkolaj, H. R. Ott, P. Millet, and F. Mila, Phys. Rev. Lett. **85**, 409 (2000).

[136] B. Pedrini, J. L. Gavilano, D. Rau, H. R. Ott, S. M. Kazakov, J. Karpinski, and S. Wessel, Phys. Rev. B **70**, 024421 (2004).

[137] H. Kinouchi, H. Mukuda, Y. K. P. M. Shirage, H. Fujihisa, Y. Gotoh, H. Eisaki, and A. Iyo, Phys. Rev. B **87**, 121101 (2013).

[138] O. P. Sushkov, J. Oitmaa, and Zheng Weihong, Phys. Rev. B **63**, 104420 (2001).

[139] N. Shannon, T. Momoi, and P. Sindzingre, Phys. Rev. Lett. **96**, 027213 (2006).

[140] J. Richter R. Darradi, J. Schulenburg, D. J. J. Farnell, and H. Rosner, Phys. Rev. B **81**, 174429 (2010).

[141] A. P. Ramirez, Nat. Phys. **4**, 442 (2008).

[142] A. A. Tsirlin and H. Rosner, Phys. Rev. B **79**, 214417 (2009).

[143] A. A. Tsirlin, B. Schmidt, Y. Skourski, R. Nath, C. Geibel, and H. Rosner, Phys. Rev. B **80**, 132407 (2009).

[144] E. Pavarini, S. C. Tarantino, T. Boffa Ballaran, M. Zema, P. Ghigna, and P. Carretta, Phys. Rev. B **77**, 014425 (2008).

[145] A. P. Reyes, E. T. Ahrens, R. H. Heffner, P. C. Hammel, and J. D. Thompson, Rev. Sci. Instrum. **63**, 3120 (1992).

[146] H. Fukazawa, N. Yamatoji, Y. Kohori, C. Treakura, N. Takeshita, Y. Tokura, and H. Takagi, Rev. Sci. Instrum. **78**, 015106 (2007).

[147] A. Pelissetto and E. Vicari, Phys. Rep. **368**, 549 (2002).

[148] L. J. de Jongh, *Magnetic Properties of Layered Transition Metal Compounds*, (Klewer, Dordrecht, 1989).

[149] S. T. Bramwell and P. C. W. Holdsworth, J. Phys.: Condens. Matter **5**, L53 (1993); S. T. Bramwell and P. C. W. Holdsworth, Phys. Rev. B **49**, 8811 (1994).

[150] T. Moriya, J. Phys. Soc. Jpn. **18**, 516, (1963).

[151] M. S. Makivic and H.-Q. Ding, Phys. Rev. B **43**, 3562 (1991).

[152] J.-K. Kim and M. Troyer, Phys. Rev. Lett. **80**, 2705 (1998).

[153] H. Rosner, R. R. P. Singh, W. H. Zheng, J. Oitmaa, and W. E. Pickett, Phys. Rev. B **67**, 014416 (2003).

[154] B. Schmidt, P. Thalmeier, and Nic Shannon, Phys. Rev. B **76**, 125113 (2007).

[155] Y. Furukawa, B. Roy, S. Ran, S. L. Budko, and P. C. Canfield, Phys. Rev. B **89**, 121109(R) (2014)

[156] S. Ran, S. L. Bud'ko, D. K. Pratt, A. Kreyssig, M. G. Kim, M. J. Kramer, D. H. Ryan, W. N. Rowan-Weetaluktuk, Y. Furukawa, B. Roy, A. I. Goldman, and P. C. Canfield, Phys. Rev. B **83**, 144517 (2011).

[157] D. C. Johnston, Adv. Phys. **59**, 803 (2010); P. C. Canfield and S. L. Bud'ko, Annu. Rev. Condens. Matter Phys. **1**, 27 (2010); G. R. Stewart, Rev. Mod. Phys. **83**, 1589 (2011).

[158] Q. Huang, Y. Qiu, W. Bao, M. A. Green, J. W. Lynn, Y. C. Gasparovic, T. Wu, G. Wu, and X. H. Chen, Phys. Rev. Lett. **101**, 257003 (2008) ; S. D. Wilson, Z. Yamani, C.

R. Rotundu, B. Freelon, E. Bourret-Courchesne, and R. J. Birgeneau, Phys. Rev. B **79**, 184519 (2009); K. Matan, R. Morinaga, K. Iida, and T. J. Sato, Phys. Rev. B **79**, 054526 (2009).

[159] J. Zhao, W. Ratcliff II, J. W. Lynn, G. F. Chen, J. L. Luo, N. L. Wang, J. Hu, and P. Dai, Phys. Rev. B **78**, 140504(R) (2008) ; K. Kaneko, A. Hoser, N. Caroca-Canales, A. Jesche, C. Krellner, O. Stockert, and C. Geibel, Phys. Rev. B **78**, 212502 (2008).

[160] Y. Xiao, Y. Su, M. Meven, R. Mittal, C. M. N. Kumar, T. Chatterji, S. Price, J. Persson, N. Kumar, S. K. Dhar, A. Thamizhavel, and Th. Brueckel, Phys. Rev. B **80**, 174424 (2009).

[161] N. Ni, S. Nandi, A. Kreyssig, A. I. Goldman, E. D. Mun, S. L. Bud'ko, and P. C. Canfield, Phys. Rev. B **78**, 014523 (2008).

[162] A. I. Goldman, D. N. Argyriou, B. Ouladdiaf, T. Chatterji, A. Kreyssig, S. Nandi, N. Ni, S. L. Bud'ko, P. C. Canfield, and R. J. McQueeney, Phys. Rev. B **78**, 100506(R) (2008).

[163] P. C. Canfield, S. L. Bud'ko, N. Ni, A. Kreyssig, A. I. Goldman, R. J. McQueeney, M. S. Torikachvilli, D. N. Argyriou, G. Luke, and W. Yu, Physica C **469**, 404 (2009).

[164] N. Kumar, R. Nagalakshmi, R. Kulkarni, P. L. Paulose, A. K. Nigam, S. K. Dhar, and A. Thamizhavel, Phys. Rev. B **79**, 012504 (2009).

[165] N. Kumar, S. Chi, Y. Chen, K. G. Rana, A. K. Nigam, A. Thamizhavel, W. Ratcliff, S. K. Dhar, and J. W. Lynn, Phys. Rev. B **80**, 144524 (2009).

[166] S. Ran, S. L. Bud'ko, W. E. Straszheim, J. Soh, M. G. Kim, A. Kreyssig, A. I. Goldman, and P. C. Canfield, Phys. Rev. B **85**, 224528 (2012).

[167] M. S. Torikachvili, S. L. Bud'ko, N. Ni, and P. C. Canfield, Phys. Rev. Lett. **101**, 057006 (2008).

[168] H. Lee, E. Park, T. Park, V. A. Sidorov, F. Ronning, E. D. Bauer, and J. D. Thompson, Phys. Rev. B **80**, 024519 (2009).

[169] W. Yu, A. A. Aczel, T. J. Williams, S. L. Bud'ko, N. Ni, P. C. Canfield, and G. M. Luke, Phys. Rev. B **79**, 020511 (2009).

[170] A. Kreyssig, M. A. Green, Y. B. Lee, G. D. Samolyuk, P. Zajdel, J. W. Lynn, S. L. Bud'ko, M. S. Torikachvili, N. Ni, S. Nandi, J. B. Leão, S. J. Poulton, D. N. Argyriou, B. N. Harmon, R. J. McQueeney, P. C. Canfield, and A. I. Goldman, Phys. Rev. B **78**, 184517 (2008).

[171] A. I. Goldman, A. Kreyssig, K. Prokes, D. K. Pratt, D. N. Argyriou, J. W. Lynn, S. Nandi, S. A. J. Kimber, Y. Chen, Y. B. Lee, G. Samolyuk, J. B. Leão, S. J. Poulton, S. L. Bud'ko, N. Ni, P. C. Canfield, B. N. Harmon, and R. J. McQueeney, Phys. Rev. B **79**, 024513 (2009).

[172] R. Nath, Y. Singh, and D. C. Johnston, Phys. Rev. B **79**, 174513 (2009).

[173] J. H. Soh, G. S. Tucker, D. K. Pratt, D. L. Abernathy, M. B. Stone, S. Ran, S. L. Bud'ko, P. C. Canfield, A. Kreyssig, R. J. McQueeney, and A. I. Goldman, Phys. Rev. Lett. **111**, 227002 (2013).

[174] R. S. Dhaka, R. Jiang, S. Ran, S. L. Bud'ko, P. C. Canfield, B. N. Harmon, A. Kaminski, M. Tomic, R. Valent, and Y. Lee, Phys. Rev. B **89**, 020511(R) (2014).

[175] S. Kawasaki, T. Tabuchi, X. F. Wang, X. H. Chen, and G.-q. Zheng, Supercond. Sci. Technol. **23**, 054004 (2010).

[176] S. Kawasaki, T. Oka, T. Tabuchi, X. F. Wang, X. H. Chen, and G.-q. Zheng, J. Phys. Chem. Solids **72**, 501 (2011).

[177] L. Ma, G.-F. Ji, J. Dai, S. R. Saha, T. Drye, J. Paglione, and W.-Q. Yu, Chin. Phys. B **22**, 057401 (2013).

[178] J. R. Jeffries, N. P. Butch, K. Kirshenbaum, S. R. Saha, G. Samudrala, S. T. Weir, Y. K. Vohra, and J. Paglione, Phys. Rev. B **85**, 184501 (2012).

[179] S. R. Saha, N. P. Butch, T. Drye, J. Magill, S. Ziemak, K. Kirshenbaum, P. Y. Zavalij, J. W. Lynn, and J. Paglione, Phys. Rev. B **85**, 024525 (2012).

[180] B. Lv, L. Deng, M. Gooch, F. Wei, Y. Sun, J. K. Meen, Y.-Y. Xue, B. Lorenz, and C.-W. Chu, Proc. Natl. Acad. Sci. U.S.A. **108**, 15705 (2011).

[181] M. Danura, K. Kudo, Y. Oshiro, S. Araki, T. C. Kobayashi, and M. Nohara, J. Phys. Soc. Jpn. **80**, 103701 (2011).

[182] K. Kudo, K. Iba, M. Takasuga, Y. Kitahama, J. Matsumura, M. Danura, Y. Nogami, and M. Nohara, Sci. Rep. **3**, 1478 (2013).

[183] P. C. Canfield, *Properties and Applications of Complex Intermetallics*, edited by E. Belin-Ferrè (World Scientific, Singapore, 2010).

[184] P. C. Canfield and Z. Fisk, Philos. Mag. B **65**, 1117 (1992).

[185] S.-H. Beak, N. J. Curro, T. Klimczuk, E. D. Bauer, F. Ronning, and J. D. Thompson, Phys. Rev. B **79**, 052504 (2009).

[186] D. K. Pratt, Y. Zhao, S. A. J. Kimber, A. Hiess, D. N. Argyriou, C. Broholm, A. Kreyssig, S. Nandi, S. L. Bud'ko, N. Ni, P. C. Canfield, R. J. McQueeney, and A. I. Goldman, Phys. Rev. B **79**, 060510(R) (2009).

[187] K. Kitagawa, N. Katayama, K. Ohgushi, and M. Takigawa, J. Phys. Soc. Jpn. **78**, 063706 (2009).

[188] S. Kitagawa, Y. Nakai, T. Iye, K. Ishida, Y. Kamihara, M. Hirano, and H. Hosono, Phys. Rev. B **81**, 212502 (2010).

[189] M. Hirano, Y. Yamada, T. Saito, R. Nagashima, T. Konishi, T. Toriyama, Y. Ohta, H. Fukazawa, Y. Kohori, Y. Furukawa, K. Kihou, C-H. Lee, A. Iyo, and H. Eisaki, J. Phys. Soc. Jpn. **81**, 054704 (2012).

[190] A. Pandey, D. G. Quirinale, W. Jayasekara, A. Sapkota, M. G. Kim, R. S. Dhaka, Y. Lee, T. W. Heitmann, P. W. Stephens, V. Ogloblichev, A. Kreyssig, R. J. McQueeney, A. I. Goldman, Adam Kaminski, B. N. Harmon, Y. Furukawa, and D. C. Johnston, Phys. Rev. B **88**, 014526 (2013).

[191] B. Roy, A. Pandey, Q. Zhang, T. W. Heitmann, D. Vaknin, D. C. Johnston, and Y. Furukawa, Phys. Rev. B **88**, 174415 (2013).

[192] W. L. Roth, J. Phys. (Paris) **25**, 507 (1964).

[193] D. Bergman, J. Alicea, E. Gull, S. Trebst, and L. Balents, Nature Phys. **3**, 487 (2007).

[194] N. Büttgen, J. Hemberger, V. Fritsch, A. Krimmel, M. Mücksch, H.-A. Krug von Nidda, P. Lunkenheimer, R. Fichtl, V. Tsurkan, and A. Loidl New J. Phys. **6**, 191 (2004); N. Büttgen, A. Zymara, C. Kegler, V. Tsurkan, and A. Loidl, Phys. Rev. B **73**, 132409 (2006).

[195] V. Fritsch, J. Hemberger, N. Büttgen, E.-W. Scheidt, H.-A. Krug von Nidda, A. Loidl, and V. Tsurkan, Phys. Rev. Lett. **92**, 116401 (2004).

[196] N. Tristan, J. Hemberger, A. Krimmel, H.-A. Krug von Nidda, V. Tsurkan, and A. Loidl, Phys. Rev. B **72**, 174404 (2005).

[197] A. Krimmel, H. Mutka, M. M. Koza, V. Tsurkan, and A. Loidl, Phys. Rev. B **79**, 134406 (2009).

[198] R. Fichtl, V. Tsurkan, P. Lunkenheimer, J. Hemberger, V. Fritsch, H.-A. Krug von Nidda, E.-W. Scheidt, and A. Loidl, Phys. Rev. Lett. **94**, 027601 (2005).

[199] A. Krimmel, M. Mücksch, V. Tsurkan, M. M. Koza, H. Mutka, C. Ritter, D. V. Sheptyakov, S. Horn, and A. Loidl, Phys. Rev. B **73**, 014413 (2006).

[200] G.M. Kalvius, A. Krimmel, O. Hartmann, F. J. Litterst, R. Wäppling, V. Tsurkan, and A. Loidl, Physica B: Condens. Matter **404**(5), 660 (2009).

[201] A. Krimmel, V. Tsurkan, D. Sheptyakov, and A. Loidl, Physica B **378**, 583 (2006).

[202] T. Fukai, Y. Furukawa, S. Wada, and K. Miyatani, J. Phys. Soc. Jpn. **65**, 4067 (1996).

[203] T. Suzuki, H. Nagai, M. Nohara, and H. Takagi, J. Phys.: Condens. Matter **19**, 145265 (2007).

[204] O. Zaharko, N. B. Christensen, A. Cervellino, V. Tsurkan, A. Maljuk, U. Stuhr, C. Niedermayer, F. Yokaichiya, D. N. Argyriou, M. Boehm, and A. Loidl, Phys. Rev. B **84**, 094403 (2011).

[205] A. P. Ramirez, Annu. Rev. Mater. Sci. **24**, 453 (1994)

[206] O. Zaharko, A. Cervellino, V. Tsurkan, N. B. Christensen, and A. Loidl, Phys. Rev. B **81**, 064416 (2010).

[207] G. J. MacDougall, D. Gout, J. L. Zarestky, G. Ehlers, A. Podlesnyak, M. A. McGuire, D. Mandrus, and S. E. Nagler, Proc. Natl. Acad. Sci. USA **38**, 15693 (2011).

[208] N. Tristan, V. Zestrea, G. Behr, R. Klingeler, B. Büchner, H.-A. Krug von Nidda, A. Loidl, and V. Tsurkan, Phys. Rev. B **77**, 094412 (2008).

[209] K. Hanashima, Y. Kodama, D. Akahoshi, C. Kanadani, and T. Saito, J. Phys. Soc. Jpn. **82**, 024702 (2013).

[210] A. Maljuk, V. Tsurkan, V. Zestrea, O. Zaharko, A. Cerellino, A. Loidl, and D. N. Argyriou, J. Cryst. Growth **311**, 3997 (2009).

[211] K. Miyatani, K. Kohn, S. Iida, and H. Kamimura, J. Phys. Soc. Jpn. **20**, 471 (1965).

[212] T. Tsuda, A. Hirai, and H. Abe, Phys. Lett. **26A**, 463 (1968).

[213] Y. Furukawa, S. Wada, T. Kajitani, and S. Hosoya, J. Phys. Soc. Jpn. **68**, 346 (1999).

[214] A. Abragam, J. Horowitz, and M. H. L. Pryce, Proc. Roy. Soc. (London), Ser. A **230**, 169 (1955).

[215] A. Narath, in *Hyperfine Interactions*, edited by A. J. Freeman and R. B. Frankel (Academic, New York, 1967).

[216] A. J. Freeman and R. E. Watson, in *Magnetism*, edited by G. T. Rado and H. Suhl (Academic, New York, 1965), Vol. 2.

[217] A. Narath, Phys. Rev. **162**, 320 (1967).

[218] A. V. Mahajan, R. Sala, E. Lee, F. Borsa, S. Kondo, and D. C. Johnston, Phys. Rev. B **57**, 8890 (1998).

[219] A. P. Reyes, E. T. Ahrens, R. H. Heffner, P. C. Hammel, and J. D. Thompson, Rev. Sci. Instrum. **63**, 3120 (1992).

[220] H. Fukazawa, N. Yamatoji, Y. Kohori, C. Treakura, N. Takeshita, Y. Tokura, and H. Takagi, Rev. Sci. Instrum. 78, 015106 (2007).

[221] B. Koteswararao, S. Salunke, A. V. Mahajan, I. Dasgupta, and J. Bobroff, Phys. Rev. B **76**, 052402 (2007).

[222] R. Nath, A. V. Mahajan, N. Büttgen, C. Kegler, A. Loidl, and J. Bobroff, Phys. Rev. B **71**, 174436 (2005).

[223] R. Nath, D. Kasinathan, H. Rosner, M. Baenitz, and C. Geibel, Phys. Rev. B **77**, 134451 (2008).

[224] R. Nath, Y. Furukawa, F. Borsa, E. E. Kaul, M. Baenitz, C. Geibel, and D. C. Johnston, Phys. Rev. B **80**, 214430 (2009).

[225] K. Dwight and N. Menyuk, Phys. Rev. **119**, 1470 (1960).

[226] B. Chardon and F. Vigneron, J. Magn. Magn. Mater. **58**, 128 (1986).

[227] J. L. Gavilano, S. Mushkolaj, H. R. Ott, P. Millet, and F. Mila, Phys. Rev. Lett. **85**, 409 (2000).

[228] P. Vonlanthen, K. B. Tanaka, A. Goto, W. G. Clark, P. Millet, J. Y. Henry, J. L. Gavilano, H. R. Ott, F. Mila, C. Berthier, M. Horvatic, Yo Tokunaga, P. Kuhns, A. P. Reyes, and W. G. Moulton, Phys. Rev. B **65**, 214413 (2002).

[229] B. Pedrini, J. L. Gavilano, D. Rau, H. R. Ott, S. M. Kazakov, J. Karpinski, and S. Wessel, Phys. Rev. B **70**, 024421 (2004).

[230] H. Kinouchi, H.Mukuda, Y. Kitaoka, P.M. Shirage, H. Fujihisa, Y. Gotoh, H. Eisaki, and A. Iyo, Phys. Rev. B **87**, 121101 (2013).

[231] J. Kikuchi, K. Ishiguchi, K.Motoya, M. Itoh, K. Inari, N. Eguchi, and J. Akimitsu, J. Phys. Soc. Jpn. **69**, 2660 (2000).

[232] Y. Ideta, Yu Kawasaki, Y. Kishimoto, T. Ohno, Y. Michihiro, Z. He, Y. Ueda, and M. Itoh, Phys. Rev. B **86**, 094433 (2012).

[233] Y. Yamada and A. Sakata, J. Phys. Soc. Jpn. **55**, 1751 (1986).

[234] K. Kitagawa, N. Katayama, K. Ohgushi, M. Yoshida, and M. Takigawa, J. Phys. Soc. Jpn. **77**, 114709 (2008).

[235] K. Kitagawa, N. Katayama, K. Ohgushi, and M. Takigawa, J. Phys. Soc. Jpn. **78**, 063706 (2009).

[236] A. V. Mahajan, R. Sala, E. Lee, F. Borsa, S. Kondo, and D. C. Johnston, Phys. Rev. B **57**, 8890 (1998).

[237] T. Moriya, Prog. Theor. Phys. **16**, 23 (1956); T. Moriya, Prog. Theor. Phys. **16**, 641 (1956).

[238] D. C. Johnston, R. J. McQueeney, B. Lake, A. Honecker, M. E. Zhitomirsky, R. Nath, Y. Furukawa, V. P. Antropov, and Y. Singh, Phys. Rev. B **84**, 094445 (2011).

[239] D. Beeman and P. Pincus, Phys. Rev. **166**, 359 (1968).

[240] M. Belesi, F. Borsa, and A. K. Powell, Phys. Rev. B **74**, 184408 (2006).

[241] A. W. Sandvik, Phys. Rev. B **66**, 024418 (2002).

[242] K. Kato, S. Todo, K. Harada, N. Kawashima, S. Miyashita, and H. Takayama, Phys. Rev. Lett. **84**, 4204 (2000).

[243] A. Bombardi, J. Rodriguez-Carvajal, S. Di Matteo, F. de Bergevin, L. Paolasini, P. Carretta, P. Millet, and R. Caciuffo, Phys. Rev. Lett. **93**, 027202 (2004); R. Melzi, P. Carretta, A. Lascialfari, M. Mambrini, M. Troyer, P. Millet, and F. Mila, Phys. Rev. Lett. **85**, 1318 (2000); R. Melzi, S. Aldrovandi, F. Tedoldi, P. Carretta, P. Millet, and F. Mila,

Phys. Rev. B **64**, 024409 (2001); H. Rosner, R. R. P. Singh, W. H. Zheng, J. Oitmaa, S.-L. Drechsler, and W. E. Pickett, Phys. Rev. Lett. **88**, 186405 (2002); H. Rosner, R. R. P. Singh, W. H. Zheng, J. Oitmaa, and W. E. Pickett, Phys. Rev. B **67**, 014416 (2003).

[244] A. L. Chernyshev, Y. C. Chen, and A. H. Castro Neto, Phys. Rev. B **65**, 104407 (2002).

[245] N. Papinutto, P. Carretta, S. Gonthier, and P. Millet, Phys. Rev. B **71**, 174425 (2005).